Departamento de Nanoestructuras y Superficies
Instituto de Ciencia de Materiales de Madrid
Consejo Superior de Investigaciones Científicas

Low dimensional Fe_3O_4 and $Fe_{1-x}O$: an *ab initio* approach

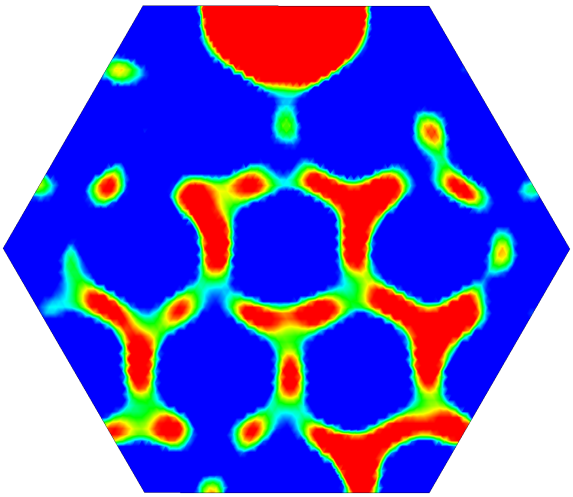

Iván David Bernal Villamil

Departamento de Física Aplicada
Facultad de Ciencias
Universidad Autónoma de Madrid
Madrid, 2015

Departamento de Nanoestructuras y Superficies
Instituto de Ciencia de Materiales de Madrid
Consejo Superior de Investigaciones Científicas

Low dimensional Fe_3O_4 and $Fe_{1-x}O$: an *ab initio* approach

Iván David Bernal Villamil

Director: Dra. Silvia Gallego Queipo
Tutor: Dr. Leonardo Soriano de Arpe

Memoria presentada para acceder al grado de Doctor
Departamento de Física Aplicada
Facultad de Ciencias
Universidad Autónoma de Madrid

Madrid, 2015

Contents

Introduction

This thesis is devoted to the study, by means of *ab initio* methods, of electronic and magnetic properties in binary Fe oxides, with special emphasis on low dimensional forms.

Transition metal monoxides (TMOs), MnO, FeO, CoO and NiO have been object of theoretical and experimental research for decades, since these oxides were thought to be examples of prototypical magnetic Mott insulators[1]. Among them, FeO shows several singularities, the most relevant of which is the defective $Fe_{1-x}O$ stoichiometry at ambient conditions.

In the first part of this introduction we will compile some of the most relevant FeO properties, pointing out the differences and similarities with the rest of monoxides in the series. We will focus on the presence of iron vacancies in FeO, their distribution and organization.

The resulting clusters around which Fe vacancies tend to agglomerate are the basic blocks of the spinel structure of magnetite (Fe_3O_4), one of the most widespread ferrous oxides. The second and last part of this introduction will be devoted to magnetite, a very interesting material both from a technological and fundamental point of view.

Wüstite (FeO)

Several properties are common to all the TMOs, such as a rocksalt lattice, large insulating gaps and AF-II type antiferromagnetism, where adjacent ferromagnetic (111) cation planes couple antiferromagnetically. In Fig. 1(a) we have sketched the FeO lattice structure, where blue and green Fe planes have opposite spin directions.

Below the Néel temperature (T_N), all the TMOs show a distortion from the cubic symmetry, different in every compound, which has been related to the magnetic exchange coupling constants[2]. In the particular case of FeO this distortion is rhombohedral and consists in a weak stretching along the [111] direction, as depicted in Fig. 1(b), with ferromagnetically coupled Fe planes perpedicular to the direction of stretching.

Regarding the presence of defects, all TMOs present different degrees of deviations from stoichiometry, but $Fe_{1-x}O$ is the most non-stoichiometric

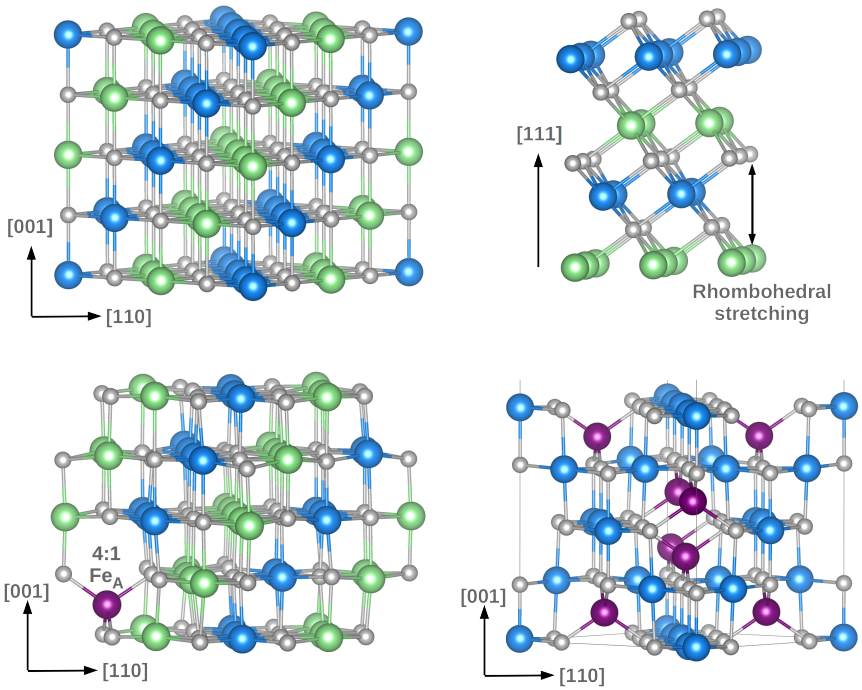

Figure 1: Upper-row: Stoichiometric FeO structures, along the [001] and the [111] direction, where Fe-layers in different colours denote opposite direction of spin. Lower row: 4:1 cluster in wüstite (left) and $Fd\bar{3}m$ magnetite unit cell (right).

among them: it is found in nature with concentrations of Fe deficiency that extend from 5% (at the lowest possible oxygen pressures) to almost 15%[3]. In fact, the stoichiometric FeO form is stable only at the extreme pressures and temperatures of the Earth's lower mantle, one of whose major constituents are solid solutions of the mineral form of FeO, wüstite. This is why FeO is under scrutiny in the field of geophysics and paleomagnetism, where large efforts are devoted to understand its complex transitions at high pressures and to determine the distribution of Fe vacancies (V_{Fe}) in the lattice[4].

Unstable FeO decomposes in Fe_3O_4 and Fe below 570°C and this reaction is slow at room temperature, which allows to prepare $Fe_{1-x}O$ samples with different compositions and local orders by rapid quenching; at the same time, these features depend on the history of the sample. The identification of the different arrangements that may emerge has been an active field of research since the pioneer diffraction study of Roth[5]. Diffraction experiments and atomistic calculations agree[6, 7] that the minimal defect cluster is formed by 4 V_{Fe} surrounding a tetrahedrally coordinated Fe_A^{3+}, the so called 4:1 cluster sketched in Fig. 1(c).

The clusters aggregate in different ways as x is increased, such as face-

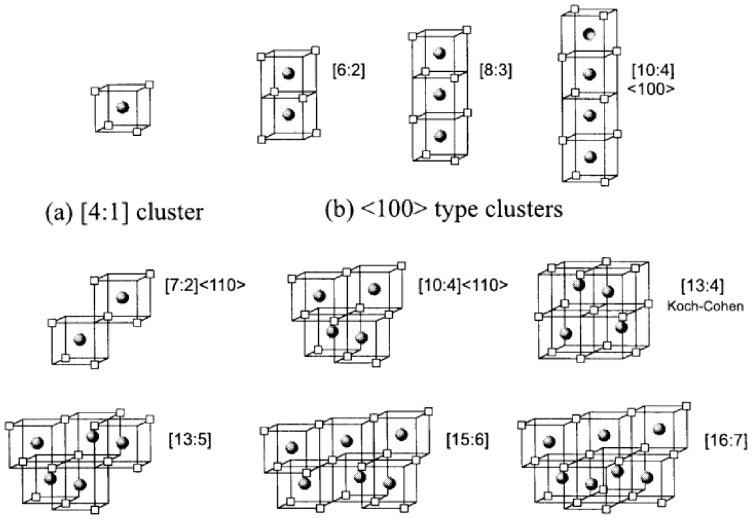

Figure 2: Types of defect clusters proposed for wüstite. In all of them a 4-coordinated ferric iron cation (solid circle) is surrounded by a tetrahedron of octahedral vacancies (empty square vertices). These clusters may be linked sharing corners, as in magnetite, edges or faces[9].

edge- or corner-sharing structures, as shown in Fig. 2, and the ratio between the number of V_{Fe} and Fe_A is believed to increase with temperature and at lower values of x. In fact, different types of aggregates may coexist[8] depending on the history of the sample [4], and it is still not clear if spinel-type local structures (for example, Fe_3O_4) are favored over more compact aggregations[9].

In general, the V_{Fe} influence on the physical properties of the sample is not negligible. On the structural side, the rhombohedral distortion decreases as the V_{Fe} concentration grows [10, 11] and there is an empirical linear relation between x and the unit cell parameter a[12, 13] Also, the specific heat anomaly and the $T_N(\sim 200$ K) depend on x, and the heat capacity is modified across T_N, which evidences changes in the nature of the magnetic transition, with a much stronger cooperative character in FeO than in non-stoichiometric samples. Finally, the conductivity and cation self-diffusion[14] also depend on x, and the carrier type changes from p to n for $x \sim 0.08$.

Studying the fundamental properties of defective FeO at atomic scales seems essential to understand the origin of the observed dependencies on x of the physical properties. Surprisingly, detailed theoretical studies of the influence of V_{Fe} on the electronic structure are scarce and, to the best of our knowledge, only isolated vacancies have been considered with *ab initio* methods. In this thesis, we have performed first-principles calculations of $Fe_{1-x}O$ to determine the stability and electronic properties of 4:1 clusters,

comparing them to structures with isolated V_{Fe} and to stoichiometric FeO.

Furthermore, as the 4:1 cluster is a basic unit for the development of spinel structures at the FeO lattice, our study provides a bridge to explore the evolution from $Fe_{1-x}O$ towards Fe_3O_4, and the influence of the lattice symmetry on the local order, allowing us to extract interesting conclusions about the nature of magnetite short-range correlations.

Magnetite (Fe_3O_4)

Magnetite is the archetype magnetic material and has been used by mankind at least since medieval sailors and even the Olmecs[15]. Due to its unique properties and large abundance, magnetite has been under research in many fields. The presence of magnetite in the Earth's mantle, for example, has motivated intense studies in paleomagnetism and geophysics, and the magnetic orientation of Fe_3O_4 in rock samples has been crucial to investigate plate tectonics. Magnetite has been found to be biocompatible, leading to the implementation of Fe_3O_4 nanoparticles in biomedical applications[16], and ultrasmall superparamagnetic nanoparticles have been used to improve the contrast of magnetic resonance imaging in clinical diagnosis[17].

It is also a very interesting material for magnetic applications, and particularly for the development of emergent technologies, such as spintronics. Examples of this are the preservation of high magnetic moments in organic coatings by surface modifications[18, 19], the manipulation of magnetoresistance in organic spintronic devices[20], and the implementation of magnetite in inorganic structures[21].

Magnetite undergoes a sharp first-order transition at T_V=120 K, observed in measurements of heat capacity, conductivity, magnetization and structural properties. The transition was named after Verwey, who described it for the first time in 1939[22, 23].

Above T_V, Fe_3O_4 crystallizes in the inverse spinel structure $Fd\bar{3}m$, sketched in Fig. 1(d), with general formula AB_2O_4: oxygens form a fcc sublattice and irons are distributed between octahedral (Fe_B) and tetrahedral (Fe_A) sites; the formal charge distribution is represented as $Fe_A^{3+}[Fe_B^{2.5+}]_2O_4$, with twice as many irons in the B-sites as there are in the A-sites. At this temperature range magnetite is a poor metal and its electronic conductivity comes from the minority spin t_{2g} states of the Fe_B crossing the Fermi level.

If we compare to $Fe_{1-x}O$, the large number of V_{Fe} in the Fe_B sublattice leads to a fundamental difference between magnetite and wüstite: the Fe_B sublattice is ferromagnetically coupled, AF-II disappears, as can be seen in Fig. 1. Also, the A and B are sublattices antiferromagnetically coupled, leading to a ferrimagnet with a high magnetic moment of $4\mu_B$ and a Curie temperature of 850 K.

Below T_V, the phase transition manifests in drop of the electrical con-

ductivity of 2-3 orders of magnitude and a structural modification into a monoclinic superstructure with Cc space group symmetry, that corresponds to $(\sqrt{2} \times \sqrt{2} \times 2)$ times the $Fd\bar{3}m$ unit cell. The destruction of half metallicity implies that the formal charge distribution shown before is not longer valid. Two types of Fe_B cations emerge with enhanced (Fe^{3+}) and reduced (Fe^{2+}) valence; the drop of conductivity is determined by the freezing of electron hopping between different Fe_B sites, and the opening of a gap close to 0.2 eV. After decades of research some of the features of the transition remain under discussion. As a matter of fact, the actual low temperature unit cell has been resolved only recently[24, 25, 26, 27], complicated by the presence of microtwinned domains.

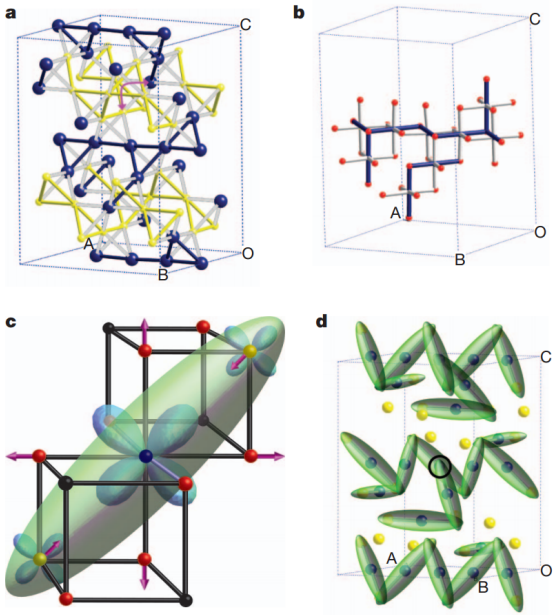

Figure 3: Charge order and trimerons in the low temperature magnetite structure. Figure from [27]. **a.** Distribution of Fe^{2+} and Fe^{3+} states (blue and yellow spheres, respectively) in the first-approximation Verwey-type model, shown in the $(\sqrt{2}a \times \sqrt{2}a \times 2a)$ Cc supercell (a is the high temperature cubic cell parameter.) **b.** Jahn-Teller distortions in a single Fe^{2+} chain. **c.** Sketch of a trimeron, showing the delocalized distribution of a minority-spin electron and the associated atomic displacements within a linear three-Fe-site unit. **d.** Trimeron distribution in the low-temperature magnetite structure, following the experimentally observed distortions.

The distribution of the different Fe_B atoms at the unit cell configures the charge order (CO), intimately linked to the orbital order [9, 10], and determines the full monoclinic Cc symmetry. The detailed origin of the transition, that involves the coupling of electrons, phonons and spins, is still

controversial, though there is agreement that it is driven by electron-phonon interactions in the presence of electronic correlations[28, 29]. Furthermore, there is evidence that some short-ranged charge order survives above T_V, but the role of these correlations on the Verwey transition and their relation to the charge density waves below T_V are not yet understood.

The nature of these correlations has been recently identified in the form of trimerons: linear chains of three adjacent Fe_B cations dominantly formed by a central Fe^{2+} and two Fe^{3+}, with a significant reduction of the interatomic Fe−Fe distances and a polaronic distribution of shared charge[27]. A sketch of the distribution of trimerons in the Cc supercell is presented in Fig. 3(d).

Though magnetite is neither a good metal above T_V nor a large gap insulator at low temperatures, the abrupt drop of the conductivity across the Verwey transition allows for its exploitation in devices. It has been used in spin valves and magnetic tunnel junctions; in different heterostructures the interlayer exchange coupling can be manipulated across the VT [30, 31]. Also, the induction of the metal-insulator transition by external electric fields offers appealing technological possibilities [32, 33, 34]. These applications, together with those in the fields of catalysis or bio-medicine, rely on low dimensional structures, and consequently magnetite samples of reduced dimensions have been synthesized in diverse forms, from nanoparticles to thin films.

Eventhough the number of studies on Fe_3O_4 nanostructures is large, most of them are focused on applications, with less emphasis on the microscopic mechanisms supporting the development of charge density waves and phase transitions. One of the main research lines in this thesis has been exploring the effect that the reduction of dimensionality exerts on the fundamental properties of magnetite. We have mainly concentrated on aspects related to the opening of an insulating gap and the development of charge and magnetic orders, keeping in mind that the VT cannot be restricted to an electronic phase transition[28, 35]. We have focused on thin film geometries, based on previous works and intending to isolate thickness effects.

Low dimensionality enters the phase diagram at least in two ways: on one side, the reduction of thickness breaks the long-range periodicity of the charge and orbital orders and the balance of interactions between the Fe sublattices; on the other, bond breaking at the surface alters the effective valence of the surface atoms and induces reconstructions that compete with the bulk order. Additional interface effects due to bond recombination or substrate-induced strain may emerge in heterostructures, but they are highly dependent on the combination of materials.

The outline of this work is as follows.

- In Chapter 1, we wil briefly show the most important aspects of the theoretical method we have used, focusing on the Kohn-Sham method

for solving the Schrödinger equation, and the parameters we have used for the different calculations performed.

- In Chapters 2 and 3, we revise the bulk properties of Fe_3O_4 and $Fe_{1-x}O$, paving the way for the study of these materials under reduced dimensions. In these sections we will see that the tendency for agglomeration of V_{Fe} acts as a precursor for the formation of short-range correlations, similar to the trimerons in magnetite.

- Chapter 4 has been divided in three sections. First, we explore the influence of the thickness on the electronic and magnetic properties of ultrathin $Fe_3O_4(001)$ films embedded in a "non-interacting" medium, with the purpose to isolate the effects induced by the reduction of thickness. In the second part, different surface reconstructions are explored in bare ultrathin films, while in the third we address the additional effects of thickness reduction.

- In Chapter 5 we will address the study of FeO(111) surfaces with two different perspectives: the presence of tetrahedrally coordinated atoms near the surface, and the influence of Fe vacancies on the surfaces of films with different terminations.

- We will end in Chapter 6 with a brief summary of the main conclusions.

Chapter 1

Theoretical background

This chapter is devoted to describe the theoretical background for the calculations carried out during the thesis period, and to justify the details of our particular computations. First, we will give a summary of the Density Functional Theory (DFT), the formalism upon which all calculations have been based. We will focus on the implementation in the VASP code, the package we have used in our work, and we will refer to the specific conditions used for the description of Fe oxides, based on previously published research and on our own investigations.

1.1 *Ab initio* methods for electronic structure calculations

The many-body problem in Solid State Physics addresses the interaction between nuclei and electrons at the atomic scale, which is described with the Schrödinger equation in Quantum Mechanics. The Born-Oppenheimer approximation exploits the fact that the ratio between electron and nucleus mass is very small, implying that the nuclei do not follow the fast electron movement[36]. Hence, the Hamiltonian that describes the system, composed by several terms that comprise the kinetic energies $\hat{T}$ and the interactions $\hat{V}$ between nuclei and electrons

$$\hat{H} = \hat{T}_{nuc} + \hat{T}_e + \hat{V}_{nuc-e} + \hat{V}_{e-e} + \hat{V}_{nuc-nuc}$$

can be expressed as the sum of an electronic-only part $\hat{H}_e$ and the nuclear parts:

$$\begin{aligned} \hat{H}_e &= \hat{T}_e + \hat{V}_{nuc-e} + \hat{V}_{e-e} \\ \hat{H} &= \hat{H}_e + \hat{T}_{nuc} + \hat{V}_{nuc-nuc} \end{aligned} \tag{1.1}$$

The term $\hat{H}_e$ couples both nuclear and electronic parts, and allows to evaluate the influence of the nuclei positions on the electronic wavefunction through the Hellmann-Feynman forces.

The numerical cost for the solution of this Hamiltonian scales exponentially with the number of electrons. There are different *ab initio* approaches to solve the stationary equation for electrons, such as the Hartree-Fock method or the DFT. They are based on the expansion of the N-electron wavefunction $\Psi(\vec{x}_1, \vec{x}_2, \ldots, \vec{x}_N)$ into Slater determinants. In the alternative DFT provides, the key feature is the particle density $\rho(\mathbf{r})$[37]. Built upon the works of Thomas and Fermi[38, 39], this theory took shape with the work of Hohenberg and Kohn[40], who provided two fundamental theorems that regard the Thomas-Fermi model as an approximation to an exact theory, the DFT, where the Hamiltonian of interacting particles in Hartree-atomic units can be written as[41]

$$\hat{H} = -\frac{1}{2}\sum \nabla_i^2 - \sum v_{\text{ext}}(\mathbf{r}_i) + \sum_i \sum_{j \neq i} \frac{1}{|\mathbf{r}_i - \mathbf{r}_j|}; \tag{1.2}$$

$$v_{\text{ext}}(\mathbf{r}_i) = -\sum_I \frac{Z_I}{|\mathbf{r}_i - \mathbf{R}_I|}$$

where $v_{\text{ext}}(\mathbf{r}_i)$ is the external potential that includes interactions between electron and nuclei.

1.1.1 Hohenberg-Kohn (HK) theorems

The HK approach is based on two theorems:

1. The external potential is determined, within a trivial additive constant, by the electron density $\rho(\mathbf{r})$. Since ρ determines the number of electrons, it follows that $\rho(\mathbf{r})$ also determines the ground-state wave function Ψ and all other electronic properties of the system.

2. A universal functional for the energy $E[\rho(\mathbf{r})]$ can be defined in terms of ρ, and it is valid for any external potential v_{ext}

$$E[\rho(\mathbf{r})] = F_{\text{HK}}[\rho(\mathbf{r})] + \int v_{\text{ext}}(\mathbf{r})\rho(\mathbf{r})d\mathbf{r} \tag{1.3}$$

$$F_{\text{HK}} = T[\rho(\mathbf{r})] + V_{e-e}[\rho(\mathbf{r})]$$

   where $T[\rho]$ is the kinetic-energy functional (corresponding to the first term in 1.1) and $V_{e-e}[\rho]$ is the electron-electron interaction functional (third term in 1.1). The exact ground-state of the system is the global minimum of this functional, and the density that renders this minimum is $\rho_0(\mathbf{r})$, the exact ground-state density, so that

$$E_0[\rho_0(\mathbf{r})] \leq E_0[\rho(\mathbf{r})]$$

Proofs of these theorems are provided in Refs. [37, 40]. With the HK theorems, the exact evaluation of the functional F_{HK} would require us to solve the many-electron Schrödinger equation. The fundamental idea upon which all DFT calculations are based consists in finding a functional which is a good approximation to $F_{\mathrm{HK}}[\rho]$ and then searching for a density that minimizes this functional. The method developed by Kohn and Sham[42] is a practical scheme based on this idea.

1.1.2 Kohn-Sham (KS) method

The KS method uses a fictitious system of non-interacting particles that generate the same density as any given system of interacting particles, $\rho_{\mathrm{KS}}(\mathbf{r}) = \rho(\mathbf{r})$. Based on the HK theorems, the ground-state energy can be found by minimizing the energy functional $E[\rho(\mathbf{r})]$ in 1.3. Kohn and Sham separated $F_{\mathrm{HK}}[\rho]$ into a set of energy components with physical meaning, but whose explicit form is not always known:

$$\begin{aligned} F_{\mathrm{HK}}[\rho(\mathbf{r})] =& T[\rho(\mathbf{r})] + V_{e-e}[\rho(\mathbf{r})] \\ =& T[\rho(\mathbf{r})] + \frac{1}{2}\iint \frac{\rho(\mathbf{r})\rho(\mathbf{r}')}{|\mathbf{r}-\mathbf{r}'|} d\mathbf{r} d\mathbf{r}' - E_{\mathrm{xc}}[\rho(\mathbf{r})] \end{aligned}$$

and the energy functional becomes:

$$E[\rho] = T_s[\rho] + \int d\mathbf{r}\ v_{\mathrm{ext}}(\mathbf{r})\rho(\mathbf{r}) + V_{\mathrm{C}}[\rho] + E_{\mathrm{xc}}[\rho] \tag{1.4}$$

where the external potential acting on the interacting system is v_{ext} and E_{xc} is the exchange correlation energy. T_s is the KS kinetic energy of non-interacting electrons with density $\rho(\mathbf{r})$, which can be described in terms of single-particle orbitals

$$T_s[\rho] = \sum_{i=1}^{N} \int d\mathbf{r}\ \phi_i^*(\mathbf{r}) \left(-\frac{\hbar^2}{2m}\nabla^2\right) \phi_i(\mathbf{r}); \tag{1.5}$$

and V_C is the Coulomb energy

$$V_C = \frac{1}{2}\int d\mathbf{r} \int d\mathbf{r}' \frac{\rho(\mathbf{r})\rho(\mathbf{r}')}{|\mathbf{r}-\mathbf{r}'|}$$

corresponding to the electron-electron interaction, equal to the classical electrostatic energy of the charge distribution $\rho(\mathbf{r})$.

The next step is to evaluate each term in 1.4. For a system of N electrons, one can construct a wave function from the single-particle orbitals $\phi_i(\mathbf{r})(i = 1, 2, ..., N)$ using a single Slater determinant, and the electron density becomes

$$\rho(\mathbf{r}) = \sum_{i=1}^{N} |\phi_i|^2$$

and expressing 1.4 in terms of single-particle orbitals, we arrive to the central equation in KS-DFT:

$$\hat{h}_i^{\mathrm{KS}}\phi_i(\mathbf{r}) = \epsilon_i\phi_i(\mathbf{r}),$$

where the one-electron Hamiltonian follows the form

$$\hat{h}_i^{\mathrm{KS}} = -\frac{1}{2}\nabla^2 + v_{\mathrm{H}}(\mathbf{r}) + v_{\mathrm{xc}}(\mathbf{r}) + v_{\mathrm{ext}}(\mathbf{r}) \tag{1.6}$$

The last three terms in 1.6 define a single-effective potential v_{eff}, where the exchange potential is given by

$$v_{\mathrm{xc}}(\mathbf{r}) = \frac{\delta E_{\mathrm{xc}}[\rho(\mathbf{r})]}{\delta\rho(\mathbf{r})}$$

An finally, the KS equation is expressed as

$$\left(-\frac{1}{2}\nabla^2 + v_{\mathrm{eff}}\right)\phi^2 = \epsilon_i\phi_i$$

DFT calculations within the KS method involve searching for a ρ that minimizes this functional, and since v_{eff} still depends on ρ, they must be solved self-consistently. Up to this point, the KS-DFT formalism is "exact" within the non-relativistic Born-Oppenheimer approximation. In fact, the only remaining part is the explicit evaluation of the exchange-correlation functional $E_{\mathrm{xc}}[\rho(\mathbf{r})]$, for which approximations are necessary.

1.1.3 Exchange-correlation approximations

The exchange-correlation energy can be rewritten as the sum of an exchange part and a correlation part. The most popular approach in the field of DFT functional development, the so-called Jacob's ladder[43, 44], consists on the gradual introduction of parameters or arguments in the exchange-correlation potential while keeping the *ab initio* spirit:

- L(S)DA - Local (spin) density approximation:

$$E_{\mathrm{xc}}^{LSDA}[\rho] = \int \rho\varepsilon_{\mathrm{xc}}^{\mathrm{unif}}(\rho)d\mathbf{r} \tag{1.7}$$

  where $\varepsilon_{\mathrm{xc}}^{\mathrm{unif}}$ is the exchange-correlation energy per particle of a uniform electron gas with uniform spin densities $n_\uparrow$ and $n_\downarrow$. Parametrizations of $\varepsilon_{\mathrm{xc}}$ are found in Refs. [45, 46]. This approximation is less accurate for atoms and molecules than for solids, since isolated systems bear less resemblance to a uniform electron gas and are better described by the functionals on higher rungs of Jacob's ladder.

- GGA - Generalized gradient approximation:

$$E_{\rm xc}^{GGA}[n_\uparrow, n_\downarrow] = \int \rho \varepsilon_{\rm xc}^{\rm GGA}(n_\uparrow, n_\downarrow \nabla n_\uparrow, \nabla n_\downarrow) d\mathbf{r} \tag{1.8}$$

  Now the density gradients have been introduced as additional local ingredients of $\varepsilon_{\rm xc}^{GGA}$, based on the second-order gradient expansion of the exchange-correlation functional. This approximation is more accurate than LDA, and it is the one we have used in our calculations, in the modified Perdew-Burke-Erzenhof parametrization[47]. Though LDA and GGA have been the most extensively used approximations, partly due to the affordable computational cost, the hierarchy of the ladder can be continued adding other corrections, such as Laplacians or the KS kinetic energy densities, leading to meta-GGA approximations and beyond, as sketched in Fig. 1.2, and increasing the computational challenge.

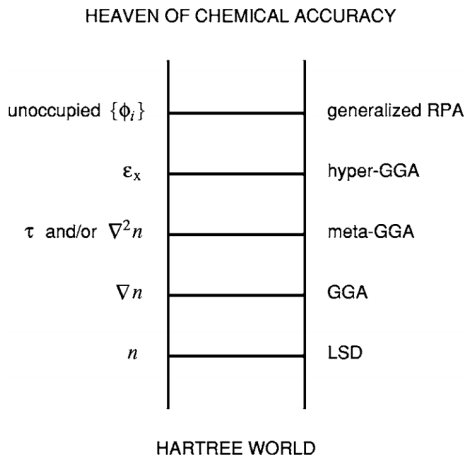

Figure 1.1: Jacob's ladder of density functional approximations to the exchange-correlation energy[43].

This allows to connect some well-known failures of LDA and GGA to describe materials with important electronic correlations, such as those in this thesis. Often, these methods are called post-DFT, and though they are not used in our work, it is worth to mention one of these approaches, that tries to combine DFT and Hartree-Fock formalism by building a hybrid exchange-correlation functional based on introducing a linear combination of the Hartree-Fock exact exchange functional

$$E_x^{\rm HF} = -\frac{1}{2} \sum_{i,j} \iint \psi_i^*(\mathbf{r}_1) \psi_j^*(\mathbf{r}_1) \frac{1}{r_{12}} \psi_i(\mathbf{r}_2) \psi_j(\mathbf{r}_2) d\mathbf{r}_1 d\mathbf{r}_2 \tag{1.9}$$

and a number of exchange and correlation explicit density functionals from other sources. The parameters determining the weight of each individual functional are specified by fitting the predictions to experimental or accurately calculated thermochemical data.

But the most popular method to incorporate, at least partially, electron-electron correlations within the DFT description is the DFT+U method, that allows to retain a moderate computational cost by introducing parametrizations in the theory. In this extension to the DFT theory, a strong intra-atomic interaction in a (screened) Hartree-Fock like manner is introduced as an on-site replacement. This can be understood as adding a penalty functional to the DFT total energy expression, and corrects the fact that all electrons in a crystal feel an average of the Coulombic potential, which for highly correlated materials turns into an underestimation of the large Coulombic repulsion between localized electrons. We have used the rotationally invariant Dudarev approach to the previously mentioned PBE parametrization of the GGA in our calculations, in which the Coulomb (U) and exchange (J) electron interactions terms enter as the difference ($U-J$), and thus only one parameter is required. In our description of ferrous oxides, we have applied this U only to the Fe d valence electrons.

Dudarev used the following Hamiltonian to describe $3d$ electrons localized on nickel sites in NiO:

$$\hat{H} = \frac{\bar{U}}{2} \sum_{m,m',\sigma} \hat{n}_{m,\sigma}\hat{n}_{m',-\sigma} + \frac{\bar{U}-\bar{J}}{2} \sum_{m\neq m',\sigma} \hat{n}_{m,\sigma}\hat{n}_{m',\sigma}$$

where $\hat{n}_\sigma = \hat{a}^\dagger_\sigma \hat{a}_\sigma$ is the operator for the number of electrons occupying a particular site, n_σ is its expectation value, and the summation is performed over projections of the orbital momentum ($m, m' = -2, -1, \cdots, 2$ in the case of d electrons); $\bar{U}$ and $\bar{J}$ are the spherically averaged matrix elements of the screened Coulomb and exchange electron-electron interactions.

The DFT+U functional is obtained after substracting the expectation value of this Hamiltonian for non-integer and integer occupation numbers:

$$E_{DFT+U} = E_{DFT} + \frac{(\bar{U}-\bar{J})}{2} \sum_\sigma (n_{m,\sigma} - n^2_{m,\sigma})$$

and the total energy is expressed in terms of the Kohn-Sham eigenvalues $\{\epsilon_i\}$ as

$$E_{DFT+U} = E_{DFT}[\{\epsilon_i\}] + \frac{\bar{U}-\bar{J}}{2} \sum_{i,j,\sigma} \rho^\sigma_{lj}\rho^\sigma_{lj} \tag{1.10}$$

where the last term represents the double counting correcion. In this approximation only the difference $(U-J)$ is meaningful.

1.2 Building the wave-function

1.2.1 Pseudopotential approximations

In principle, the Schrödinger equation contains all electrons in an atom. A further approximation to solve it can be based upon the observation that the core electrons of an atom are relatively unaffected by its chemical environment. They are strongly bound and do not play a significant role in the chemical binding of atoms, unlike the valence electrons, which contribute to a much larger fraction of the total binding energy[48].

The core electrons can be described by atomic wave functions, and since they are eigenstates of the atomic Hamiltonian, they must all be mutually orthogonal. The valence electrons oscillate rapidly (which brings convergence problems) in the core region in order to maintain this orthogonality, and hence their kinetic energy cancels the large potential energy due to the strong Coulomb potential near the core. Thus the valence electrons are much more weakly bound than the core electrons.

It is therefore convenient to attempt to replace the strong Coulomb potential and core electrons by an effective pseudopotential which is much weaker, and replace the valence electron wave-functions, which oscillate rapidly in the core region, by pseudo-wave-functions, which vary smoothly in the core region[49, 50].

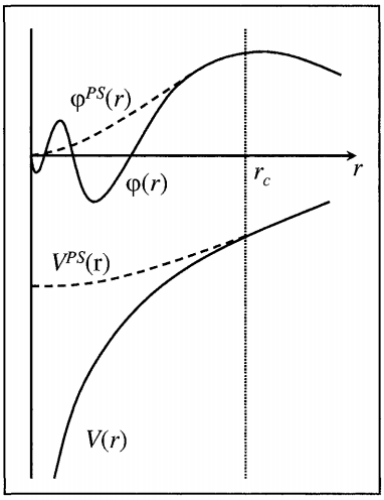

Figure 1.2: Schematic illustration of the replacement of the all-electron wavefunction and core potential by a pseudo-wavefunction and a pseudopotential[51].

In our calculations we have used the projector augmented-wave (PAW) method together with a plane wave basis set. The PAW method was introduced by Bloĉhl[52], and consists in mapping, exactly in principle, pseudo-

wave-functions described by plane waves to all-electron wave functions whose rapid oscillations close to the nuclei are treated by introducing spheres about each atom and radial grids inside these spheres. The mapping is carried out with the help of a set of partial waves and projectors calculated in the isolated atoms, and it is exact in the limit of a large number of partial waves, but in practice a compromise must be made between the partial-wave set completeness and the computational efficiency[52, 53].

1.2.2 Basis set

Different basis sets can be used to describe the wavefunctions. The VASP code expresses them in plane-waves basis sets, which offer a straightforward implementation of the KS equations for crystalline solids.

The periodicity of the crystal lattice imposes a translational invariance to the single particle wavefunctions

$$\phi_{n,\mathbf{k}}(\mathbf{r}+\boldsymbol{\tau}) = \phi_{n,\mathbf{k}}(\mathbf{r})e^{i\mathbf{r}\cdot\boldsymbol{\tau}}$$

which are indexed with $\mathbf{k}$, a vector in the Brillouin zone. The Bloch theorem implies that the single electron wave-functions observe this equation when $\boldsymbol{\tau}$ is any transitional vector leaving the Hamiltonian invariant. The most general solution that satisfies this boundary condition is

$$\begin{aligned}\phi_{\mathbf{k}}(\mathbf{r}) &= \mathrm{e}^{i}(\mathbf{k}\cdot\mathbf{r})\sum_{\mathbf{G}} C_{\mathbf{G}}(\mathbf{k})\mathrm{e}^{i\mathbf{G}\cdot\mathbf{r}} \\ &= \mathrm{e}^{i}(\mathbf{k}\cdot\mathbf{r})w(\mathbf{k},\mathbf{r}) \end{aligned} \tag{1.11}$$

where the $\mathbf{G}$ are reciprocal lattice vectors, and $\langle\mathbf{G}+\mathbf{k}|\phi_{\mathbf{k}}\rangle = C_{\mathbf{G}}(\mathbf{k})$.

The charge density is then determined by integrating over the entire Brillouin zone and summing over the filled bands

$$\rho_e(\mathbf{r}) = \sum_{n}^{\infty}\int d^3\mathbf{k} f_{n,\mathbf{k}}\phi_{n,\mathbf{k}}(\mathbf{r})\phi^*_{n,\mathbf{k}}(\mathbf{r}) \tag{1.12}$$

where the charge density is cell periodic and

$$f_{n,\mathbf{k}} = [1+\exp(\beta(\varepsilon_{n,\mathbf{k}}-\varepsilon_f))]^{-1} \tag{1.13}$$

are the Fermi-weights. Then the KS-DFT equations are given by

$$\left(-\frac{1}{2}\Delta + V_{\text{eff}}\left(\mathbf{r},\{\rho_e(\mathbf{r})\}\right)\right)\Psi_{n,\mathbf{k}}(\mathbf{r}) = \varepsilon_{n,\mathbf{k}}\Psi_{n,\mathbf{k}}(\mathbf{r}) \tag{1.14}$$

where the effective potential depends on the electronic and ionic charge distributions

$$V_{\text{eff}}(\mathbf{r},\{\rho_e(\mathbf{r}')\}) = e^2\int\frac{\rho_e(\mathbf{r}')+\rho_{ion}(\mathbf{r}')}{|\mathbf{r}-\mathbf{r}'|}d^3\mathbf{r}' + V_{\text{xc}}(\rho_e(\mathbf{r})) \tag{1.15}$$

In practice, those plane waves $|\mathbf{G}+\mathbf{k}|$ which satisfy

$$\frac{\hbar^2}{2m_e}|\mathbf{G}+\mathbf{k}|^2 < E_{cutoff} \tag{1.16}$$

are included. Plane waves are convenient for many reasons. Traditionally, because many elements exhibit a band-structure that can be interpreted in a free electron picture (metallic s and p elements) and the pseudopotential theory was initially developed to cope with these elements (pseudopotential perturbation theory). Also, because they ease the implementation of the total energy expressions and the Hamiltonian H, offering a simple and efficient method of evaluation using the fast Fourier transform (FFT)[54].

1.3 Computational details of our calculations

In this thesis, we have performed *ab initio* calculations within DFT as implemented in the VASP code[54, 55]. VASP is a complex package for performing ab initio quantum-mechanical molecular dynamics (MD) simulations using pseudopotentials or the projector-augmented wave (PAW) method and a plane-wave basis set. The approach implemented in VASP is based on the (finite-temperature) L(S)DA or GGA with the free energy as variational quantity.

1.3.1 Exchange-correlation functionals

For the exchange correlation functional, we have used the Perdew-Burke-Erzenhof (PBE) parametrization of the GGA, modified for solids (PBE-Sol)[56]. The LSDA and GGA approximations describe incorrectly the ground state of intermediate $3d$ transition-metal monoxides, as FeO[83], which has been our object of study. Their prediction is that they are metals, when in reality they are insulators with well developed correlation gaps[58]. Several extensions to the DFT theory have been proposed to retrieve an insulating gap state for these compounds, such as self-interaction corrected LDA[59, 60], LDA+U[83] or the orbital polatization correction in a crystal field basis[61]. We have used the Dudarev approach to the LDA+U method[62], in which the on-site Coulomb interaction between d electrons (characterized by the Hubbard U) enters this method as the difference $(U-J)$. The value of U has been carefully adjusted for each structure under study, as will be detailed on the corresponding sections.

1.3.2 Unit cells

Our approach to describe the system under study is based on slab models. Imposing 3D periodicity to the unit cell trivially allows to describe bulk crystals. For surfaces, a vacuum region is introduced between opposite sides

of the slab by stretching one of the lattice vectors (in the direction perpendicular to the surface). The minimum vacuum size is always more than 12 Å, necessary to avoid interaction between the slab edges. Also, in order to model the surface of bulk crystals, a minimum slab thickness is required to recover bulk-like properties at inner layers.

The Brillouin zone (BZ) has been sampled using Monkhorst-Pack grids[63], where the number of subdivisions N_i along each reciprocal lattice vector $\mathbf{b}_i$ is entered manually, shifting off from Γ whenever we set an even number of subdivisions.:

$$\mathbf{k} = \mathbf{b}_1 \frac{n_1 + 1/2}{N_1} + \mathbf{b}_2 \frac{n_2 + 1/2}{N_2} + \mathbf{b}_3 \frac{n_3 + 1/2}{N_3};$$
$$n_i = 0, \cdots, N_i - 1$$

The sampling of the BZ has been chosen in order to guarantee convergence in the total energy better than 0.1meV/f.u..

The equilibrium structure of each system under study has been found by allowing the relaxation of the lattice vectors and atomic positions. We will comment in each case the particular conditions of these relaxations. In general, they have been performed until the forces on all atoms were ≤ 0.01eV/Å.

1.3.3 Bader charges

When solving the Schrödinger equation, if a spatial basis set like plane-waves is used, the wavefunction belongs to the whole system but not to individual atoms. In this case, defining boundaries which partition the electronic charge density (and any other quantity derived from it) between the atoms can be useful for calculating the atomic contributions to the electronic charge.

Bader's theory[64] exploits the topological properties of the charge density to partition the space in several regions, each of which surrounds a nucleus. Typically in molecular systems, the charge density reaches a minimum between atoms and this is a natural place to separate atoms from each other. The boundary of each Bader volume is defined as the surface through which the charge density gradient has a zero flux.

For the Bader charge calculation, we have used the algorithm developed by A. Arnaldsson, W. Tang, S. Chill, and G. Henkelman[65, 66, 67].

1.3.4 Surface Polarity

Whenever polar surfaces are calculated, a linear electrostatic potential has been added to the local potential, correcting the errors introduced by the periodic boundary conditions[68]. These errors come from the artificial dipole that results from having two charged surfaces. By adding that potential, the

leading errors in the forces are corrected, and the work-function can be evaluated for asymmetric slabs. The minimum vacuum previously mentioned is also necessary in order to determine the dipole with sufficient accuracy. Another method we have used to correct the artificial dipoles that might emerge consists in building slabs supported on a substrate.

Chapter 2

Bulk Fe_3O_4

Magnetite is a fascinating material for understanding the fundamental physics that emerge from electronic correlations. As mentioned in the Introduction, novel technologies related to oxide electronics rely on its unique features, such as high temperature spin polarization and robust ferrimagnetism.

Above T_V, magnetite crystallizes in the inverse spinel structure sketched in Fig. 2.1, where a +3 valence is assigned to Fe_A (purple in Fig. 2.1), while a mean +2.5 valence corresponds to Fe_B (blue in Fig. 2.1) in order to achieve charge neutrality ($Fe^{3+}[Fe^{2.5+}]_2O_4$). Actually, a dynamical charge disproportionation seems to exist between Fe_B atoms, and the conductivity is mediated by an effective electron hopping between different Fe_B sites[69, 70]. Fe_A and Fe_B sublattices are coupled antiferromagnetically and the magnetic moment is carried mainly by the spin component, although there is evidence that the presence of strong correlation effects contributes to a non-quenched orbital moment[71, 72]. The magnetic exchange coupling is governed by the O-mediated superexchange mechanism, with a dominance of the J_{AB} exchange constants over J_{BB} and J_{AA}[73, 74]. A ferromagnetic double exchange contribution affects J_{BB}, which is sensitive to spin-charge coupling phenomena[75]. Half-metallicity was unambiguosly predicted from early *ab initio* calculations[76], and though its experimental identification is difficult and controversial[77, 78] it seems to be confirmed from recent measurements based on different techniques[79].

Magnetite undergoes a first-order transition (Verwey transition - VT) at the critical temperature $T_V \sim 120$K[22]. The structural modification from the $Fd\bar{3}m$ symmetry towards a monoclinic structure is sketched in Fig. 2.1. The decrease of the conductivity below T_V is assigned to the freezing of the electron hopping between different Fe_B sites, with a slightly enhanced (Fe^{3+}) or reduced (Fe^{2+}) valence, which present local perturbations called trimerons: these reveal as the essential short-range unit in the electronic phase transitions of magnetite[80]. Laser pump-probe experiments have created a non-equilibrium version of the VT by introducing holes in the

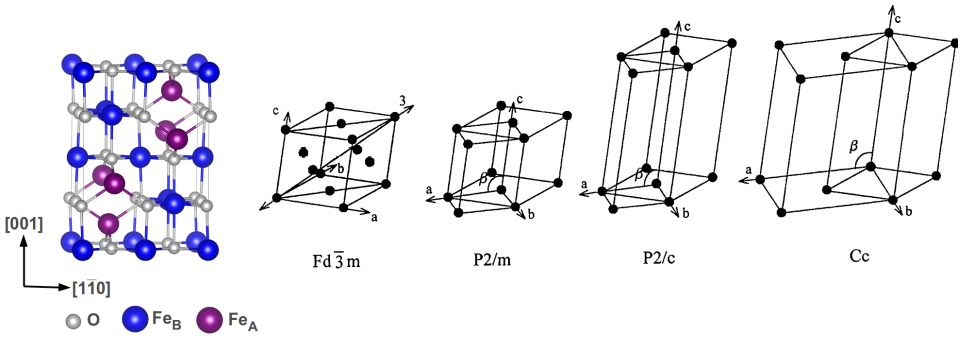

Figure 2.1: $P2/m$ unit cell used to describe bulk Fe_3O_4 and symmetry tranformations from the cubic $Fd\bar{3}m$ unit cell towards the low temperature monoclinic unit cell Cc.

trimeron lattice[81], and this opens the possibility of obtaining analogs of the VT under sizes much lower than those required by a full Cc cell.

This chapter will address the results of *ab initio* calculations on bulk magnetite. First, we will adress the structural and electronic properties above T_V, followed by the same analysis below T_V. In the final part, charge density plots showing accumulation of charge along certain directions in the low temperature regime, which serve to identify trimerons, will be discussed.

2.1 Fe_3O_4 above T_V

The unit cell we have used for modelling has $P2/m$ symmetry and is sketched in the left side of Fig. 2.1. It is built as $(\sqrt{2}/2 \times \sqrt{2}/2 \times 1)$ times the cube $(Fd\bar{3}m)$ and contains half of its atoms. At the same time, the $P2/m$ structure can be seen as 1/8 of the monoclinic Cc unit cell. Figure 2.2 shows our description of the bulk electronic properties above T_V based on first-principles calculations using the $P2/m$ unit cell with cubic symmetry. A grid in k-space of $7 \times 7 \times 5$ was used, leading to convergence in the total energy of 1 meV. We have calculated the density of states (DOS) for U between 0 eV and 4 eV in the unrelaxed unit cell, in order to find the influence of electronic correlations in our description, and to choose the most suitable parameter to model the bulk properties.

When U is gradually increased from 0 eV, several changes occur in the electronic properties. The Bader charges in the O sites slightly grow, while charges at the Fe_B and Fe_A sites gradually decrease until they reach the values of 6.52 and 6.37, respectively. The insulating gap in the majority spin channel grows from 0.9 eV for $U = 0$ to 2.5 eV for $U = 4$. At the same time, Fe−O hybridization is reduced, leading to the increased weight of oxygen p-orbitals at the top of the valence band; for U beyond 3.6 eV,

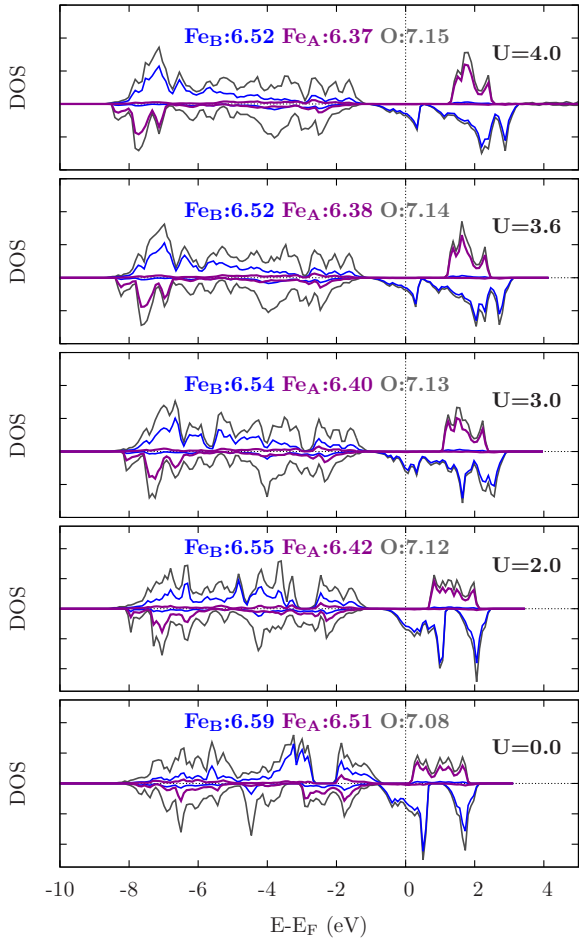

Figure 2.2: Evolution with U of the Bader charges and the spin-resolved DOS of the cubic bulk Fe_3O_4 above T_V, using the experimental lattice parameter 8.40Å. Black - total DOS of the $P2/m$ supercell. Violet and blue - Fe_B and Fe_A contributions. Positive (negative) DOS values correspond to majority (minority) spin projections.

a gap emerges at the conduction band right above E_F in the minority spin channel.

The inclusion of U also alters the structural properties. We have allowed the relaxation of lattice vectors and atomic positions for all values of U shown in Fig. 2.2. In the absence of U, the equilibrium lattice parameter a corresponds to 8.28 Å, and its value grows with U, reaching the experimental value, $a = 8.40$ Å, for $U = 4$ eV. Accordingly, we have chosen $U = 4$eV as the most suitable value for the description of bulk magnetite above T_V. This U is not far from the values used in previous calculations[76, 82], and we will see later that it also describes well most properties of the phase below T_V.

After the full relaxation for $U = 4$ eV, several structural modifications occur, and they are summarized in Table 2.1. In it, we show the average interatomic distances between first-neighbors Fe_B−Fe_B and both average Fe_B and Fe_A distances to their surrounding oxygens. Before the relaxation we found big differences between the forces acting on the oxygens (∼1 eV/Å) and on the irons (<1 meV/Å); indeed, Table 2.1 evidences that the change after relaxation is more pronounced in the O-sublattice. This oxygen movement is accompanied by a 0.12 $Å^3$/ion reduction of the unit cell total volume, and a slight decrease of the [001] lattice vector.

Table 2.1: Average interatomic distances between Fe−Fe and Fe−O in bulk Fe_3O_4 above T_V.

d(Å)	$d(Fe_B-Fe_B)$	$d(Fe_B-O)$	$d(Fe_A-O)$
before relax.	2.97	2.10	1.82
after relax.	2.96±0.00	2.05±0.02	1.89±0.00

The DOS corresponding to the relaxed structure is plotted in Fig. 2.3, where we have also placed the information of the Bader charges of all atoms in the unit cell. Purple and blue lines correspond to the total contributions of Fe_A and Fe_B. As pointed out in the figure, the Fe_B t_{2g} states cross the Fermi level, that is, they are responsible of the half-metallicity. The DOS before and after relaxation are very similar, eventhough the structure is 117 meV/f.u. more stable after relaxation. Comparing to Fig. 2.2 (case $U = 4.0$), clearly the lattice distortion is not related to the oxygen electronegativity −charge compensation−. It is also possible that the exchange constants play a role here, as it occurs in FeO. The biggest difference between both cases lies in the majority spin gap, which decreases from 2.5 eV to 2 eV. After relaxation, the Fe_B charge is sligthly enhanced, probably due to the shortened distance to the oxygens, and the total magnetic moment per formula unit remains unaltered, 4 μ_B, conserving the global magnetic

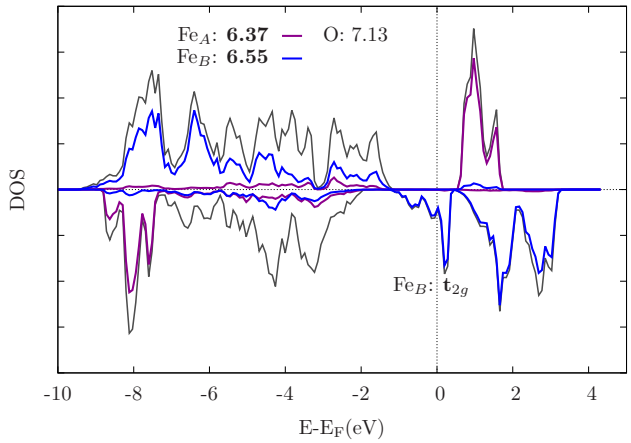

Figure 2.3: Same as Fig. 2.2 for $U = 4$, after the relaxation of lattice vectors and atomic positions.

order.

2.2 Fe_3O_4 below T_V

For the description of magnetite below the Verwey transition we have used the same parameters as above T_V, but excluding any symmetry constraints. This allows the development of U-driven asymmetries, as we will show below.

In order to find the U that better describes bulk properties below T_V, as in the previous section, we have plotted in Fig. 2.4 the evolution with U of the spin-resolved DOS in the unrelaxed system. There are 8 octahedral Fe in the unit cell and all of them have the same valence and Bader charge when $U = 0$, as they do in the phase above T_V for all the U range. When U is increased, two types of Fe_B emerge with enhanced and reduced charge, that is, with reduced and enhanced valence, Fe^{2+} and Fe^{3+}. In Fig. 2.4 we indicate in parenthesis before the corresponding Bader charges, the number of Fe sites with this charge in the unit cell. It is evident that the amount of Fe^{3+} atoms gradually grows until equilibrium between Fe^{2+} and Fe^{3+} populations is reached at $U = 3.6$ (4 Fe in each group).

The difference between both types of Fe_B is also reflected in their DOS: for $U \geq 3.6$ there is no overlap between them. The evolution of the Fe^{2+} DOS around Fermi shows a gradual opening of an insulating gap, which is occupied by the emergent Fe^{3+} t_{2g} states. On the other hand, Fe^{3+} ions show a gradual reduction of their Bader charge and a gradual shift of their majority spin states towards the bottom of the valence band (VB). These states are clearly placed below the oxygen VB for $U \geq 3.6$, reducing the O−Fe hybridization.

Two different minima very close in energy are obtained after relaxation.

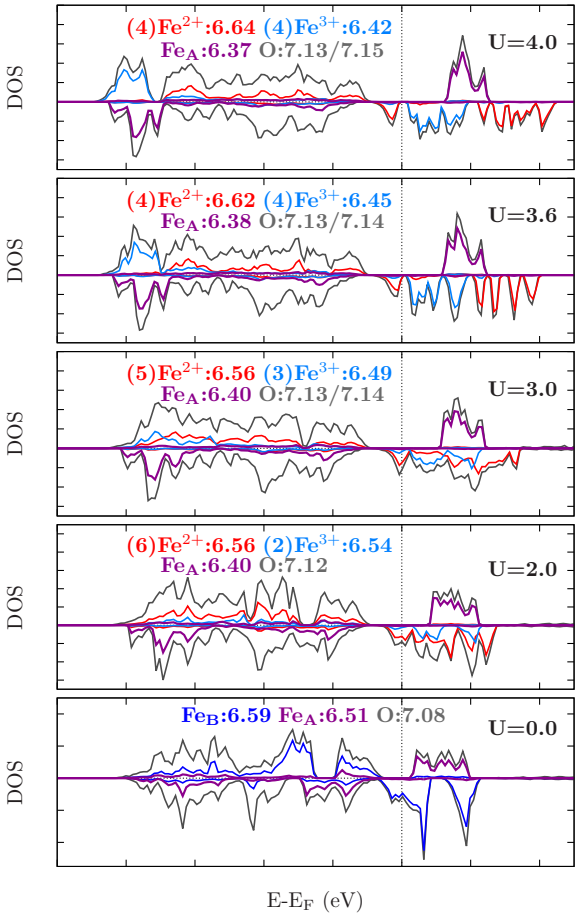

Figure 2.4: Same as Fig. 2.2 for Fe_3O_4 below T_V, using the experimental lattice parameter $a = 8.40$ Å. Black - total DOS. Blue, red, and purple - Fe_B^{2+}, Fe_B^{3+}, and Fe_A contributions.

Their existence reflects the limitations of our description with a reduced $P2/m$ symmetry, nevertheless, we can extract very interesting features of the relation between charge order (CO) and short-range order (SRO), as will be shown in the following. The unit cells obtained after relaxation, labelled S1 and S2, are sketched in Fig. 2.5. Both of them show a distortion very different from the case above T_V.

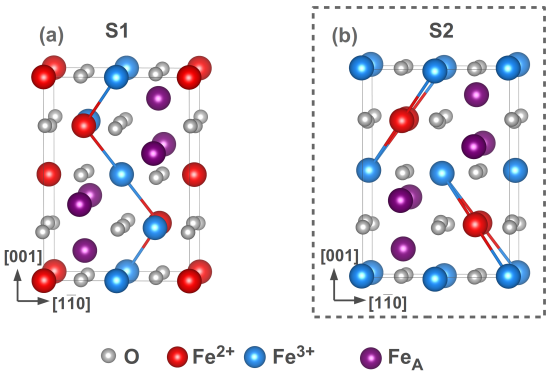

Figure 2.5: Low temperature bulk structures of lowest energy after relaxation of the cubic symmetry. Only the shortest Fe_B-Fe_B interatomic distances are drawn for each case.

Tables 2.2 and 2.3 show the average interatomic Fe−O and Fe_B-Fe_B distances to first neighbors. We can extract from Table 2.2 that, in average, oxygens are closer to Fe^{3+} than to Fe^{2+} ions. This tendency is present in both structures, but the dispersion in S2 of the average values is bigger, due to a more distorted O-sublattice. The bond Fe_A-O stretches compared to the cubic value as it did above T_V. This evidences the moderate changes of Fe_A across the VT, which is also reflected in their DOS.

Table 2.2: Average interatomic Fe−O distances and corresponding dispersion to first neighbors for structures S1 and S2.

d(Å)	$Fe^{2+}-O$	$Fe^{3+}-O$	Fe_A-O
S1	2.09±0.03	2.02±0.02	1.89±0.01
S2	2.08±0.04	2.03±0.04	1.88±0.02

The most interesting differences between S1 and S2 arise when we look at the data in Table 2.3. In it, we describe all the different Fe_B-Fe_B pairs that arise: with the same valence ($Fe^{2+}-Fe^{2+}$) and ($Fe^{3+}-Fe^{3+}$), and with different valences ($Fe^{2+}-Fe^{3+}$). Among the latter, shortened and elongated distances emerge (last column in the table). In Fig. 2.5 we have drawn these

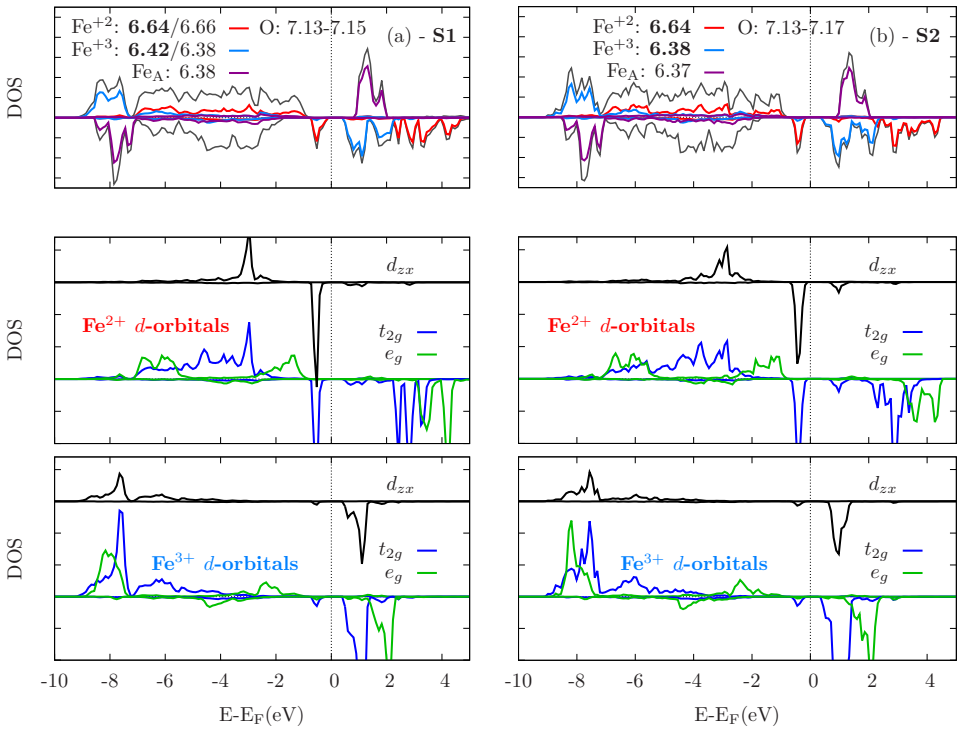

Figure 2.6: Top: same as Fig. 2.2 for the relaxed structures S1(a) and S2 (b). Middle and bottom: d-orbitals decomposition of the Fe^{2+} and Fe^{3+} atoms that share a shotened CL in the zx direction.

Table 2.3: Average interatomic Fe_B-Fe_B distances to first neighbors for structures S1 and S2.

d(Å)	($Fe^{2+}-Fe^{2+}$)	($Fe^{3+}-Fe^{3+}$)	($Fe^{2+}-Fe^{3+}$)
S1	2.95	2.98	**2.93**/2.98
S2	2.95	2.96	**2.89**/3.03

shortened connecting lines (CLs), and we see there that their distribution generates trios: Fe^{3+}−Fe^{2+}−Fe^{3+}. In S1, the Fe^{3+} on both edges of a trio connect to the next trio along the [001] direction, contrary to S2, where they connect adjacent trios always through an "elbow", breaking the continuity of the trio-line. This is due to the distribution of CO in the unit cell: in S1 there is a mixture of Fe^{2+} and Fe^{3+} on each (001) plane, while in S2 they are distributed in alternating planes. This feature in particular coincides with the first Verwey hypothesis, where the freezing of electron hopping between neighboring Fe_B sites was explained with the layered pattern obtained in S2. Also, the distribution of shortened CLs is similar to the experimental trimerons observed[27]. Last column in Table 2.3 shows that the difference between short and long CLs is more pronounced in S2 than in S1. However, the energy difference between both structures is negligible (4 meV/f.u. in favor of S1), and similarly their volumes are very close: S1 is 0.02 $Å^3$/ion bigger.

The DOS corresponding to structures S1 and S2 and the Bader charges of all atoms are in the top panels of Fig. 2.6. Compared to the cubic unit cell in Fig. 2.4, both structures show an increase of the minority spin gap (it almost doubles) and the maximum charge disproportionation between different Fe_B reaches a value of $0.28e$. In S1 only half of the Fe_B belong to a shortened trio, unlike S2, where all Fe_B are involved in them. This leads to charge variations in S1: when in a shortened chain, Fe^{2+} charge diminishes 0.02 e, while for Fe^{3+} it grows almost 0.04 e.

In the middle and bottom panels of Fig. 2.6 we have plotted the orbital decomposition of the Fe d-states of two Fe_B in a shortened chain (as depicted in Fig. 2.5) directed along the zx direction. In the central atom, Fe^{2+}, the contribution at the top of the VB is due to the t_{2g} states, more specifically, to the d_{zx} orbital. At the same time, around 1 eV in the CB, there is an accumulation of states that is enhanced in S2 (where the CLs are shorter than 2.90 Å). Regarding Fe^{3+}, we see that mostly d_{zx} and d_{yz} are contributing at the same energy as Fe^{2+} in the CB. Once again, this effect is enhanced in S2. This subtle difference is observed more clearly in the charge densities at the end of this chapter.

As it was mentioned at the beginning of the chapter, in trimerons collinear Fe_B atoms develop a polaronic distribution of shared charge, and this effect is accompanied by a hybridization among their d-states, given their reduced interatomic distances. In particular, structure S1 shows a reduction of $d(Fe^{2+}-Fe^{3+})$, but only half of the Fe_B take part in these shortened chains. And eventhough only Fe^{2+} d_{xz} orbitals are responsible for the states at the top of the VB and at the the bottom of the CB, the interatomic distance $d(Fe^{2+}-Fe^{3+})$ is not short enough to allow for a defined peak. In S2, on the other hand, the peak at the CB in the Fe^{2+} DOS is at the same position as the peak of the Fe^{3+} d_{zx} and d_{yz} orbitals. This suggests that

in S2 we should expect the presence of trimerons, given the enhancement of the hybridization features and the shortened CLs of the chains, whose length matches the average experimental value[27].

O- and Fe-sublattice distortions

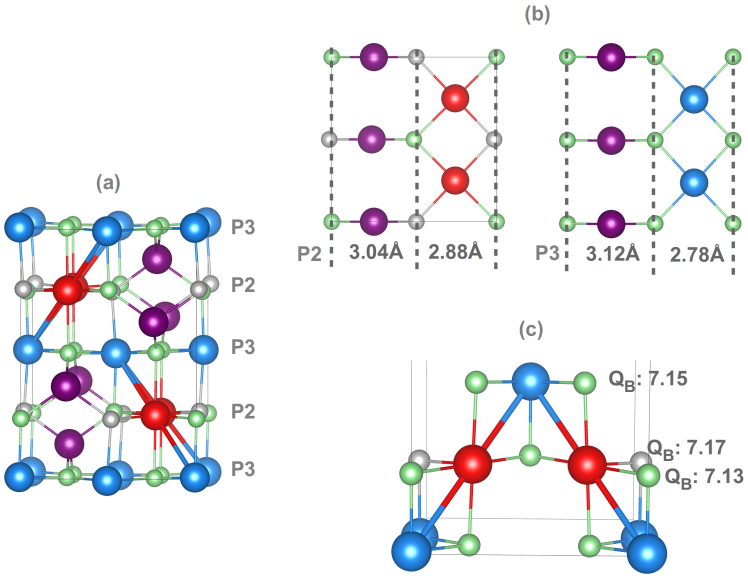

Figure 2.7: Distortion of the O-sublattice. (a) Structure S2 with Fe−O bonds and trimeron chains. (b)Top view of a Fe^{2+}−O plane and two adjacent Fe_A planes. (c) Front view of two consecutive trimerons. For clarity, oxygens on P2 linked to a trimeron are shown in green.

Apparently, the distortion in the O-sublattice does not keep any relation to lattice or charge distribution, but a closer look evidences that this is not true.

Fe_3O_4 is based on a full fcc O-sublattice with Fe_A atoms in its tetrahedral insterstices, together with an incomplete fcc Fe_B sublattice. In this spinel structure, the distribution of the Fe_B vacancies (V_{Fe_B}) and the position of the Fe_A cations ensure the homogeneity in the O−Fe bonds. All the oxygens have one O−Fe_A and three O−Fe_B bonds. As shown in Fig. 2.7(a), two types of Fe_B−O(001) planes develop in S2, formed by either Fe^{2+} or Fe^{3+}, (called P2 and P3). Given the valence-dependent Fe_B−O distances (see Table 2.2), we should expect different distortions on different planes. In Fig 2.7(b) we have sketched planes P2 and P3, where a sort of breathing mode develops for the O-O distances: oxygens separate from the voids around Fe_A and approach coplanar Fe_B rows. The extreme shortening of the O-O CLs on P3 (2.78 Å) is also present in the high temperature corresponding values:

2.79 Å and 3.12 Å. Regarding structure S1, the O−O distances on adjacent planes are more homogeneous due to the distribution of Fe^{2+} and Fe^{3+} in the cell.

Another important feature that we have observed in the O-sublattice explains the charge dispersion in it. By having a quick look on structure S2 in Fig. 2.7(a), we see that all P3 oxygens are equivalent and are bonded to Fe_B atoms within a shortened chain (coloured in green). At the same time, only half of the P2 oxygens have this type of bond (also coloured in green). As represented in Fig. 2.7(c), where we have skectched the front view of two trimerons, the P2 oxygens not bonded to the trimeron have an increased charge. The same effect is present in S1, eventhough trimerons do not form.

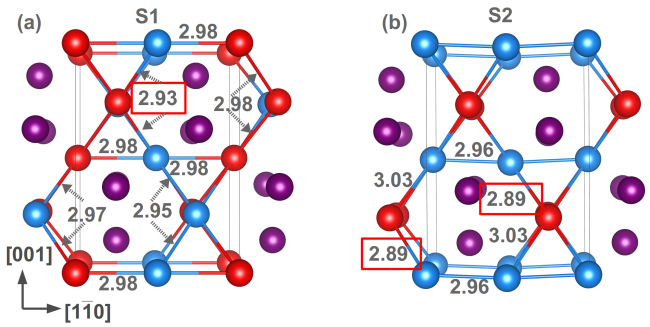

Figure 2.8: Distribution of the first Fe_B neighbors in (a) S1 and (b) S2 structures. The shortest CLs are highlighted with a red square.

As mentioned before, the Fe-sublattice in magnetite has a particular distribution of vacancies. All Fe_B are first neighbors to 6 V_{Fe_B}: two V_{Fe} are coplanar on the (001) plane, and there are two on each adjacent Fe-O(001) plane, above and below. This is better visualized in Fig. 2.8, where we have drawn all Fe_B-Fe_B CLs between first neighbors for S1 and S2. The sketch highlights the position of the voids in the unit cell. They occupy the center of hexagons defined by the CLs, that have different distributions of Fe^{2+} and Fe^{3+} and different distortions. In the right panel, which corresponds to structure S2, all the resulting hexagons are identical, and their distortion is symmetric with respect to the center of the hexagon, providing the shortening of two sides up to 2.89Å. This is not the case for S1, in the left panel, where two types of hexagons emerge with different number of Fe^{2+} and Fe^{3+}, and they distort in such a way that the maximal Fe^{2+}−Fe^{3+} shortening corresponds to 2.93Å only in the hexagon with the lower number of Fe^{3+}. This correlates the distribution of Fe^{3+} to the emergence of trimerons.

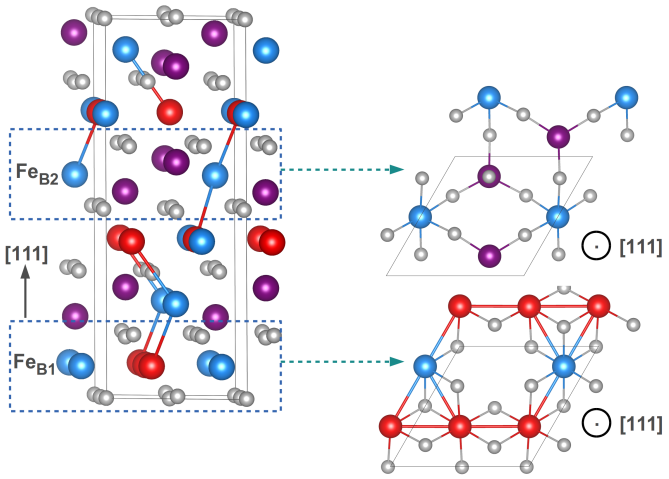

Figure 2.9: Minimum translational unit cell along the [111] direction. In the left panel, only Fe_B−Fe_B CLs shorter than 2.93 Å are drawn.

Fe_3O_4 - [111] bulk

In order to further explore magnetite bulk properties, we have studied a third structure in the low temperature range, which corresponds to the minimum translational Fe_3O_4 unit cell built along the [111] direction, as sketched in Fig. 2.9. This cell contains 1.5 times more atoms than the $P2/m$, and it can be regarded as a 2×2 Fe-deffective FeO rocksalt unit cell, where the V_{FeB} are partially compensated by Fe_A sites. As we can see in the right panel of Fig. 2.9 there are two types of Fe_B layers along the [111] axis, depending on the number of V_{Fe_B} they have. A layer with only one V_{Fe} (Fe_{B1}) and a layer with 3 V_{Fe} (Fe_{B2}). The Fe_{B2} layer, which contains only one Fe_B, is embedded between two very close Fe_A planes.

After the complete relaxation of atomic positions and vectors we find that this structure is close in energy to S2, 6 meV/f.u. less stable, but its structural distortion is slightly different to S1 and S2. Shortened Fe_B−Fe_B CLs are observed with an interatomic distance of 2.92 Å, and all the other $d(Fe_B{-}Fe_B)$ are much longer ($\sim$ 2.97 Å). As sketched in Fig. 2.9, the short-distances pattern consists of isolated non-collinear groups of three Fe_B, that look like two opposite halves of one trimeron linked together: there are two Fe^{2+} in the edges and one Fe^{3+} in the center. All the Fe^{2+} and only half of the emergent Fe^{3+} in the cell are part of this shortened pattern. The DOS of this structure, in Fig. 2.10, does not differ in general from that of S1 (in Fig. 2.6), and the tendency shown in the Bader charges is maintained, with the Fe^{3+} that are not part of shortened chains having less charge. In fact, in this structure there is a general charge decrease in the Fe^{3+} sites and a slight charge increase in the Fe_A and the O sites. The different symmetry of

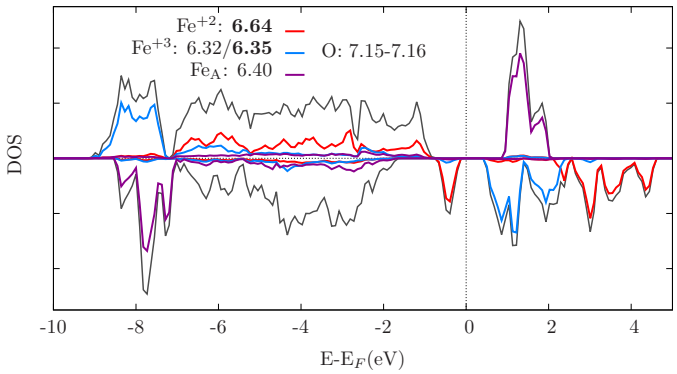

Figure 2.10: Spin-polarized DOS for the structure in Fig. 2.9.

this unit cell with respect to the $P2/m$ cell inhibits the (001) distribution of CO. As occured with S1, this reverts in the suppression of trimerons.

Summarizing, we have seen that different charge distributions and distortions can emerge in the $P2/m$ unit cell, and in the minimum translational unit cell along the [111] direction, with only a slight alteration of their relative stabilities. In S1, we have found a tendency to the creation of shortened chains across the unit cell, but not short enough to generate a clear picture of short-range correlations. On the other hand, structural modulations similar to the experimental values are found in S2, where the directionality and enhanced weight of the Fe^{2+} t_{2g} states in the CB evidences the presence of correlations. However, this configuration is very close in energy to S1.

2.3 Charge density distribution

The previous analysis has shown that when Fe^{2+} and Fe^{3+} atoms get closer than a certain threshold (around 2.90 Å), there is a hybridization between their d states with orbital directionality. In this section we will show that this hydridization corresponds to an actual accumulation of charge along the corresponding interatomic line, as evidenced by the density charge distribution (CD) on Fe planes.

We begin by analyzing structure S1. In Fig. 2.11(a) we have highlighted a blue dotted rectangle that contains the Fe_B plane under study. In the top-view of this plane, represented in Fig. 2.11(b), we see three kinds of Fe_B pairs: Fe^{2+}–Fe^{3+} at 2.93 Å (solid CL) and at 2.98 Å (dashed CL) and Fe^{3+}–Fe^{3+} at 2.98 Å (dashed CL). If the whole range of charge density values on this plane is plotted, as in Fig. 2.11(c), we see an accumulation of charge (in blue) around the atomic cores followed by a fast decay (in red) beyond them. We are interested in the interstitial region, specifically in the middle of the CLs between Fe_B neighbors, where differences in charge

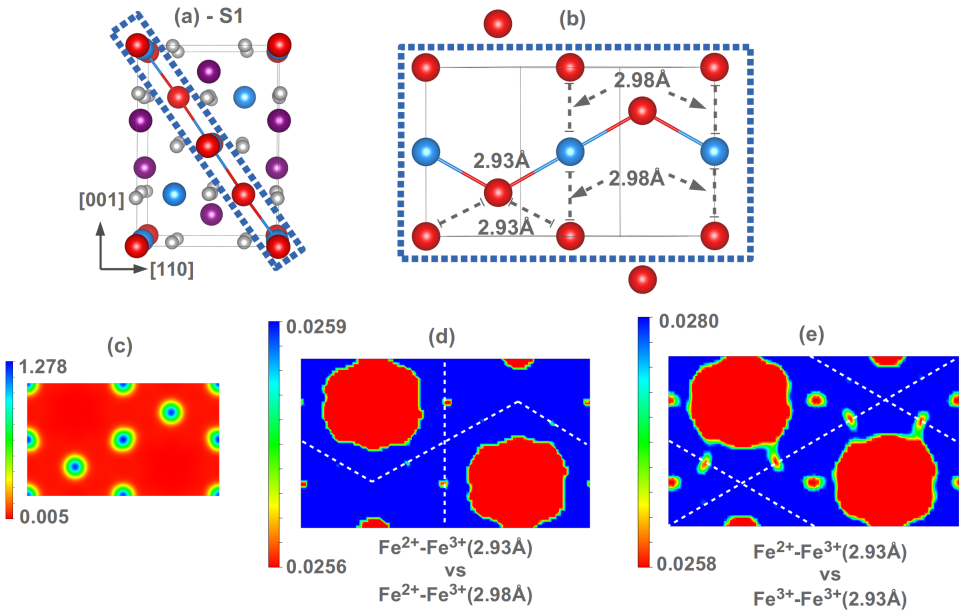

Figure 2.11: Charge density plots for S1 on the plane highlighted in (a) and sketched in (b). In (c) the total CD range is plotted, while (d) and (e) ranges are chosen to measure accurately charge accumulation along the indicated Fe_B-Fe_B lines.

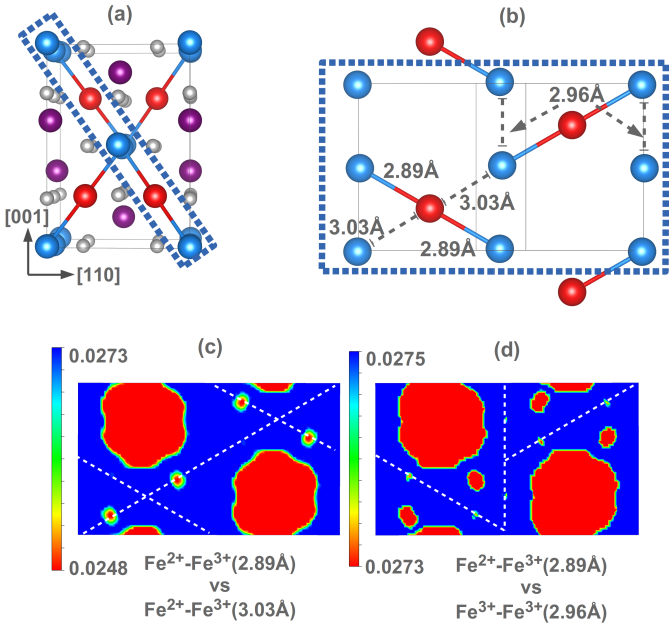

Figure 2.12: Same as Fig. 2.11 for structure S2 . It becomes evident in (c) that charge accumulates along the shortened CLs.

accumulation can be seen.

The adequate ranges of values for the comparison of either short and long $Fe^{2+}-Fe^{3+}$ CLs, or short $Fe^{2+}-Fe^{3+}$ and $Fe^{3+}-Fe^{3+}$ CLs are different. In the first case, plotted in Fig. 2.11(d), the interatomic lines under comparison are highlighted with white dots, and the plot range has been chosen in order to identify the modulation of charge in the interstitial region. If values above the minimum (0.0256) are set, red spots will emerge in the middle of the vertical long CLs. At the same time, for values below the maximum (0.0259), light blue spots will appear in the middle of short CLs. Thus, the charge accumulation in the short $Fe^{2+}-Fe^{3+}$ CL, when compared to the long one, is less than $0.0003e$. Regarding the $Fe^{3+}-Fe^{3+}$ CLs in Fig. 2.11(d) and following the same method as previously, we find an accumulation of approximately 0.0021e, one order of magnitude larger, in relation to the shortened $Fe^{2+}-Fe^{3+}$ CLs. It follows from this that along a shortened $Fe^{2+}-Fe^{3+}$ chain in S1 not the orbital character of the involved Fe, nor their charge distribution along the chain support the definition of trimerons.

Regarding S2, we have plotted the density of charge on the plane sketched in Figs. 2.12(a) and (b), that contains different Fe_B-Fe_B pairs, as sketched in Figs. 2.12(c) and (d). The results are to some extent opposite to what we found in S1. In Fig. 2.12(c), where the CD range is set to identify short and long $Fe^{2+}-Fe^{3+}$ CLs, the charge difference reaches almost $0.0025e$ essentially ten times larger than in structure S1. The inverse occurs when we set the range to match short $Fe^{2+}-Fe^{3+}$ and Fe^{3+}-Fe^{3+} CLs: the charge difference between those CLs is less than $0.0001e$. This proves the charge accumulation and the existence of trimerons in S2.

2.4 Conclusions

We have demostrated the ability to describe the bulk Fe_3O_4 properties above and below T_V with a reduced $P2/m$ cell. Also, we have provided the signatures of trimerons from *ab initio* calculations. Their existence is characterized by the simultaneous presence of three features: interatomic Fe_B-Fe_B distance shorter than 2.90 Å, orbital directionality of the t_{2g} states along the direction of the shortened distance and charge accumulation at the middle of this shortened distance, comparable to that at the interstitial region of $Fe^{3+}-Fe^{3+}$ pairs. Finally, we have also found that there is a close link between the emergence of short-range correlations and the distribution of Fe^{3+} in the Fe_B sublattice: the layered CO along the [001] direction of the Verwey model seems to favor the development of trimerons, closely linked to a lack of accumulation of adjacent Fe^{3+}. Furthermore, there is an intimate connection to the distortion and charge distribution of the O-sublattice, although the complexity of the inverse spinel structure makes this analysis difficult.

Chapter 3

Iron vacancies and clusters in bulk FeO

The mineral form of iron monoxide, wüstite, is usually described with the formula $Fe_{1-x}O$, since its structure is known to be Fe-defective. Some of its properties have already been discussed in the Introduction, such as the rock-salt structure, the antiferromagnetic (AFM) coupling between consecutive Fe-planes along the [111] direction, and the insulating character. In this chapter we will first explore the electronic properties of the non-defective FeO, and then we will focus on the presence of different vacancy arrangements throughout the cell.

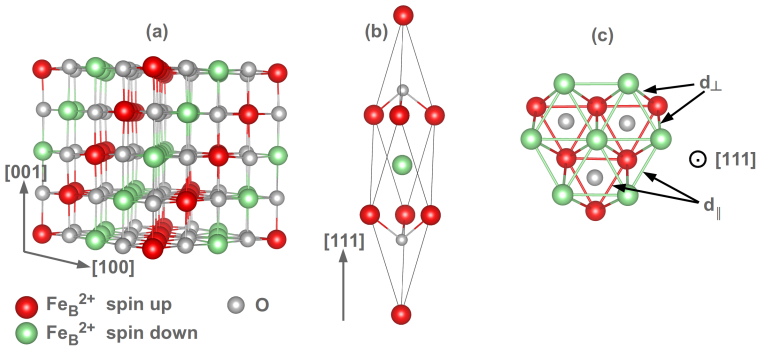

Figure 3.1: (a) FeO cubic unit cell of 64 atoms and (b) minimum unit cell with 4 atoms. (c) Top view of two adjacent Fe(111) layers with opposite spin direction (coloured in red and green), showing the interlayer ($d_\parallel$) and intralayer ($d_\perp$) distances.

3.1 Stoichiometric FeO

The electronic structure of stoichiometric wüstite has been extensively studied under different approaches, using this system as a benchmark to test models that include correlation effects[1, 83, 84, 85, 86].

A sketch of the cubic unit cell we have used for modelling is drawn in Fig. 3.1(a), where red and green layers denote Fe planes antiferromagnetically coupled along the [111] direction. This cell contains 64 atoms, and it becomes necessary to have such a big cell in order to introduce isolated Fe-vacancies, as will be shown later in this chapter. In Fig. 3.1(b), a minimum unit cell with 4 atoms along the [111] direction is also shown. We have used both cells for modelling stoichiometric FeO. In all our calculations the lattice vectors and atomic positions of the structure have been fully relaxed until the forces on all atoms were lower than 0.01 eV/Å. The Brillouin Zone (BZ) has been sampled with partitions of $2 \times 2 \times 2$ during relaxations and $4 \times 4 \times 4$ for the static calculations. When modelling stoichiometric FeO with the reduced cell in Fig. 3.1(b), a sampling of $7 \times 7 \times 7$ has been used. These partitions guarantee convergence in the total energy of 1 meV/atom.

As it was explained in the description of the theoretical method, in order to take into account the electronic correlations in strongly correlated oxides it becomes necessary to include an on-site Coulomb repulsion term U. The evolution with U of the spin-polarized DOS in the minimum unrelaxed unit cell ($a = 4.30$ Å) is sketched in Fig. 3.2. Based on the recovery of the experimental gap ($E_g = 2$ eV) and the preservation of the orbital overlap of the oxygen p band and the cation d states[1] we will restrict to $U = 4.0$ eV. With this U we also recover the experimental value for the equilibrium rocksalt lattice parameter. The opening of the insulating gap occurs for values $U \sim 2.0$ eV and above. On the other hand, the small gap at -1 eV, which separates e_g and t_{2g} Fe states, gradually decreases and almost disappears for $U = 5.0$ eV.

After full relaxation of vectors and atomic positions, our description of FeO with both unit cells in Fig. 3.1(a) and (b) is in excellent agreement with previous calculations. The lattice parameter, the electronic properties, the high local magnetic moment 3.67 μ_B, and the magnetic AF-II order, which induces a slight rhombohedral distortion[87], are recovered for both geometries. A significant deformation of the O fcc sublattice occurs, which, under the reduced symmetry of the large unit cell, enhances the dispersion of the atomically resolved properties, such as local charges and interatomic distances. This distortion lowers the total energy by 21 meV/f.u. and is related to the onset of magnetism: it does not appear in a non-magnetic calculation (where also the elongation along [111] is lost).

The total density of states (DOS) of the relaxed supercell and its projection on the Fe atoms for the big unit cell with 64 atoms are in Fig. 3.3 (top), together with the d-states decomposition on a Fe cation (bottom). It can be

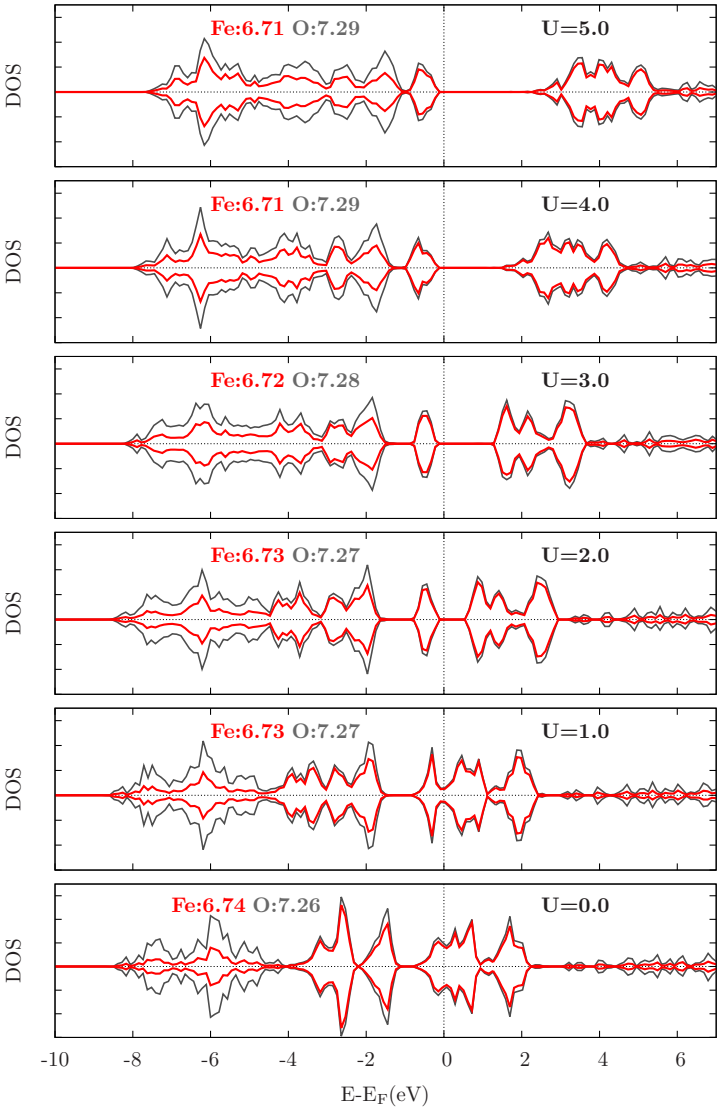

Figure 3.2: Spin-resolved DOS of FeO, using an unrelaxed rocksalt geometry, as a function of U, separating Fe and O contributions and providing Bader charges for each type of atoms.

inferred from the DOS that we obtain a perfect AFM with a total magnetic moment $\mu_B = 0$. There is a strong hybridization between O and Fe states throughout the valence band (VB) and a non-negligible contribution of O at the VB edge. Regardless of this, our description corresponds to that of a Mott insulator. In analogy with magnetite, we will call Fe_B^{2+} those irons occupying the octahedral sites in the cell. Their DOS shows an insulating gap of 2 eV between t_{2g} states, and the orbital projection on the Fe sites shows the expected separation between t_{2g} and e_g linked to the octahedral coordination.

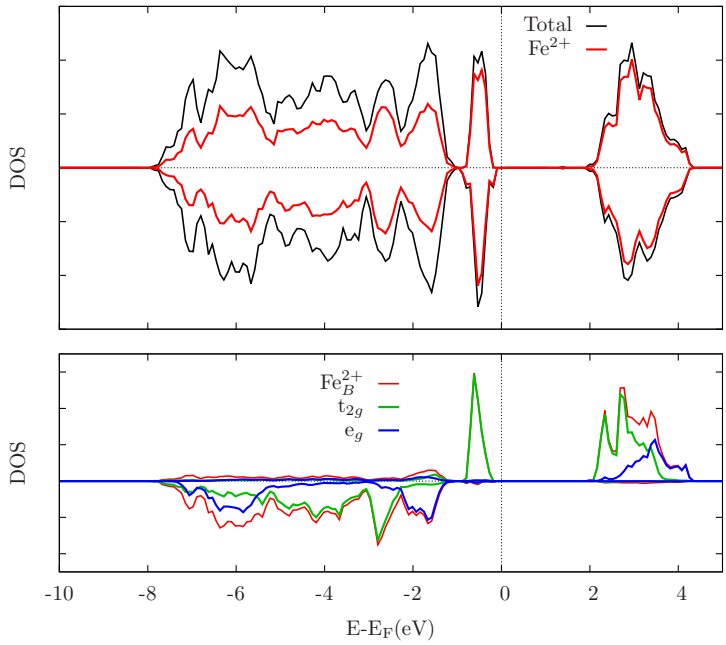

Figure 3.3: Top: spin-resolved DOS of the stoichiometric FeO where positive (negative) values correspond to majority (minority) spins. The black curve shows the total DOS and the blue is the Fe contribution. Bottom: orbital decomposition for a Fe cation, showing that the insulating gap occurs between t_{2g} states, and the separation of e_g and t_{2g} due to the octahedral coordination.

The first column in Table 3.1 shows the average values of the Bader charges and magnetic moments for Fe and O. As a consequence of the O-sublattice asymmetry local variations are found at different sites. The ionic character of the Fe−O bonds is reflected in the large charge transfer from Fe to O, and the negligible induced magnetization in the O sites comes from the perfect compensation of the Fe magnetic moments with opposite orientation, because each O is bonded to the same number of Fe↑ and Fe↓ as reflected in the DOS.

The structural properties are summarized in Tables 3.2 and 3.3. Given

Table 3.1: Mean values and dispersions of the Bader charges (Q_B) and atom resolved magnetic moments m for all considered structures.

Q_B	FeO	$Fe_{0.97}O$	3 V_{Fe}	4:1
Fe_B^{2+}	6.74±0.04	6.74±0.04	6.72±0.03	6.71±0.03
Fe_B^{3+}	–	6.43±0.02	6.39±0.02	6.43±0.03
Fe_A^{3+}	–	–	–	6.37±0.00
O	7.26±0.03	7.24±0.05	7.22±0.04	7.23±0.04
$m(\mu_B)$	FeO	$Fe_{0.97}O$	3 V_{Fe}	4:1
Fe_B^{2+}	3.67±0.00	3.67±0.02	3.67±0.02	3.68±0.03
Fe_B^{3+}	–	4.14±0.00	4.15±0.02	4.14±0.03
Fe_A^{3+}	–	–	–	4.12±0.00
O	0.01±0.01	0.03±0.02	0.05±0.04	0.05±0.04

Table 3.2: Mean values and dispersions of the in-plane ($d_\parallel$) and interlayer ($d_\perp$) interatomic Fe−Fe distances corresponding to (111) planes, for the structures in Table 3.1.

d(Fe−Fe),Å	FeO	$Fe_{0.97}O$	3 V_{Fe}	4:1
$d_\parallel$	3.03 ± 0.03	3.03 ± 0.05	3.01 ± 0.08	3.03 ± 0.08
$d_\perp$	3.05 ± 0.01	3.05 ± 0.04	3.03 ± 0.06	3.04 ± 0.06

Table 3.3: Mean values and dispersions of the Fe−O bond lengths for the different types of Fe sites at the structures in Table 3.1.

d(Fe−O),Å	FeO	$Fe_{0.97}O$	3 V_{Fe}	4:1
Fe_B^{2+}	2.15 ± 0.05	2.15 ± 0.07	2.14 ± 0.06	2.14 ± 0.07
Fe_B^{3+}	–	2.07 ± 0.05	2.05 ± 0.07	2.05 ± 0.06
Fe_A^{3+}	–	–	–	1.90 ± 0.02

that the rhombohedral distortion ascribed to FeO occurs along the [111] direction, it becomes natural to classify the distortion of the Fe-sublattice by measuring interatomic distances between first neighbors ($d(\mathrm{Fe}-\mathrm{Fe})$) parallel and perpendicular to the ferromagnetic (111) planes, as shown in Fig. 3.1(c). For example, $d_{\parallel}$ in Table 3.2 corresponds to the average Fe−Fe distances between nearest neighbors (n.n.) on the same FM plane. On the other hand, $d_{\perp}$ measures the interlayer distances, the average distance between all n.n. on adjacent AFM layers. Thus, the previously mentioned rhombohedral distortion can be deduced from the first column in Table 3.2, where $d_{\parallel}$ has a smaller value in average than $d_{\perp}$. The O sublattice is distorted in the same way as the Fe sublattice, with the same interlayer and intralayer average distances, but with larger dispersions. As a consequence of this, the Fe−O bond lenghts ($d(\mathrm{Fe}-\mathrm{O})$) have also significant variations that do not follow any particular pattern with respect to the magnetic order, as the first column of Table 3.3 shows. Nevertheless, the noticeable distortion of the FeO lattice is closely linked to the competition between the different superexchange paths. The magnetic order of the system is known to be dominated by the exchange interactions between second nearest neighbors (J_{2nn}), due to frustration of the first nearest neighbors interactions (J_{1nn})[5]. Oppositely, the rhombohedral distortion of the unit cell is caused by spin-phonon couplings governed by J_{1nn}[2]. The additional deformation of the O sublattice seems to be a mechanism to preserve maximization of J_{2nn} under the presence of the magnetically induced phonon splitting We have calculated the values of J_{1nn} and J_{2nn} in three configurations: the unrelaxed unit cell, the unit cell with only vectors relaxed, and the cell with relaxed atomic positions and lattice vectors, as in [88]. By calculating the ratio $|J_{2nn}/J_{1nn}|$ (3,5 meV, 3,5 meV, and 4,0 meV, respectively), we can conclude that the O-sublattice distortion in the fully relaxed case enhances J_{2nn}.

3.2 $Fe_{0.97}O$ - Isolated iron vacancy

Once we have analyzed the properties of stoichiometric FeO, we turn to the defective $Fe_{1-x}O$. We have first studied the configuration with one Fe vacancy (V_{Fe}) in the supercell with 64 atoms. Eventhough this concentration of vacancies ($x \sim 3\%$) is lower than the experimental range for wüstite, it allows us to isolate the structural and electronic features of non-interacting vacancies.

The creation of a vacancy in the Fe sublattice is expected to induce a change of valence on two Fe, that should act as Fe^{3+}. We label these enhanced valence cations Fe_B^{3+} in analogy to magnetite, where the irons that occupy the B sublattice (octahedrally coordinated) split into Fe_B^{2+} and Fe_B^{3+} (with Bader charges 6.37 and 6.64 respectively) below the Verwey temperature. In our particular case, the Fe_B^{3+} ions emerge among the first V_{Fe}

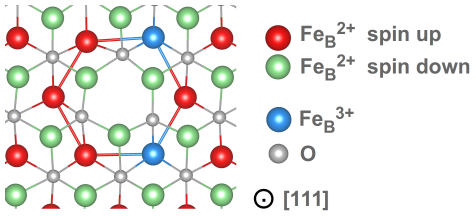

Figure 3.4: Top view of two adjacent antiferromagnetically coupled Fe(111) layers, with thick lines connecting Fe neighbors of the vacancy, highlighting its position.

neighbors and belong to the same FM layer where V_{Fe} is created (see blue cations in Fig. 3.4). In Table 3.1 we provide the average Bader charges (Q_B) and magnetic moments of all atoms in the unit cell. A slight reduction of the average O charge is noticed close to the vacancy, but the charge distribution is complex and, as a consequence of the O sublattice distortion, we may find as well O sites with similar low values of Q_B far from V_{Fe}. Accompanying the charge reduction in the Fe_B^{3+} sites as compared to the Fe_B^{2+}, we see in Table 3.1 a significant enhancement of their magnetic moment, which along with the uncompensated $\vec{m}$ at empty Fe sites, induces a slight average magnetization in the O sublattice. This leads to the partial compensation of the AF coupling in the supercell, where a net magnetization of 2 μ_B emerges. This effect, together with the reduction of the insulating gap to around 0.8 eV, represent the main differences with respect to stoichiometric FeO.

The DOS in Fig. 3.5(a) shows new states (blue line) at the gap, which correspond to the two emergent Fe_B^{3+}. Besides being responsible for the gap reduction, these new Fe_B^{3+} also provide new features at the bottom of the conduction band around -8 eV. Regardless of this, the global electronic structure of the wüstite lattice does not vary significantly, and, as we will explain below, most modifications are localized around V_{Fe}.

As a first important structural change, the oxygens tend to approach the Fe_B^{3+} sites by 0.08 Å, while the average distance to the Fe_B^{2+} ions remains approximately unchanged (second column of Table 3.3), leading to a significant distortion of the fcc O sublattice. The second relevant structural change concerns the Fe sublattice: the Fe positions around V_{Fe} are significantly rearranged. There are 12 Fe n.n. to V_{Fe} in total, 6 of them are coplanar on the (111) plane and form a hexagon around V_{Fe}, as in Fig. 3.4, and the other 6 form triangles on the top and bottom Fe-layers. The general tendency among these neighbors is to fill the void created by V_{Fe} in such a way, that the hexagon and the triangles shrink, and the latter come closer to the hexagon. From the second n.n. on, the stoichiometric distances d(Fe−Fe) are gradually restored.

This is evidenced once we analyze the distortion of the supercell. In the

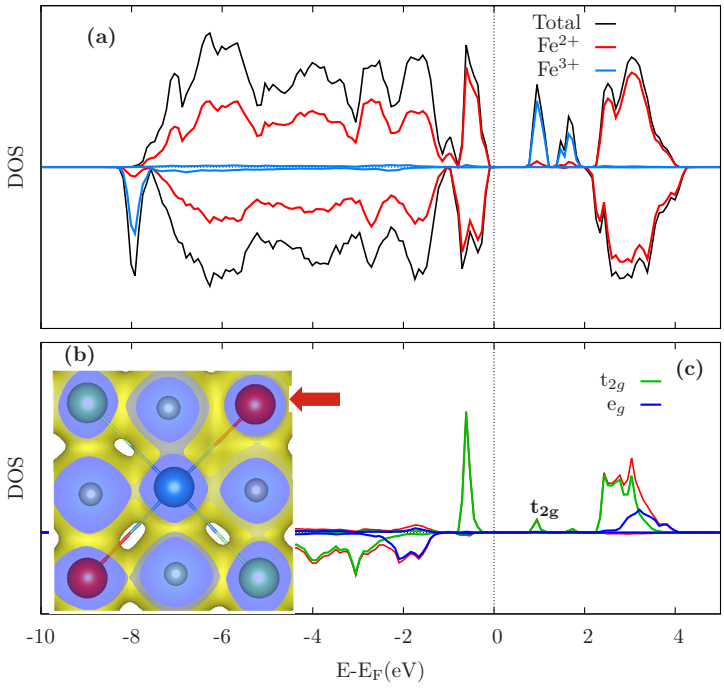

Figure 3.5: Spin-resolved DOS for $Fe_{0.97}O$ with positive (negative) values corresponding to majority (minority) spins. (a) Total DOS, Fe_B^{2+} and Fe_B^{3+} contributions. (b) Charge density around a Fe_B^{3+} site with accumulation of charge along the Fe_B^{2+}- Fe_B^{3+} connecting line. (c) DOS around the Fermi level of the Fe_B^{2+} pointed by a red arrow in panel (b), showing t_{2g} states that lie along the CL towards Fe_B^{3+}, with vertical scale 10 times smaller than for total DOS.

second column of Table 3.2 we have summarized and classified the average Fe−Fe distances as in the previous section. There is a slight reduction of the cell volume and a tendency to shorten both $d_{\parallel}$ and $d_{\perp}$, better evidenced with the histogram in Fig. 3.6, when compared to stoichioimetric FeO. Eventhough the dispersion in the values is more pronounced now, the low concentration of defects considered here does not alter the elongation along c, as evidenced by the $d_{\parallel}/d_{\perp}$ ratio, as compared to FeO. This is another manifestation of the local changes introduced by V_{Fe}, which mostly occur in its vicinity.

We did not find a regular dependency of the d(Fe−Fe) distances on the Fe valence as we found for d(Fe−O). Nevertheless, some of the Fe_B^{2+} exhibit a singular relation to their neighboring Fe_B^{3+}. In Fig. 3.5(b) we have plotted the three dimensional real space distribution of the charge density on a (010) plane that contains different Fe−Fe bonds. In this cut, a Fe_B^{3+} (central blue) is surrounded by 4 Fe_B^{2+} (in red and green - different spin direction). There is an accumulation of charge along one of the Fe_B^{2+}−Fe_B^{3+} connecting lines

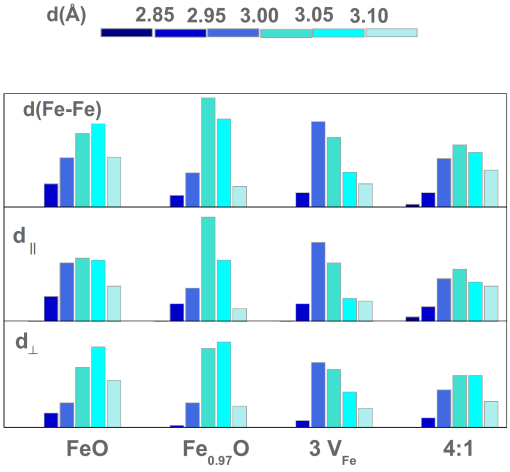

Figure 3.6: Histograms showing the distribution of d(Fe−Fe) values at the Fe_B sublattice, and sorted in $d_{\parallel}$ and $d_{\perp}$, for the structures in Table 3.1. The vertical scale of the central and bottom panels has been reduced by $\sim 30\%$ with respect to the top panel.

(CLs), which is considerably shortened to 2.87 Å, while the other $Fe_B^{2+}-Fe_B^{3+}$ pairs have CLs over 3 Å. The charge accumulation at this short CL is also present at the DOS in Fig. 3.5(c), where the states of the corresponding Fe_B^{2+} (pointed by a red arrow) are overlapping with those of the Fe_B^{3+} at the FeO gap. Analysis of the orbital character of these states shows that they have t_{2g} character and lie along the CL, in other words, they are pointing in the direction of Fe_B^{3+}. The combined presence of these features, namely: 1− shortening of the $Fe_B^{2+}-Fe_B^{3+}$ distances, and 2− presence of Fe_B^{2+} states in the FeO gap with t_{2g} orbitals along the CL, is characteristic of the short-range charge correlation units in low-temperature magnetite, the trimerons[27, 80]. We will discuss these aspects in more detail in the last section of the chapter.

The energy cost of creating a defect has been estimated as[89, 90]

$$E_c = E[Fe_{1-x}O] - E[FeO] + n\mu_{Fe} \tag{3.1}$$

where E refers to the total energy of the supercell with or without V_{Fe}, and $n\mu$ is the number of V_{Fe} times the Fe chemical potential. The limits of μ_{Fe} have been obtained from calculations of the bcc Fe and the O_2 molecule, taking into account the influence of U on Fe and the Gibbs free energies of formation of the oxide and the stable forms of its elemental constituents[91]. In this way, we can express E_c as a function of the O chemical potential μ_O, where the zero reference is set to $\mu_O = 1/2E[O_2]$. In Fig. 3.7 we have plotted this dependence, with the horizontal line at $E_c = 0$ corresponding to the stoichiometric case.

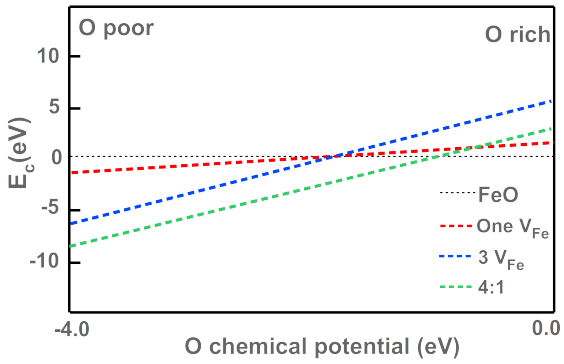

Figure 3.7: Energy cost of creating a V_{Fe} for the different structures in Table 3.1, as a function of μ_O.

3.3 $Fe_{0.906}O$– Three V_{Fe}.

In this section we will explore two different scenarios that appear when three V_{Fe} are created in the supercell, corresponding to a concentration within the experimental range for wüstite, of $x \sim 9.4\%$. In the first scenario, the V_{Fe} are maximally separated from each other. The second scenario consists in generating a 4:1 cluster, removing four Fe_B and introducing one Fe_A (in a tetrahedral site).

3.3.1 $Fe_{0.906}O$ – Isolated vacancies

The maximum separation between three V_{Fe} in our supercell can be obtained by removing one Fe from the corner of the cube and two more Fe from the middle (100) layer; they can be removed along the $[1\bar{1}0]$ or [110] diagonals, generating two systems that are geometrically identical but magnetically inequivalent because of the type-II antiferromagnetism. This situation is better visualized in Fig. 3.8, where the corresponding cubic unit cells are sketched together with all the inequivalent Fe-positions on two adjacent (111) planes with opposite spin-orientation (red and green). On top we have configuration C1: two Fe are removed along the $[1\bar{1}0]$ diagonal in the central layer, leading to 2 V_{Fe} on the red plane and 1 V_{Fe} on the green one. In the bottom we have C2: three Fe with parallel spins are removed (all the V_{Fe} are coplanar) and the magnetic imbalance is bigger.

As expected, the net magnetization is 2 μ_B for C1 and 14 μ_B for C2. Despite this large difference, the total energies for both configurations are very close, with C1 being favored over C2 by 47 meV (less than 1 meV/atom). This tendency is also manifested in the similarity of their global structural and electronic properties. There are local differences between them, but their resemblance is a proof of the weak interaction between the vacancies.

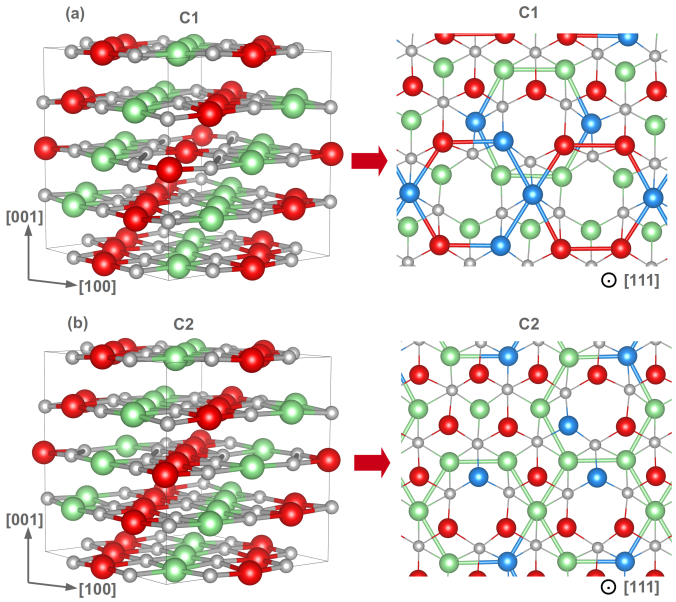

Figure 3.8: Cubic cell and top view of two adjacent Fe(111) layers in $Fe_{0.906}O$ in structures (a) C1 and (b) C2 . Emergent Fe_B^{3+} sites are coloured in blue. On C1, two V_{Fe} are coplanar and one V_{Fe} is created in the adjacent AFM plane. On C2, all three V_{Fe} are coplanar. For clarity, thick Fe−Fe lines joining the six n.n. to each V_{Fe} are drawn. The legend coincides with Fig. 3.4.

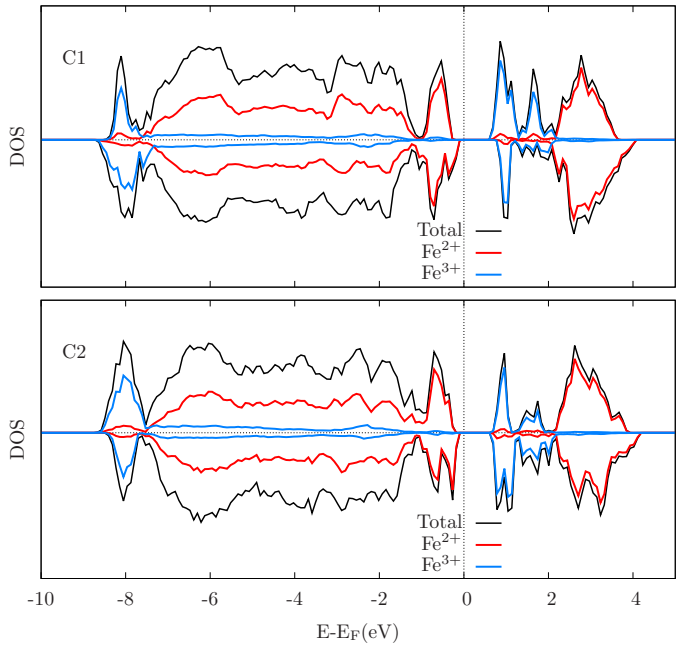

Figure 3.9: Spin-polarized DOS for structures C1 (top) and C2 (bottom).

This also allows to put limits on the minimum separation for the V_{Fe} to interact: in both structures, two V_{Fe} share one first Fe neighbor, as shown in Fig. 3.8, reaching a limit separation of $\sim$ 5.93 Å. On the other hand, regarding Fig. 3.7, this composition is more stable than FeO at low O_2 pressures, and also more stable than $Fe_{0.97}O$ when FeO becomes unstable.

The spin-polarized DOS corresponding to both structures are shown in Fig. 3.9(a) and (b), together with the projections on different types of cations. As in the previous section with one V_{Fe}, two irons with enhanced valence Fe_B^{3+} emerge per each vacancy created, and they introduce new states at the bottom of the CB and at the insulating gap, reducing it further to $\sim$ 0.5eV in both configurations. Comparing the DOS in Fig. 3.9 to the case with one V_{Fe} (Fig. 3.5), the larger amount of emerging Fe_B^{3+} sites introduces additional states at both spin orientations. In general, all features of the DOS are broader, associated to more defective structures.

The mean values of the charges and magnetic moments are summarized in the third column of Table 3.1. They correspond to structure C1, similar values are obtained for C2. The increase of V_{Fe} concentration causes a raise in the charge demand from O, resulting in a general reduction of the oxygen Bader charges. This tendency can also be understood by analyzing the positions of the Fe_B^{3+}: some of them emerge in positions where they have 2 V_{Fe} as nearest neighbors. It is also remarkable that not always the Fe_B^{3+} appear as coplanar to their closest V_{Fe}: in C2, for example, most of the Fe_B^{3+} emerge in the plane without defects (red plane in Fig. 3.8(b)) reinforcing the spin imbalance with their enhanced magnetic moments. This fact, together with the relative negligible energy difference between C1 and C2, supports the interpretation of magnetic measurements that assign to the defects local ferrimagnetic areas, which are disordered with respect to each other and also with respect to the overall AF order[11, 92].

The global structural properties, such as the mean interatomic distances, the unit cell vectors and the cell volume are very similar in both C1 and C2. The mean d(Fe−O) and d(Fe−Fe) values for C1 are in the third column of Tables 3.2 and 3.3. The average d(Fe−O) are sligthly shorter than in $Fe_{0.97}O$, as well as the volume of the supercell, whose contraction is 3 times bigger and leads to a reduced cubic lattice parameter of 4.26 Å. In Table 3.2 we notice a weakening of the rhombohedral distortion, in agreement with experimental evidence[10, 11], which is better appreciated in the histograms on Fig. 3.6, with very similar distributions for $d_{\parallel}$ and $d_{\perp}$. The larger number of V_{Fe} and the tendency of the Fe sublattice to fill the voids increases the dispersion of the interatomic distances and shifts them to shorter values. Another important effect, which has consequences on the electronic properties around the vacancies, consists in the appearance of pairs of n.n. Fe_B^{3+}−Fe_B^{3+}. As we will explore in the last section of this chapter, there is an accumulation of valence charge in their interstitial region.

3.3.2 $Fe_{0.906}O$ – Cluster 4:1

The second scenario with 3 V_{Fe} in the supercell that we have studied is the 4:1 cluster. This cluster consists in creating 4 V_{Fe} around a tetrahedrally coordinated iron, as shown in Fig. 3.10. In fact, we are creating one more V_{Fe} than before, but the addition of Fe_A balances the number of vacancies. The 4:1 cluster is expected to be the most stable configuration for moderate values of x[9]. In agreement with this, we have obtained that it lowers the energy from the isolated V_{Fe} scenario by 22 meV/atom. As we can extract from Fig. 3.7, this extends the range of stability of defective $Fe_{1-x}O$ over FeO to higher O pressures.

The side view of the supercell sketched in Fig. 3.10 reveals that Fe_A is almost coplanar to one of the FM (111) Fe layers. The top view on the right side, with two Fe(111) layers and the O layer between them, shows that all V_{Fe} are first n.n., but three of them lie on the same (111) (red) plane. We have drawn thick Fe−Fe lines in order to highlight the vacancy positions.

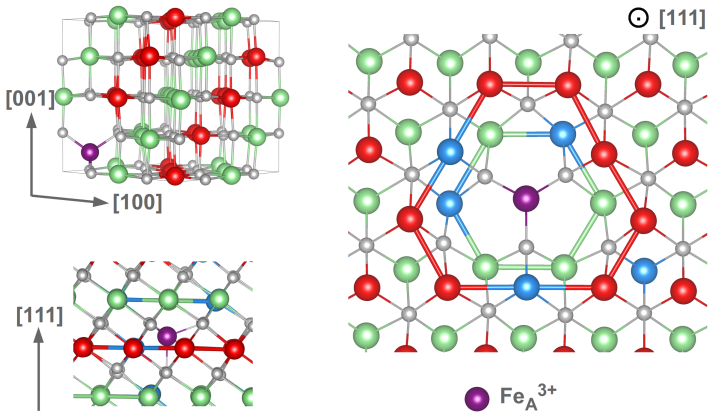

Figure 3.10: Top and side views of two Fe(111) layers around the 4:1 cluster, following the legend in Fig. 3.1. On the right and bottom left panels, thick Fe-Fe lines are drawn around the voids. The side perspective on the bottom left shows that Fe_A is almost coplanar to the plane with more V_{Fe}.

The Fe_A spin can be parallel or antiparallel to the layer with more vacancies, which leads to two magnetic configurations with very different uncompensated magnetizations: 4 μ_B and 14 μ_B. Despite this difference, both configurations show similar global properties in their ground state which reminds of the situation for C1 and C2 in section 3.3.1. Unlike that case, the relative energy difference between both configurations grows to 5 meV/atom, bigger than before but still a moderate value in favor of the situation with lower total magnetic moment. As we pointed out before, each V_{Fe} introduced in the lattice is compensated by the emergence of two Fe^{3+} atoms to ensure electroneutrality. Here, the tetrahedral Fe_A acts with enhanced

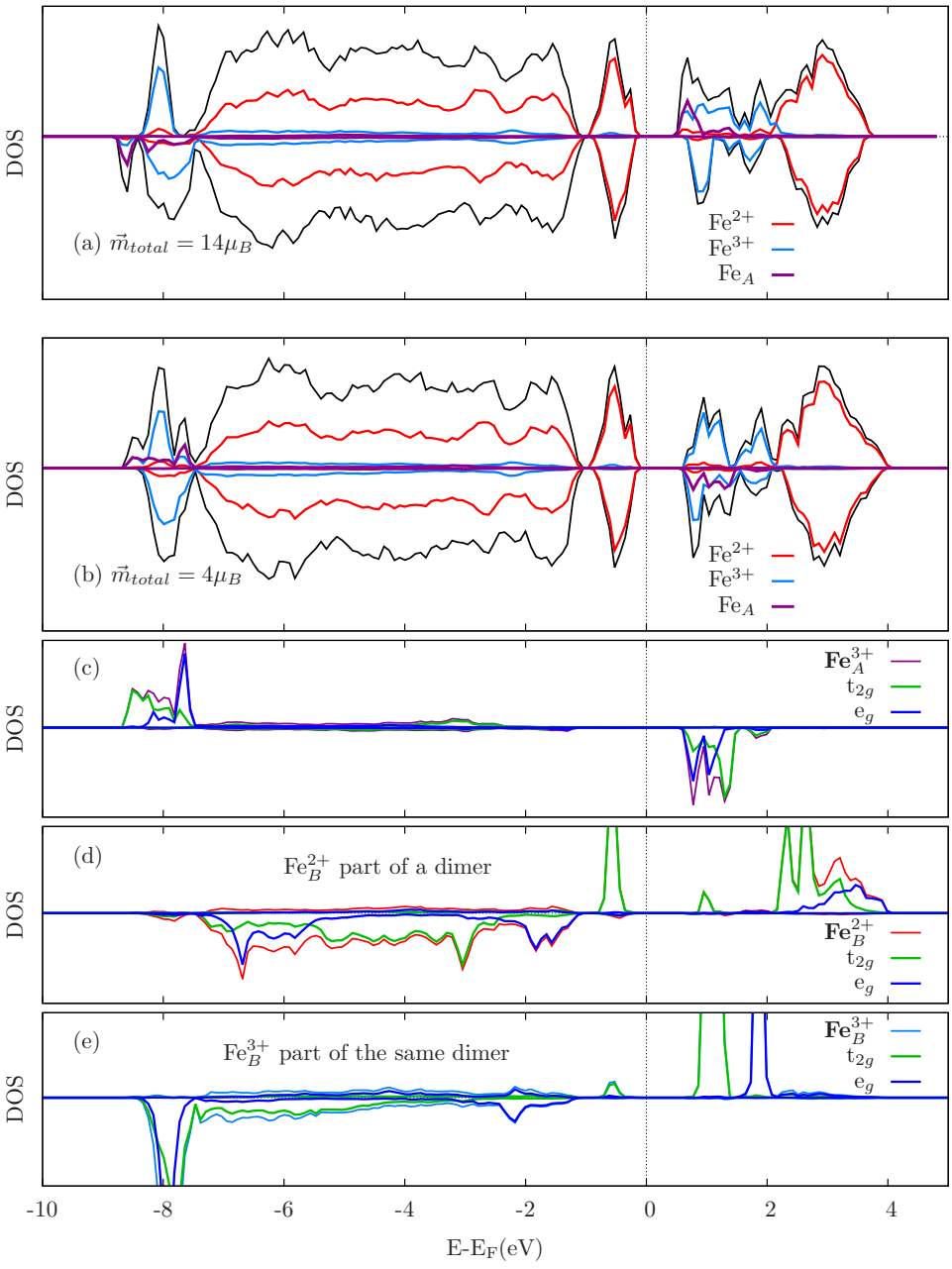

Figure 3.11: Spin-polarized DOS of the supercell containing a 4:1 cluster. (a) and (b): Total DOS and contributions from all different Fe for structures with ttotal magnetization 14 μ_B and 4 μ_B; (c),(d) and (e): Fe_A, and selected Fe_B^{2+} and Fe_B^{3+} *d*-orbital projections in structure (b). The vertical scale in (d) and (e) is three times bigger than in (c).

valence, and we obtain only 5 Fe_B^{3+}. All of the emergent Fe_B^{3+} appear as first n.n. to Fe_A and also all of them are first n.n. to two of the V_{Fe} (see Fig. 3.10).

In Fig. 3.11(a) and (b) we have plotted the DOS of both configurations and the projections on the different Fe sites, as well as the DOS for each of the different Fe types present in the most stable structure from (b). The corresponding mean Q_B values and magnetic moments are in the last column of Table 3.1. As we can see in Fig. 3.11(c) and (e), the contribution from Fe_A^{3+} almost overlaps with the contribution from the emerging Fe_B^{3+}, but with a different order in their t_{2g} and e_g states because of their different coordination. The resulting insulating gap is ~ 0.6eV. A higher degree of order in this structure, compared to the isolated vacancies dispersed throughout the supercell, can be drawn from the better resolution of the peaks in the DOS corresponding to each of the Fe sites. For example, the peaks asociated to t_{2g} and e_g states at the top of the VB for Fe_B^{2+} do not overlap, unlike in all previously considered structures with defects. Also, the vacancies are more localized in this structure, and this has consequences on the distribution of O charges: they are lower (~ 7.18) in the sites bonded to Fe_A, and far from the cluster they recover the values they have in FeO. As a result, the mean Q_B at the O sublattice is enhanced over the configuration corresponding to 3 isolated V_{Fe}. The effectiveness of the cluster to compensate globally the loss of charge seems to be the origin of its higher stability.

The formation of clusters leads to the inhomogeneous distribution of magnetic moments, since a higher magnetization is obtained in the vicinity of the defects, and the defects are first neighbors in a cluster. This is in excellent agreement with previous experiments[92], where high magnetization and low temperature coercivity have been linked to the presence of large clusters based on stacking of spinel-like defects. The difference between the magnetic moments of Fe_A^{3+} and Fe_B^{3+} is very small, as well as the induced magnetization in the O sublattice, which does not differ from the previously studied defective structures.

The mean values of the resulting interatomic distances and their dispersions are summarized in the last column of Tables 3.2 and 3.3. The average $d(Fe_B^{2+}-O)$ and $d(Fe_B^{3+}-O)$ do not change in this configuration with respect to previous values, and the average $d(Fe_A\text{-}O)$ stretches from the cubic value of 1.82 Å to 1.90 Å, similar to the value for the tetrahedral sublattice in magnetite[93]. In addition to this, some particularly short $d(Fe^{2+}-Fe^{3+})$ appear below 2.85 Å. The DOS from both components of this pair are plotted in Fig. 3.11(d) and (e), showing hybridization of the t_{2g} states along their CL. Besides this, there is a general tendency of the Fe−sublattice to shrink towards the voids and an overall reduction of the average d(Fe−Fe) followed by contraction of the volume. In fact, it is clear from the histograms in Fig. 3.6 that d(Fe−Fe) has a wider range of values in the cluster, and that the distribution has more resemblance to the stoichiometric oxide than

the structures with isolated V_{Fe}. Regardless of that similarity to FeO, the rhombohedral distortion disappears upon the increase of V_{Fe} concentration; this effect is in good agreement with experimental evidence. In general, the FeO matrix tends to recover its stoichiometric properties far from the cluster, while the agglomeration of V_{Fe} around Fe_A introduces larger local modifications than in the matrix with isolated defects.

3.4 Charge density distribution

As we have shown throughout the chapter, the irons with enhanced valence that emerge in Fe-defective structures to ensure electroneutrality are always among the first n.n. to one or more of the V_{Fe}. The tendency of the Fe sublattice to shrink around the voids brings together $Fe_B^{2+}-Fe_B^{3+}$ pairs that beyond a certain minimum interatomic distance develop a polaronic charge distribution. The electronic structure of a Fe_B^{2+} site connected to this kind of "dimer" shows the hybridization of t_{2g} states with the states of the Fe_B^{3+} at the FeO gap in the CB. This means that we can recognize structurally and electronically the new phenomena. We will provide the details of this effect in this section, based on the two-dimensional charge density (CD) on the (111) planes where the shortened CLs are located.

3.4.1 Isolated vacancies. $Fe_{0.97}O$ and $Fe_{0.906}O$

We will first adress the supercell with one V_{Fe} from section 3.2. The DOS of this structure, Fig. 3.5, showed the Fe_B^{2+} orbital directionality. Due to the fcc stacking of the Fe−sublattice, all the first and most of the second Fe n.n. to V_{Fe} are contained in a triangle with vertices on the vacancy, as sketched in Fig 3.12(a). We have plotted the full CD on this plane in Fig. 3.12(b), which spans a range between 1.285 $e/Å^3$ and 0.001 $e/Å^3$, that evidences the accumulation of charge around the center of the Fe sites and a fast decay in the interstitials. The relevant interval for polaronic charge accumulation is very narrow, as shown in Fig. 3.12(e). Usually, there is a depression of the CD at the middle of the line between two Fe neighbors. This depression is attenuated on the lines connecting the Fe_B^{3+} sites and dissapears completely in the $Fe_B^{2+}-Fe_B^{3+}$ shortened CLs. Eventhough the orbitals at the CLs with a length of 2.96Å (highlighted in the left corner of Fig. 3.12(e)) show a tendency to hybridize and directionality of their t_{2g} states, there is a visible difference in the amount of charge they share, as compared with the CL from the top of the triangle with a length of 2.88Å. This provides the length limits necessary for the development of polaronic charge sharing.

When we increase the number of isolated V_{Fe} in our supercell, as in section 3.3.1, some of the Fe_B^{3+} emerge as n.n.. In Fig. 3.13 we have plotted

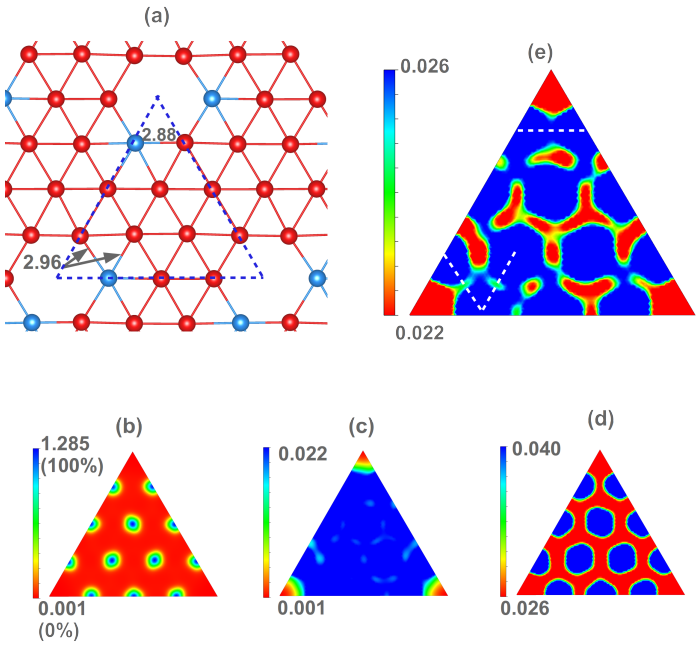

Figure 3.12: Two-dimensional slice of the charge density at the (111) plane containing the V_{Fe} in $Fe_{0.97}O$, showing on (a) the reference atomic positions. Representative interatomic distances (in Å) between Fe^{2+}−Fe^{3+} pairs are provided, and the corresponding CLs indicated by the dashed lines on the CD plots.

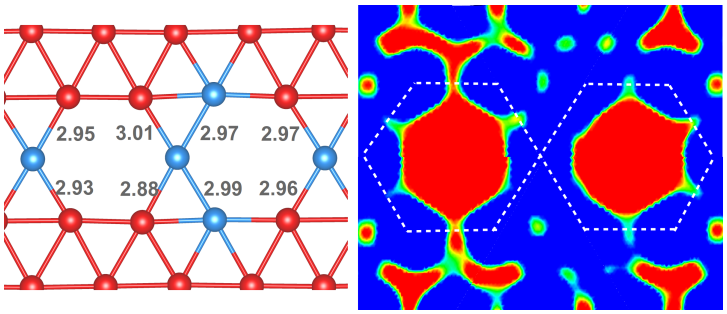

Figure 3.13: Same as Fig. 3.12 for $Fe_{0.906}O$ with structure C1.

the CD in the same range as before, and we see that in the central region where the two hexagons join, three Fe_B^{3+} are consecutive and the CD accumulation between them is very pronounced. Eventhough these Fe_B^{3+} sites are on a hexagon that shrinks towards the void, their interatomic distances are not particularly reduced (as we would expect given the amount of charge they share). Also, Fe_B^{3+} sites lack of any directionality in their orbital order. In fact, we find only one pair Fe_B^{2+}–Fe_B^{3+} with a reduced CL of 2.88 Å that shows a significant polaronic charge distribution. All the other pairs, regardless of the fact that they hybridize their t_{2g} states, do not seem to accumulate charge along their CL. With this, we can say that the long-range distribution of Fe_B^{3+} in the lattice is crucial for the emergence of polaronic charge sharing, since regions with high concentration of Fe_B^{3+} inhibit this phenomena.

3.4.2 4:1 cluster and Fe_3O_4

The local order generated by the 4:1 clusters in $Fe_{1-x}O$ is a basic building block for the development of a spinel-like structure similar to that of magnetite. Moreover, the local properties around the defects are very similar to those of Fe_3O_4. We will explore here the distribution of charge in the 4:1 cluster, compared to the CD in the $P2/m$ magnetite cell where trimerons emerge (structure S2 from the previous chapter).

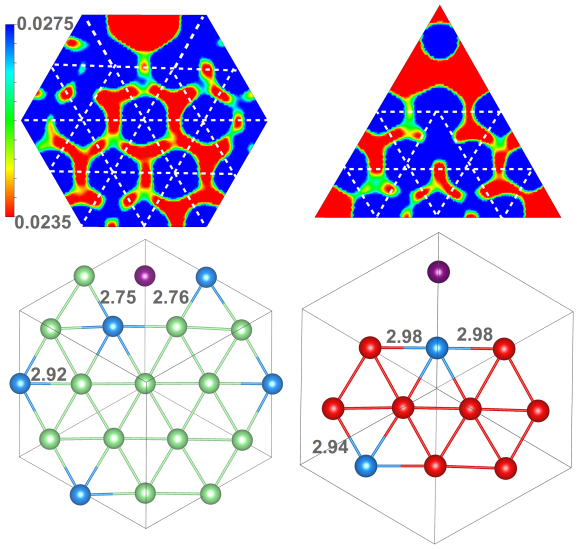

Figure 3.14: Same as Fig. 3.12 for $Fe_{0.906}O$ with 4:1 cluster.

The arrangement of vacancies in the cluster, more explicit in Fig. 3.10, favors the shortening of some of the Fe_B^{2+} – Fe_B^{3+} hybridized pairs, obtaining very reduced values for two of them, as shown in Fig. 3.14, that reach almost

2.75 Å. These two pairs show polaronic charge distribution, while all the other hybridized pairs (whose CL is longer than 2.89 Å) do not. We see as well that the tetrahedral Fe_A favors a distribution where none of the Fe_B^{3+} are n.n. to each other, different from the case already seen with isolated V_{Fe}, where polaronic charge distribution was inhibited by a distribution of close Fe_B^{3+}.

Now the CD range in the interstitial regions is shifted to slightly higher values compared to the isolated vacancies case, and matches better the range of values for magnetite, as can be seen comparing to Fig. 2.12 from the previous chapter.

Since the distribution of Fe_B^{3+} sites is ultimately dictated by the O positions, there is a clear correlation between the emergence of polaronic charge sharing and the structure of the O fcc sublattice. Also, the influence of the Fe_A sites in the distribution of the V_{Fe} has an important role to optimize the conditions for enhanced charge sharing. These conditions are also present in magnetite: a distorted O sublattice and Fe atoms in tetrahedral positions. Additionally, in magnetite there is more freedom to create polarons along any direction due to the ferromagnetism of the Fe_B sublattice.

3.5 Conclusions

When a vacancy is created in stoichiometric FeO, the resulting charge uncompensation leads to the emergence of two Fe_B^{3+} at n.n. positions to the vacancy site, which, compared to the Fe_B^{2+} atoms, are characterized by shorter Fe−O bond lengths; they are also responsible for the closing of the insulating gap from 2 eV to below 1 eV. At the same time, the creation of a V_{Fe} uncompensates the antiferromagnetic ordering, and eventhough the emergent Fe_B^{3+} atoms have enhanced magnetic moments that tend to reduce this imbalance, there is a net magnetization in the lattice. The Fe sublattice tends to fill the voids created by the V_{Fe}, resulting in the contraction of the cell volume and the reduction of the rhombohedral distortion of FeO. If the number of vacancies is increased, regardless of their distribution, all alterations of the structural, electronic, and magnetic properties are localized around the defects. In fact, the features of the stoichiometric oxide tend to be recovered far from the V_{Fe} sites.

We obtain that the formation of compact defect clusters is clearly favored, probably linked to a more effective compensation of the global charge. Nevertheless, the fast quenching process applied to obtain $Fe_{1-x}O$ at ambient conditions may produce samples where different vacancy configurations exist. The most relevant features introduced by the 4:1 clusters are a high degree of overall order due to the localization of the defects, a larger local magnetization, and the existence of more favorable conditions to form polarons.

In analogy to Fe_3O_4, the emergence of polaronic charge sharing is linked to the anomalous shortening of certain interatomic $Fe_B^{2+}-Fe_B^{3+}$ distances below a threshold value of 2.89 Å. The formation of polarons is conditioned by the distribution of the V_{Fe} and the Fe_B^{3+} sites, which in turn depends on the internal structure of the O sublattice

Together with the reduction of the magnetically induced rhombohedral distortion, the limited effect in the energy balance of local alterations of the magnetization around the defects evidences a secondary role of the magnetism in the stability of the system. However, the O sublattice distortion requires the presence of magnetism, even when V_{Fe} are introduced. This distortion plays a crucial role in the emergence of polaronic charge distributions, which are favored under the most stable defect configurations. The importance of the magnetic interactions is higher when tetrahedral Fe_A sites are occupied, making plausible that the magnetic energy balance becomes crucial to determine the stability of large defect structures based on spinel-like clusters.

Chapter 4

Ultrathin magnetite films

As mentioned in the Introduction, different causes may contribute to alter the perfect bulk-like behavior in thin films, such as the emergence of antiphase domain boundaries - APBs[94], or the interaction with the substrate (bond reorganization, imposed strains, changes in internal magnetic and electric fields, and interdiffusion[95, 96, 97]).

In this chapter, we will explore two main effects also present in thin films: the reduction of thickness and the influence of the surface. To this end, we have calculated films on a Au substrate that minimizes the interactions with the interface. We have considered slabs free of APBs, where most bulk-like properties are know to be recovered[98, 99].

We will focus on $Fe_3O_4(001)$ films. Magnetite is most commonly grown along the [001] and the [111] direction, and since our aim is to study the influence of the thickness on the film properties, the repetition unit along the [001] direction is smaller than along the [111], which esaes the modelation of smaller slabs. On the other hand, it is on the $Fe_3O_4(001)$ that the Verwey transtition has been proposed[100], and films along this direction seem to have one stable termination, unlike the (111) surfaces, which are more difficult to stabilize.

We have divided the chapter in three main sections. In the first one, we try to isolate the influence of thickness for the development of magnetite properties, studying ultrathin slabs embedded in several Au layers, gradually increasing the thickness of the Fe_3O_4 structure. In the second section, for a slab bigger than the minimum $P2/m$ cell, different surface reconstructions are explored, showing the influence that these reconstructions exert on the development of short- and long-range orders. Finally, in the third section we investigate the additional effects of the thickness reduction on ultrathin films, creating surfaces in the slabs studied in the first section.

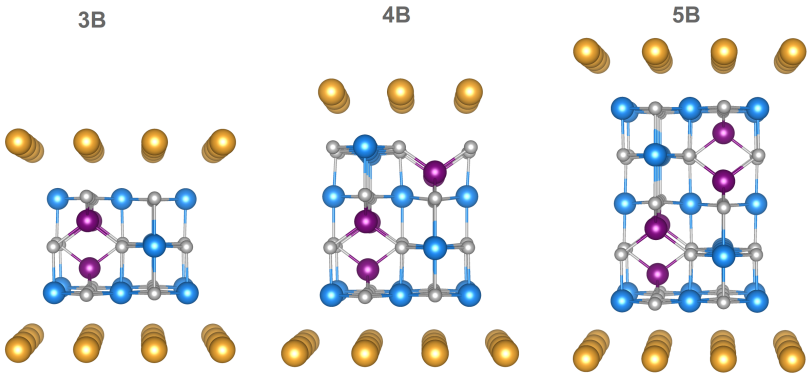

Figure 4.1: Supercells used to model the ultrathin $Fe_3O_4(001)$ films of different thicknesses in our calculations. The Au layers surround the slabs, so that the upper and lower Fe_B-O planes are interface layers in contact with Au.

4.1 Influence of thickness on magnetite properties

In this section we will explore the existence of a fundamental limit for the development of magnetite main electronic features, including the VT. Based on our results for the bulk $P2/m$ cell in Chapter 2, we have performed calculations based on ultrathin $Fe_3O_4(001)$ films in the thickness range below the minimum unit cell size, as shown in Fig. 4.1.

In order to isolate thickness effects avoiding surface reconstructions, we will consider films embedded in a stretched Au(001) matrix three to four layers wide; this minimizes the interactions with the interfaces. The Au substrate has been chosen during the search for a non-interacting medium, after comparison with other metals, always imposing magnetite lattice parameter. We have restricted to terminations on Fe_B-O planes, since experimental evidence indicates that this layer tends to be preferred over the Fe_A-ended case[100]. We have kept fixed the bulk lattice vectors, departing both from the high temperature (HTP) and the low temperature phases (LTP - structure S2 in Chapter 2), and allowing full relaxation of the atomic positions inside the film while leaving fixed the interfaces with Au. This configuration allows to identify differences between both bulk phases at conditions of reduced dimensionality, and to compare their relative stability. The thinnest slab considered (labelled **3B**) contains three mixed Fe_B-O planes and two Fe_A layers, resulting in a thickness of approximately 0.4 nm. This is the minimum thickness required to have at least one Fe_B-O plane free of interface effects. At the subsequent slabs we have gradually expanded the thickness by adding one formula unit (f.u.), that is, one Fe_B-O and one Fe_A additional layers, up to a maximum thickness of ~ 1 nm (slab **6B** (not shown) with 6 Fe_B-O planes), where the bulk features typical of the $P2/m$ unit cell of the LTP are recovered.

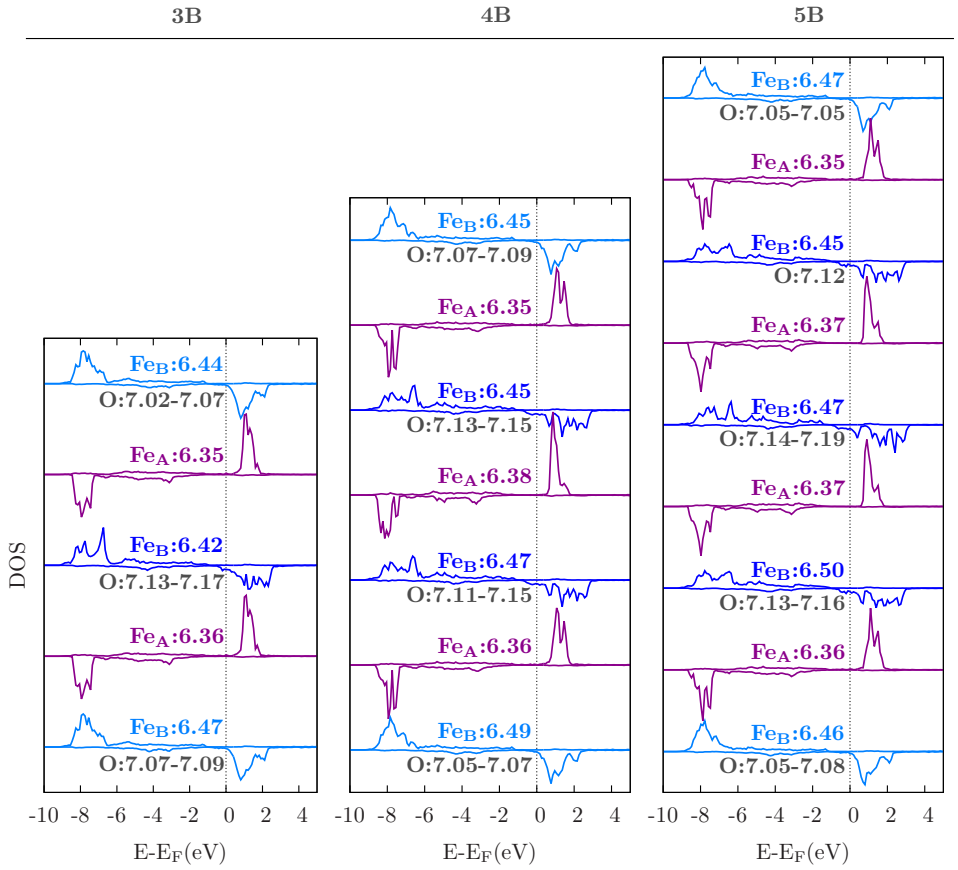

Figure 4.2: Layer- and spin-resolved DOS of all inequivalent Fe atoms for the slabs of Fig. 4.1, as obtained departing from the bulk HTP unit cell. Positive (negative) DOS correspond to majority (minority) spin projections. The corresponding Q_B are indicated, together with the range of Q_B values of O at each layer.

We will first focus on the thinnest 3B films. The layer resolved DOS and Bader charges for the HTP- and LTP-based films are shown in the left panels of Figs. 4.2 and 4.3, respectively. Eventhough slight differences are found in the oxygens Q_B, where the large dispersion of values is partially induced by the different bonds at the interface sites, the final electronic structures are very similar, regardless of the initial unit cell. In the HTP thin film there is a tendency to half-metallicity in the inner Fe_B layer, but the limited thickness does not allow for the complete emergence of it. At the same time, the LTP thin film is not thick enough for the appearance of any charge disproportionation at the Fe_B sublattice. All Fe_B behave closer to a Fe^{3+} valence state than to Fe^{2+}, with the corresponding enhancement of their individual magnetic moments (around $4.1\mu_B$): this leads to a slight increase of the net magnetization of the slab. Nevertheless, both the bulk electronic

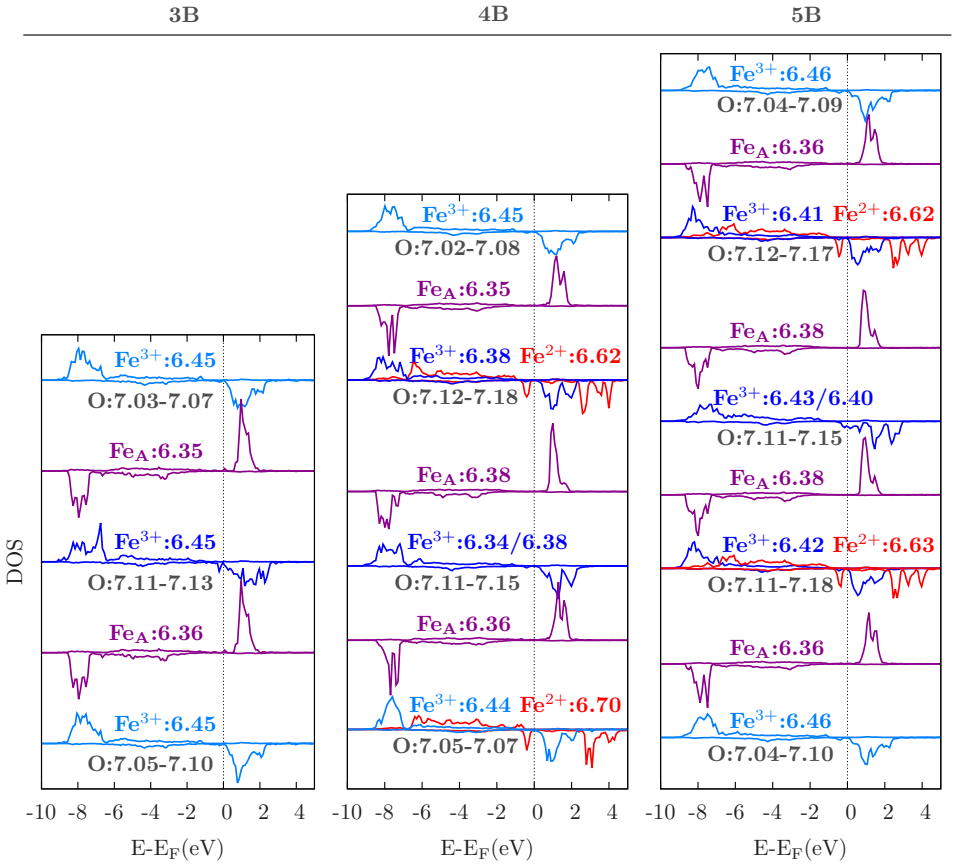

Figure 4.3: Same as Fig. 4.2 departing from the LTP unit cell

properties of the Fe_A atoms and the ferrimagnetic coupling between the Fe sublattices are preserved.

From the structural point of view, differences between the bulk cells of departure are still present in the films. In particular, the network of long and short Fe_B-Fe_B distances enabling the formation of trimerons in the LTP persists at **3B** films of Fig. 4.3, but it does not affect the electronic distribution of charge. These results put an unequivocal thickness limit for the emergence of the VT, and also for the development of charge fluctuations.

As the films grow, we can identify some common features to all slabs. The most important one is the relevant influence of the interfaces. The choice of a supporting Au matrix has been done in order to minimize the interface effects. Nevertheless, the reduced charge transfer from Au lowers the Q_B at the O atoms, and in order to compensate the anionic charge loss, Fe−O distances are reduced. Consequently, the interface Fe_B atoms behave as Fe^{3+}, with an average $Q_B \sim 6.47$, and with increased magnetic moments close to 4.10 μ_B. As we can see in the right axis of Fig. 4.4, where

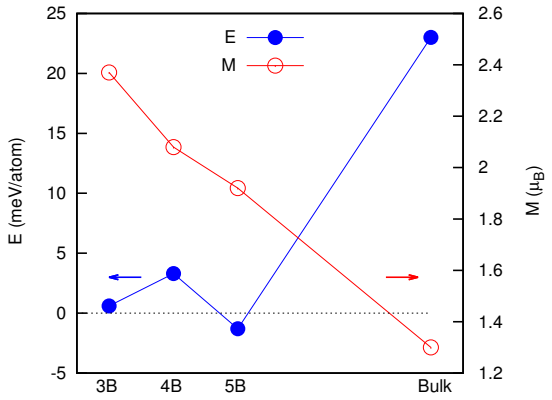

Figure 4.4: Evolution with increasing thickness of the energy difference between slabs constructed from the HTP and LTP unit cells shown in Figs. 4.2 and 4.3 (E, in meV/atom) and of the net magnetization per Fe atom corresponding to the most stable solution (M, in μ_B). As a reference, bulk values are also indicated. The dotted line is a visual guide to the energy zero, positive E values corresponding to stability of the LTP.

we have plotted the normalized net magnetization per Fe atom in the most stable slabs, interface effects are dominant at the thinnest slabs and the net magnetization is enhanced in them. In all cases, the ferrimagnetic bulk-like order prevails with a large energy gain over other solutions, for example, the ferromagnetic one. The bulk-like magnetization is gradually recovered as the thickness increases and the inner layers approach the bulk situation.

For HTP films thicker than **3B**, important differences are evidenced in Fig. 4.2: a tendency to approach half-metallicity is obtained already at **4B**, whose thickness is around 0.65 nm. Compared to the bulk, interatomic distances show larger dispersions in the films, influenced by the structural constraints imposed by the interfaces. The main consequence on the electronic properties is the enhanced charge transfer from Fe_B to O at the inner layers.

On the other hand, at the LTP films in Fig. 4.3, charge disproportionation emerges at the Fe_B sublattice, substantially different from the bulk CO: the electronic constraints imposed by the interface Fe^{3+} atoms condition the development of CO at the inner layers. At **4B**, for example, the symmetry favors the development of in-plane CO, which results in coplanar Fe^{3+} and Fe^{2+} atoms. And though short interatomic distances exist across the slab below the threshold value of 2.89Å, they are not always linked to polaronic charge sharing; they also emerge between Fe^{3+} neighbors. The resulting situation is similar to $Fe_{1-x}O$, where the accumulation of close Fe^{3+} atoms was demonstrated to affect negatively the development of polarons[101] (Chapter 3). In our case, polarons can be found at sparse Fe^{2+}–Fe^{3+} pairs but

linear chains involving three adjacent neighbors are not formed.

The **5B** slabs are even more complex, as the increased thickness makes room for the competition between in-plane and normal CO patterns. In fact, alternative solutions to the best minimum in Fig. 4.3 exist, an example is shown in Fig. 4.5. The figure evidences that again, eventhough shortened distances below the threshold value of 2.89 Å exist, they may couple $Fe^{3+}-Fe^{3+}$ pairs, and even when polarons emerge, they refer to isolated $Fe^{2+}-Fe^{3+}$ couples, but not to trimeronic structures. A bulk-like CO with trimerons is recovered only at the **6B** slabs, implying that an additional threshold thickness of 1 nm is required for the development of the short-range correlations characteristic of magnetite. This thickness is closely linked to the minimum size needed to stabilize a long-range CO similar to the bulk.

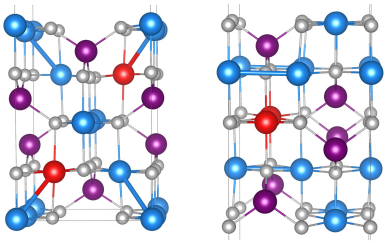

Figure 4.5: Sketch of two almost degenerate solutions found for the **5B** films built from the LTP bulk unit cell. On the left, the case corresponding to Fig. 4.3, and on the right, a situation with an energy difference of less than 1meV/atom. Short interatomic Fe_B-Fe_B distances below 2.89Å are indicated by thick bonds.

Finally, it is interesting to compare the total energies of the HTP- and LTP-slabs ground states. This is done in Fig. 4.4 (left axis), where the relative stability of both types of structures is shown as the film thickness is gradually increased. It is evident that the energy difference between HTP- and LTP-based films is one order of magnitude smaller at the ultrathin limit as compared to the bulk. As expected, essentially no difference is obtained at the thinnest **3B** film, where the electronic properties were already shown to be very similar. But also for thicker films the relative stabilities are comparable, occasionally favoring the half-metallic solution at certain thicknesses. This seems to indicate that penalization of the full development of the bulk CO has important consequences on the stability of magnetite insulating phase, inhibiting the VT.

4.2 Surface effects

The development of devices for novel electronics confers to surfaces a primordial role. One of the most extensively considered aspects in this area is the efficiency of magnetite as a spin injector. The spin polarization of the

injected current is expected to be −100% at room temperature, corresponding to the half-metallic bulk state. However, much lower values are usually attained, and surfaces have been considered responsible of this failure.

In relation to the Verwey transition, the interest on surfaces emerges from the early proposition that short-range correlations should persist above T_V, and that the transition temperature would be higher under reduced dimensions, for example at surfaces[102, 103]. In that sense, the hypothetical existence of a surface VT where surface gap closure occured above T_V was an attractive possibility, and it was proposed for the (001) films[100]. Nevertheless, as we will show, the current evidece questions the existence of a surface transition analog to the VT.

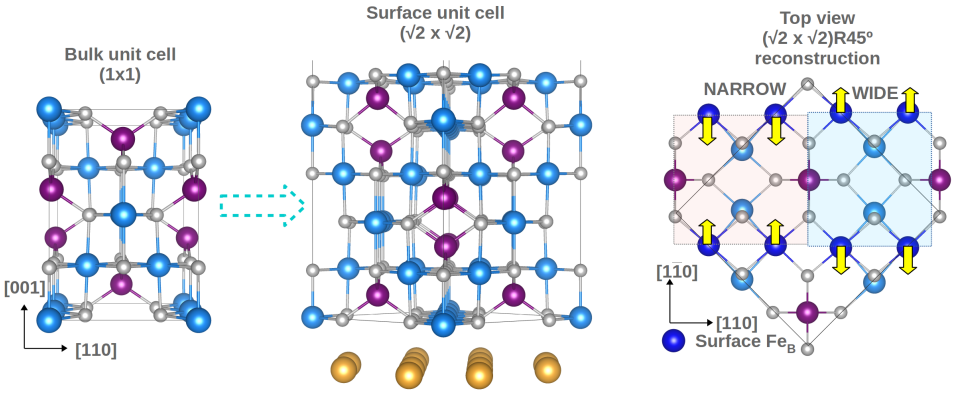

Figure 4.6: $P2/m$ structure (left) and surface slab (center) with 12 layers. Right: $\sqrt{2} \times \sqrt{2}R45°$ reconstruction.

The $Fe_3O_4(001)$ surface presents a $(\sqrt{2} \times \sqrt{2}R45°)$ reconstruction that has been observed under very different preparation conditions, both in thin films and single crystals, and whose origin has been debated for a long time[103, 104, 105, 106]. This reconstruction, which occurs in a Fe_B−O termination[104], consists on a zigzag pattern of Fe_B−Fe_B rows that generates wide and narrow zones as sketched in the right panel of Fig. 4.6. Though here we will restrict to stoichiometric surfaces, it has been recently proposed that the reconstruction is based on an Fe-deficient surface region[107]. It remains apparently unchanged in a wide temperature range, from well above room temperature to below T_V[106, 108], and it persists in films as thin as 2nm, coexisting with APDs[109, 110]. Additionally, the surface presents an insulating gap at room temperature [103], that was initially linked to the existence of a surface Verwey transition[100]. At temperatures around $T_S = 720$ K, recent experiments indicate that the $(\sqrt{2} \times \sqrt{2}R45°)$ pattern disappears through a second-order transition, thus different from the VT[111]. Also, below T_V, the projection on the surface of the structural features of the LTP can be distinguished from the reconstruction [113]. In

order to clarify the ixistence or not of a surface Verwey transition, we have studied the $Fe_3O_4(001)$, including all the range of temperatures mentioned above. We have divided this section into three subsections: above T_S, below T_S, and below T_V, constructing slabs based on the HTP and LTP bulk structures, and with $(\sqrt{2} \times \sqrt{2})$ 2D unit cells, either reconstructed or not, as shown in Fig. 4.6.

4.2.1 Surface above T_S

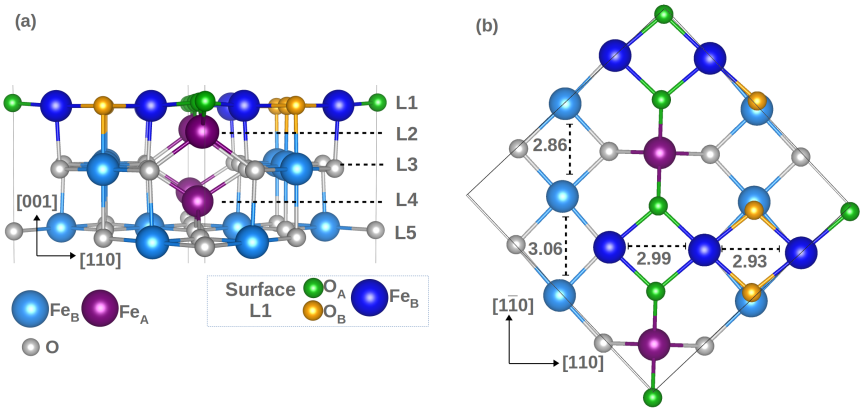

Figure 4.7: (a) Side and (b) top view of the $Fe_3O_4(0\ 0\ 1)$ surface above T_S. Panel (b) only shows the 3 outermost planes, indicating the different in-plane Fe_B−Fe_B distances in Å, omitting the leftmost rows of atoms at L1 for clarity.

We will first focus on the HTP unreconstructed surface above T_S. A sketch of the structure corresponding to our ground state is depicted in Fig. 4.7, where layers are numbered from the surface (L1) towards the bulk. At L1 there are two types of O sites, O_A and O_B, either bonded to a subsurface Fe_A (in green) or on top of a Fe_B (in orange). All the surface oxygens have lost one donor neighbor, and they get closer to their surrounding Fe_B in order to recover their charge. As a consequence of this reduction (Fe_B−O bonds become $\sim$ 1.97 Å), the first interlayer spacing is compressed $d_{12} =$ 0.78 Å (to be compared to the bulk value 1.04 Å), and the subsequent d_{23}=1.17 Å and d_{34}=1.07 Å are expanded. At the same time, the compression of Fe_A−O_A bonds is less prominent, which causes a surface corrugation of 0.12 Å and a slight in-plane wavelike distortion of the O rows. This asymmetry persists at L3, where the O corrugation attenuates to 0.04 Å.

The large distortion of the O sublattice does not affect the Fe_A cations as much as it affects the Fe_B at the two outermost layers L1 and L3. Each Fe_B along the surface [110] and subsurface [1$\bar{1}$0] rows approaches one of its adjacent Fe neighbors, at the expense of moving away from the opposite. As shown in Fig. 4.7(b), where we have removed the leftmost rows of atoms

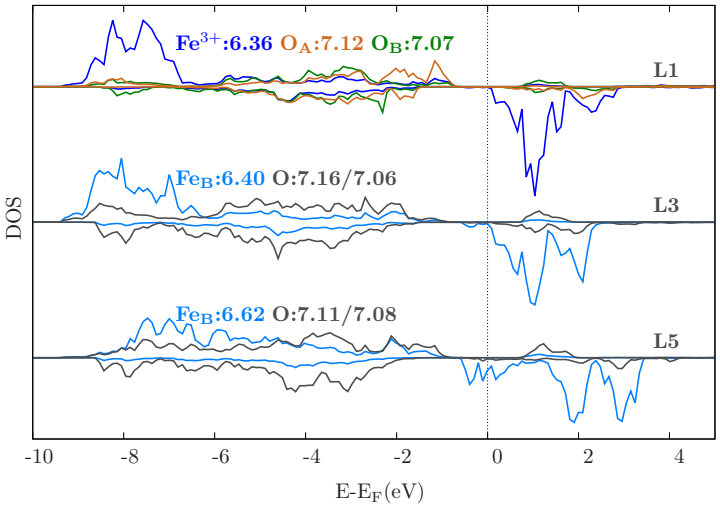

Figure 4.8: Spin-resolved DOS of all inequivalent atoms (blue for Fe, green for surface O) at the outermost Fe_B-O planes from Fig. 4.7, providing the corresponding Q_B.

for clarity, this movement is more pronounced at the subsurface (L3).

In Fig. 4.8 we present the atomic-resolved DOS and corresponding Q_B at the outermost Fe_B-O planes in this structure. Below the surface we obtain a situation similar to the bulk HTP: there is a small dispersion in the Q_B(O) values that is not visible in the DOS. But at the surface, O_A and O_B DOS slightly differ and their charge dispersion is more pronounced. The Fe_B atoms, on the other hand, present several new features at the surface and below it. At L1, all Fe_B behave as Fe^{3+}, opening a surface insulating gap. This is in contrast to the bulk properties below T_V, where the emergence of the gap is not accompanied by any charge disproportionation. Bulk-like behavior is gradually recovered at L3 and is almost restored at L5. Since our slabs are not completely free from confinement effects, we cannot discard that bulk properties could be restablished at L3, as inferred from STM observations of APBs[106, 111].

Regarding the magnetic properties close to the surface, it is important to remark that uncompensated and sligthly enhanced magnetic moments emerge at the top planes ($4.16\mu_B$ for Fe_B and $0.4\mu_B$ for O), and the antiferromagnetic coupling between the Fe_A and Fe_B sublattices remains unaltered. This preserves the bulk-like high magnetic moment of Fe_3O_4 at the high temperature surface.

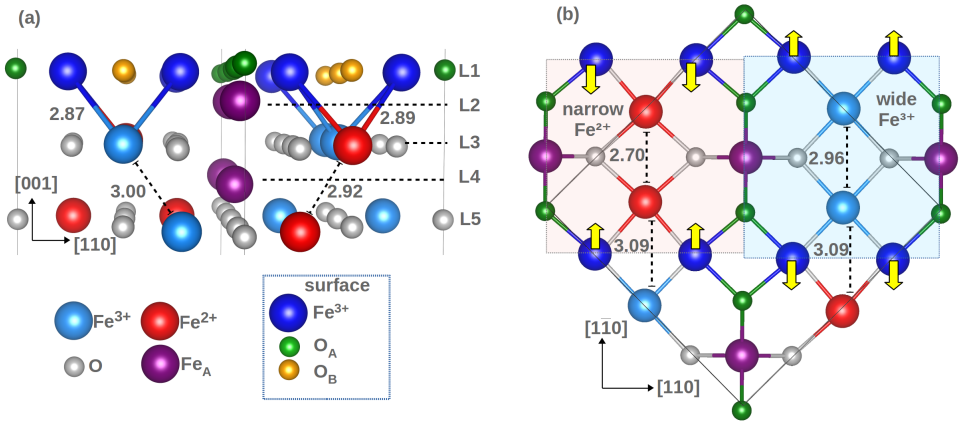

Figure 4.9: (a) Side and (b) top view of the $Fe_3O_4(0\ 0\ 1)$ surface above T_S. Panel (b) only shows the 3 outermost planes, indicating the different in-plane $Fe_B{-}Fe_B$ distances in Å, omitting all the O_B atoms at L1 in (b) for clarity.

4.2.2 Surface below T_S

When the temperature is lowered below T_S, the $(\sqrt{2}\times\sqrt{2}R45°)$ reconstruction sets in. Our results indicate that all structural effects described for the unreconstructed surface are still present below T_S, with only minor interlayer modifications (less than 0.04 Å in d_{23} and d_{34}), and slightly more asymmetric Fe−O coordination units. This is in agreement with previous quantitative low energy electron diffraction (LEED) experiments, where similar oscillatory relaxations of the interlayer distances and large corrugations of the atomic positions were found[108].

Figs. 4.9 and 4.10 show a sketch of the relaxed structure and the corresponding DOS and Q_B at the 3 outermost $Fe_B{-}O$ planes. The zigzag pattern linked to the reconstruction is pointed out in Fig. 4.9(b), where Fe_B-Fe_B distances in the narrow and wide zones differ in ∼0.42 Å. Below these zones, at L3, Fe_B with different valences emerge, Fe^{2+} and Fe^{3+}, setting up a charge disproportionation of $\sim$ 0.10 e on the plane and reducing the dispersion of the O charges. This subsurface CO has already been proposed on the basis of purely electronic effects[100]. However, our results show that in presence of electronic correlations, the wavelike reconstruction is 28 meV/f.u. more stable than the (1×1) surface. We can still see reminiscences of this CO at L5, together with a gradual recovery of the half-metallicity. In fact, we cannot discard some penetration of the surface effects into deeper layers in real samples, since the existence of defects or APBs may contribute to alter the CO, and the energy barrier between different charge distributions is only a few meV[112].

These results support the interplay between CO and electron-lattice couplings (as already proposed in Ref. [111] based on thermodynamic models)

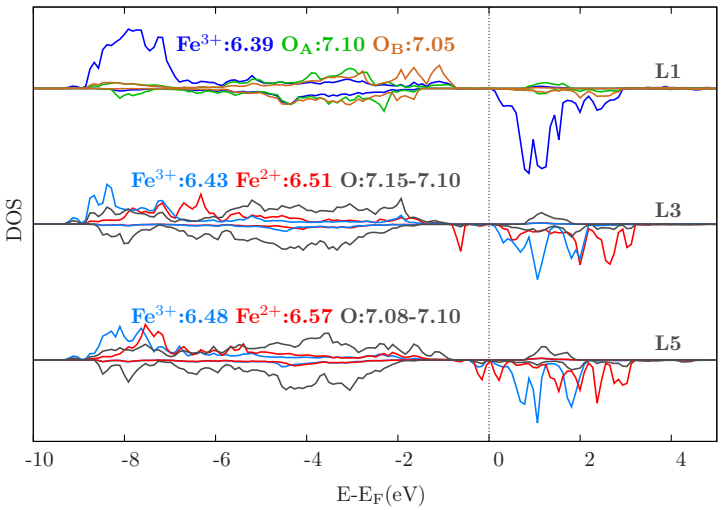

Figure 4.10: Spin-resolved DOS of all inequivalent atoms (blue for Fe, green for surface O) at the outermost Fe_B-O planes from Fig. 4.7, providing the corresponding Q_B.

as the origin of the surface transition. However, the surface insulating character and the emerging CO below T_S are significantly different from the bulk properties at low temperatures. As we will demonstrate, neither the surface structure nor the orbital character of the surface t_{2g} states support the definition of trimerons. In the subsurface, pairs of Fe_B with the same valence emerge beneath the wide and narrow zones highlighted in Fig. 4.9b. These pairs reduce their mutual interatomic distances, inducing a large charge accumulation of $0.037e\text{Å}^{-3}$ between adjacent Fe^{2+}, and 0.029Å^{-3} between Fe^{3+} neighbors.

This configuration inhibits the formation of trimeron chains within the (0 0 1) plane. On the other hand, shortened dimers along the [001] direction are not formed, because every Fe_B on L3 is closer to a pair of Fe_B with the same valence on L5, frustrating the trimeron configuration, as shown in Fig. 4.9.

The above described model for the reconstruction has been revisited very recently[107]. A significant improvement of the LEED R-factor is obtained admitting a non-stoichiometric surface region, with subsurface Fe_B vacancies that are partially compensated by Fe_A interstitials at the L2 plane. Some of the relevant features already described in Figs. 4.9 and 4.10 are still present. First, the undulating surface Fe_B rows, which are more pronounced, make room for the emergence of short-ranged surface charge correlations. Second, the insulating gap rooted in charge compensation effects due to bond reorganization, that questions the existence of a surface Verwey transition analog to that of the bulk. Though the details of the charge distribution inherent to

this model deserve to be determined, the existence of an insulating surface region with distinct features that will alter the periodicity of the bulk CO is common to the stoichiometric surface model adopted by us to describe bare films.

4.2.3 Surface below T_V

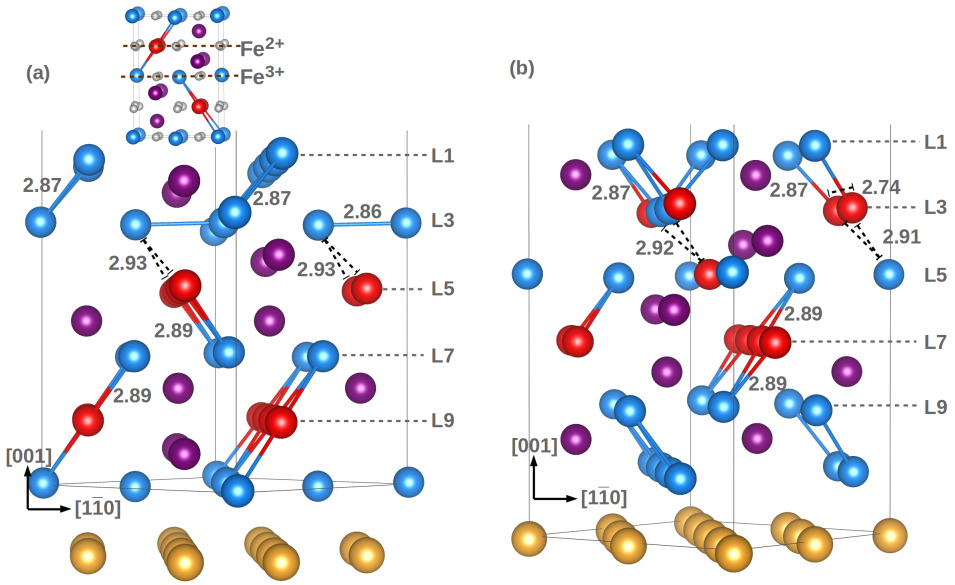

Figure 4.11: Side view of the LTP slabs constructed with (a) the Fe^{2+} or (b) the Fe^{3+} layers exposed. Fe-Fe lines have been drawn for distances below the critical trimeron threshold: 2.90 Å.

The emergence of a distinct CO on the surface layers of magnetite above T_V suggests the possibility of a competition between the LTP bulk CO and the surface CO. In order to explore this, we have modelled the Fe_3O_4(0 0 1) LTP, departing from the bulk unit cell where trimeron chains emerge (structure S2 in Chapter 2). Although this particular cell contains limited information of the actual long-range CO in the bulk, important conclusions can be drawn about the influence that the short-range CO exerts on the surface and viceversa.

There are two types of Fe_B layers in the departing bulk model, which leads to a surface slab that can be constructed exposing either Fe^{2+} or Fe^{3+} planes. As sketched in Fig. 4.11, the ending plane influences the continuity of bulk trimerons close to the surface. For instance, in the case depicted in 4.11(b), CO emerges on L3, opposite to the slab constructed from the Fe^{2+} truncated bulk, represented in Fig. 4.11(a), which is 70 meV/f.u. more stable. This value is around ten times bigger than the energy difference

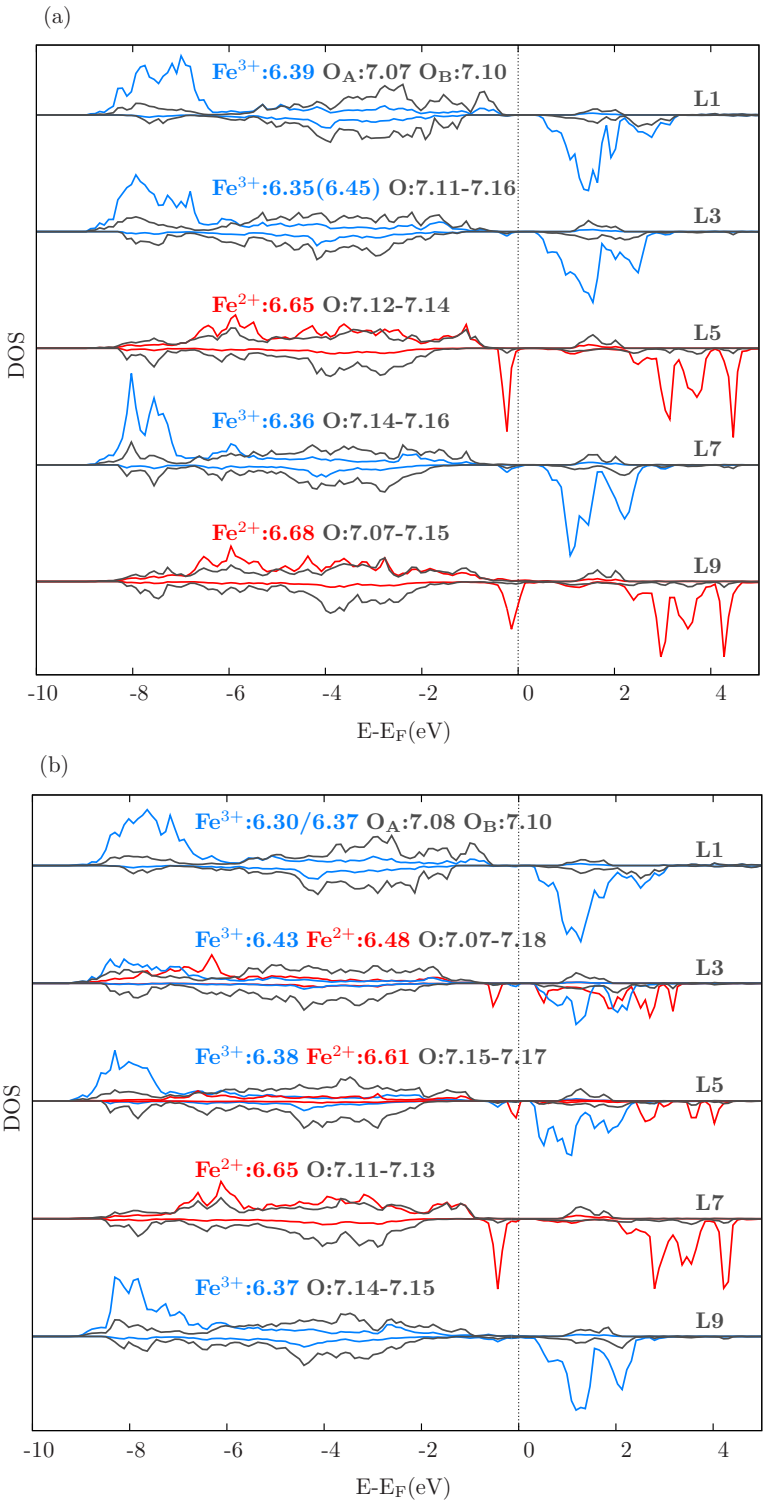

Figure 4.12: Spin-polarized DOS for structures in Fig. 4.11.

between the surfaces above and below T_S, evidencing the high impact of the bulk CO on the surface properties. We have estimated that the loss of the bulk CO at the subsurface lowers the work function by 0.30 eV, a value close to the variation induced by the adsorption of water[114].

On the other hand, the structural and electronic characteristics of the surface region in both slabs are similar to the HTP films: an insulating Fe^{3+} surface layer, shortened in-plane Fe_B-O bonds, a similar pattern of interlayer distances and longitudinal Fe_B displacements. Eventhough the surface causes an additional dispersion of Q_B, as shown in Fig. 4.12(a) and (b), the bulk O charge tends to be recovered.

We have compared the (1×1) and $(\sqrt{2} \times \sqrt{2}R45°)$ symmetries, and surprisingly they have the same electronic structure in both slab terminations, separated by less than 7 meV/f.u.. This difference might come from the additional charge modulation introduced by the LTP bulk structure within the (0 0 1) plane, which obscures the changes introduced by the reconstruction. Regarding Fig. 4.11(a), half of the Fe^{3+} sites at L3 would develop "dimers" with the surface Fe_B, but those have changed their valence inhibiting the polaronic charge distribution. The other half of Fe^{3+} tends to form trimerons with L5, but their distance is slightly bigger than the threshold. Thus, two types of Fe_B sites exist at the subsurface, with similar DOS but slightly different Q_B, which proves again the influence of the bulk CO on the surface properties below T_V.

The insulating surface layer that we always obtain seems to be a universal feature in magnetite even under metastable terminations[115, 116]. This Fe^{3+} layer has an important local effect on the bulk CO, as we can see in Figs. 4.11(b) and its corresponding DOS, where the lack of continuity of the trimerons at the subsurface allows for the emergence of in-plane localized bipolarons, indicating the possible coexistence of local surface and bulk COs. On the other hand, Fig. 4.11(a) evidences that also in the most stable structure those trimerons closer to the surface are slightly affected by it: the $Fe^{3+}-Fe^{2+}$ distances between L3 and L5 are moderately enlarged, which introduces an asymmetry in the Fe chain weakening the charge sharing in its upper branch.

4.3 Influence of thickness reduction

In the last part of this chapter we will investigate the additional effects generated by the surface on the electronic properties of ultrathin films. Since the competition between bulk and surface COs is based on the cooperative effect of the inner bulk layers, new scenarios may exist for thicknesses below the minimum unit cell size. We will focus on films grown along the (001) orientation, which eases the identification of surface effects by comparison to the previous section.

We have considered the same slabs of Fig. 4.1, introducing a vacuum region of more than 12 Å between the Au matrix and one of the film surfaces, and leaving one Au layer in the substrate. Again, we have modelled supercells constructed from both the bulk HTP and LTP unit cells, allowing the relaxation of the three outermost surface layers. The presence of the vacuum implies an additional freedom to relax along the normal to the surface, that particularly at the thinnest films softens the constraints imposed by the fixing of the lattice vectors. We have started in all cases both from an unreconstructed termination and from the $\sqrt{2} \times \sqrt{2}R45°$ surface.

Fig. 4.13 shows the electronic properties of the most stable solutions for the HTP- (top row) and the LTP-films (bottom row). All the **3B** films, as in the embedded cases, converge to similar electronic ground states. The subtle structural differences tend to favor situations that maximize the O charge compensation and subsequently the net magnetization. The large charge demand of the O atoms at the boundaries affects all the planes, causing all Fe_B atoms to act as Fe^{3+}. This dominant effect inhibits the development of any CO induced by the surface reconstruction, which is destabilized. Again, an additional consequence is the lack of a VT in this ultrathin limit.

Despite that singularity, surface features are similar to those described before: the surface O atoms reduce their Q_B and the charge transfer from adjacent Fe neighbors is significantly increased. This reverts in the pronounced decrease of the Q_B at the surface Fe sites that extends with gradual attenuation up to 3 layers in depth. These surface effects on the charge distribution are independent of the film thickness or the surface symmetry, and coincide with those observed at the surfaces of crystals and thick films, pointing to the universality of the local surface properties. A similar conclusion can be obtained regarding local interface effects, that is precisely the interplay of surface and interface features, which extend beyond the planes at the borders, and introduce differences between films of different thicknesses.

The structural reorganization imposed by the large charge demand from surface O is present almost unaltered at all thicknesses. Namely, similar to the effect described in the previous section, the alternance between short and long $d(Fe_B{-}Fe_B)$ along the surface and subsurface rows persists, together with the oscillatory variation of the interlayer spacings imposed by the O−Fe bonds shortening on the surface. The main differences come from the relative stability of the $(\sqrt{2}\times\sqrt{2}R45°)$ and (1×1) surface symmetries. Each surface is strongly affected by the competition between surface- and a bulk-like CO. This can be seen in Fig. 4.14, which shows the corresponding Fe^{2+} and Fe^{3+} distribution, together with the interatomic $Fe_B{-}Fe_B$ distances shortened below 2.90Å. At the LTP, the existence of the reconstruction does not always trigger a subsurface polaronic charge distribution. This occurs because the tendency to develop a bulk-like CO along the (001) direction is dominant, and for these limited thicknesses the reconstruction is not favored. Eventhough there are shortened $d(Fe_B{-}Fe_B)$ throughout the slabs, they do

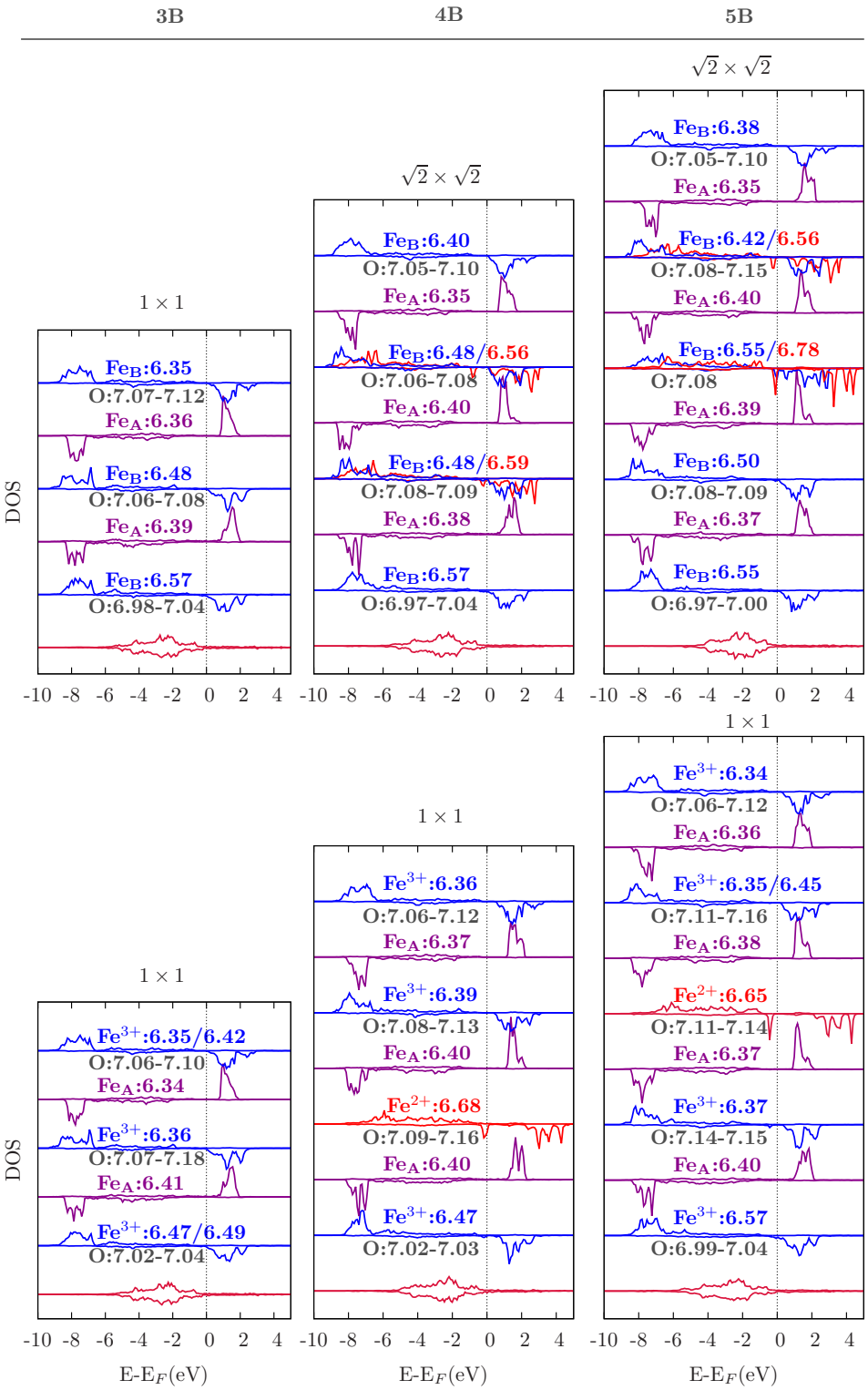

Figure 4.13: Layer and spin-resolved DOS of all different Fe sites at the most stable solutions for the bare HTP-(upper row) and LTP-films (bottom row) of different thickness, distributed as in Fig. 4.14. The corresponding surface symmetry, either (1×1) or $(\sqrt{2}\times\sqrt{2}R45°)$, is indicated for each case. The Q_B of all distinct Fe sites and the range of values for O at each layer are also provided.

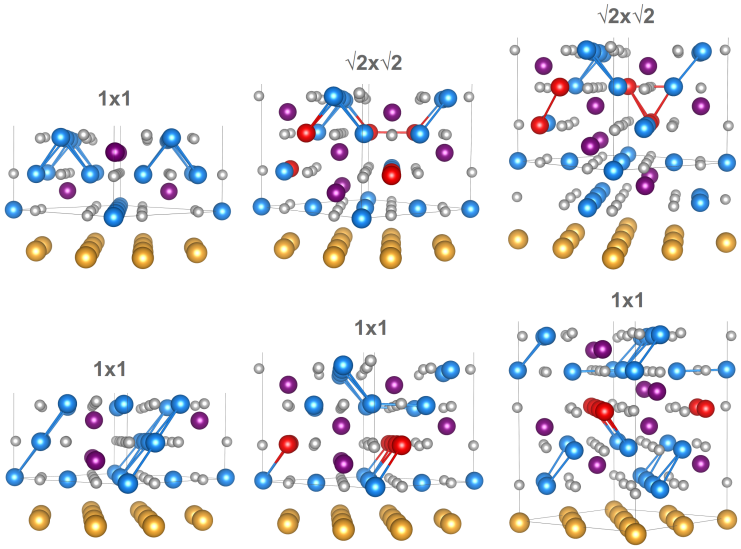

Figure 4.14: Distribution of CO and shortened interatomic distances at the films shown in Fig. 4.13. The yellow bottom layer corresponds to the interface Au plane, while for the rest of atoms the symbols of Fig. 4.9 have been used.

not always link Fe atoms acting with different valence, neither linear chains of Fe^{3+}–Fe^{2+}–Fe^{3+} atoms are formed.

As a result, the tendency to approach the bulk situation as the thickness grows is slower in ultrathin films than in embedded films. This is better evidenced in Fig. 4.15, which shows the evolution of the energy differences between HTP- and LTP-based films (blue line, left axis) along with the net magnetization per Fe atom (red line, right axis) at the most stable solution for each thickness. Regarding the magnetization, the gradual approach to the bulk properties is very similar to the embedded slabs (see Fig. 4.4) The slight enhancement at bare films arises from the enhanced valence of the surface Fe_B atoms. More significant variations are found on the relative stability of HTP- and LTP-based structures: the energy differences are more pronounced and the stabilization of the LTP is less favored. In our slabs, about half of the layers can be considered surface layers, particularly at the thinnest ones, and this is the reason why the settlement of bulk conditions is attenuated. Additionally, the competing emergence of bulk-like and surface COs strongly affects the stability of the LTP, depending on the odd or even number of Fe layers.

Finally, Fig. 4.15 also shows the energy differences between the (1×1) and reconstructed surfaces for each type of bulk unit cell (HTP or LTP, green and magenta lines) Both lines show a gradual tendency to favor the $(\sqrt{2} \times \sqrt{2}R45°)$ surface as the film thickens. While at HTP cells the reconstruction is stabilized except at the **3B** case, at the LTP the competing

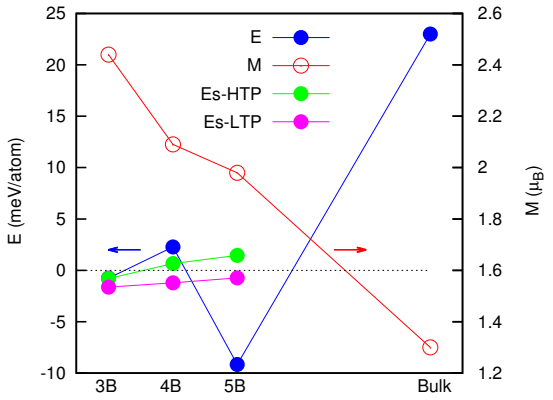

Figure 4.15: Same as Fig. 4.4 for the bare films, also showing the energy gain introduced by the reconstruction (Es) for both the HTP and LTP as a function of the thickness. Positive energies indicate stability of the LTP structure (E) and the $(\sqrt{2} \times \sqrt{2}R45°)$ reconstruction (Es).

COs always lead to a (1×1) surface, but the energy gain with respect to the reconstruction reduces as the thickness increases. In conclusion, as compared to the embedded films, the surface imposes an insulating region with specific structural features and a tendency to develop local CO distinct from the bulk. This introduces a competition between surface and bulk COs that increases the minimum thickness to develop a bulk-like inner structure, and also conditions the emergence of the Verwey transition.

4.4 Conclusions

The reduction of dimensionality in magnetite offers an interesting scenario to explore the coexistence of short- and long-range COs, and their role in the development of electronic phase transitions.

In all slabs studied, there is a robust insulating surface state with Fe^{3+} character, that persists across the surface and bulk phase transitions. It is originated by the large demand of charge from surface O arising from bond breaking, and causes a significant restructuration at the outermost planes that inhibits the formation of trimerons. The competitition of surface and bulk charge distributions at the ultrathin limit slows the recovery of bulk-like properties with increasing thickness. Our results also show that a minimum thickness of 4 $Fe_B{-}O$ planes is required along the [001] axis in order to develop charge order phenomena and a Verwey transition.

Our calculations confirm the higher stability of the surface reconstruction over the (1×1) surface that emerges above T_S, evidencing that both surfaces share common features induced by the charge demand from surface O.

The surface reconstruction below T_S develops a CO that differs from the bulk CO at LTP. Its distinct nature manifests in a lower charge disproportionation as compared to the bulk LTP, and in the preferential bipolaronic CO within (001) planes. The $(\sqrt{2} \times \sqrt{2}R45^\circ)$ reconstruction in thin films is favored as the thickness of the film is increased.

Below T_V, the surface CO competes with the dominant bulk one, and this competition is conditioned by the insulating Fe^{3+} character of the surface, which weakens the trimeron structures close to it. At the same time, the tendency to develop the long-range CO of the LTP alters the stability of the reconstruction, and particularly for ultrathin films, the (1×1) surface may become more stable.

The inclusion of the full Cc symmetry, with additional modulations of the CO within (001) planes, may show an even richer scenario. Similarly, non-stoichiometric surface reconstructions can be considered, extending the thickness of the altered surface region. Nevertheless the robust insulating character Fe^{3+} of the surface and the general idea of surface CO different from the Verwey transition would still remain. Our results unequivocally demonstrate the existence of a mutual influence of the surface and bulk COs, providing and partially quantifying the main features involved in it.

Chapter 5

$Fe_{1-x}O(111)$ Surfaces

The interest on FeO surfaces and thin films is based on two facts: first, ultrathin FeO films have been stabilized at ambient conditions, in contrast to the extreme pressures and temperatures required for the bulk[117]. Second, the first stages of Fe_3O_4 growth on metal substrates (particularly along the (111) orientation) start by the formation of an ultrathin FeO film[117, 118]. However, there are practically no detailed studies of the stability and properties of low dimensional FeO.

In this chapter, we will address the study of FeO(111) surfaces from two different perspectives, with the ultimate aim to understand the evolution of FeO to Fe_3O_4:

- First, we will explore the stability of tetrahedral environments in stoichiometric FeO, by considering würtzite (WZ) structures. WZ stacking defects have already been observed in CoO(111) surfaces[119], and nanosized CoO crystals embedded in ZnO have been stabilized in the search for dilute magnetic materials. In the first section of this chapter, we will consider the WZ form of bulk FeO, followed in the second section by the exploration of the stability and properties of WZ-like terminations, similar to those found for CoO(111).

- Second, we have already shown in previous chapters that formation of 4:1 clusters in $Fe_{1-x}O$ resembles the inverse spinel structure of Fe_3O_4. Furthermore, along the [111] direction, the magnetite lattice can be readily identified with the local environment created by 4:1 clusters, as portrayed in Fig. 2.9. In the last section, we will explore two different terminations of FeO(111) that include Fe-defective planes, corresponding to O-ended and Fe-ended surfaces.

Eventhough self-consistency has been achieved, the results presented in this chapter should be considered as preliminar, since the minima found can correspond to local metastable states. Further work is deserved in this sense, however, this has been taken account in order to extract the conclusions.

5.1 FeO in a würtzite environment. Bulk and Surface.

5.1.1 Bulk WZ FeO

The unit cell of the würtzite-type bulk FeO is depicted in Fig. 5.1. Basically, this structure is built by shifting one of the atoms in the RS cell towards the position on top of the layer below. This way, all the atoms are in a tetrahedral environment and the number of Fe−O bonds for each cation changes from 6 to 4. In the left panel we have sketched an unrelaxed WZ structure with orthogonal lattice vectors. We have calculated the structural and electronic properties, following the same conditions of Chapter 3, and with the same type II antiferromagnetic configuration: adjacent Fe(111) planes are antiferromagnetically coupled. After full relaxation of vectors and atomic positions we obtain the distorted cell sketched in the right panel. The in-plane interatomic distance is measured by $a_{\rm wz} = 3.26 \pm 0.02$ Å, which would correspond, in a rocksalt environement, to an enlarged unit cell parameter of ∼4.6 Å (instead of 4.30 Å). The height of the cell in the [111] direction is $c = 1.65 a_{\rm wz}$, which due to the distortion of the lattice vectors corresponds to interatomic Fe−Fe and O−O distances between atoms in adjacent layers of 3.28±0.09 Å. Finally, the parameter u=0.14 (in relative units, where 1 corresponds to the total height of the cell) determines the existence of two types of Fe−O bond lengths, a long d(Fe−O) = 2.03±0.04 Å, and a short d(Fe−O) = 1.94 Å, as shown in Fig. 5.1. These values are small, compared to the stoichiometric rocksalt FeO (2.15±0.05).

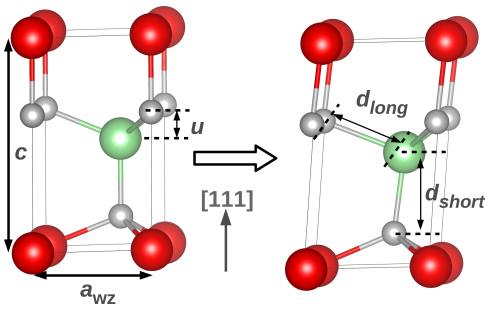

Figure 5.1: Unrelaxed (left) and fully relaxed (right) würtzite-type FeO unit cell. Red and green Fe denote opposite spin directions.

The spin-polarized DOS corresponding to the relaxed structure is plotted in Fig. 5.2, together with the information of the Bader charges and the magnetic moments. The system is insulating, with a smaller gap than the rocksalt bulk, and the Fe (O) charge is slightly enhanced (reduced). This is due to the decrease of the number of bonds in the würtzite geometry.

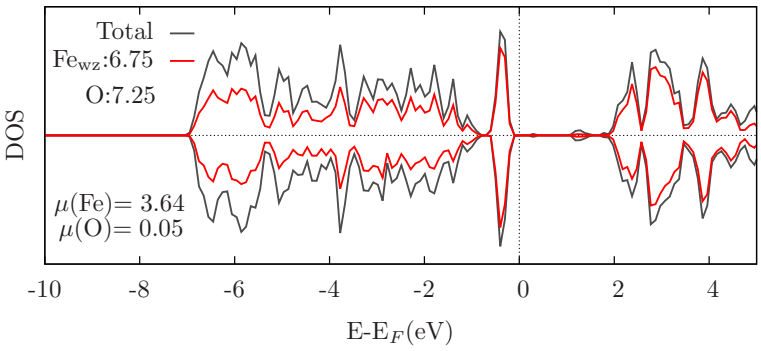

Figure 5.2: Spin-polarized total DOS and Fe contribution, together with the Bader charges of relaxed WZ bulk FeO. The system is an antiferromagnetic insulator with magnetic moments (in μ_B) $\mu(\mathrm{Fe}) = 3.64$ and $\mu(\mathrm{O}) = 0.05$.

However, the enhanced ionicity is accompanied by a slight reduction of the Fe magnetic moment. The structure asymmetry leads to a net O magnetization, but the total magnetization of the cell remains zero. The rocksalt structure is much more stable than the würtzite one. We obtain an energy difference of 190 meV/f.u., which would explain the lack of experimental reports on stable or metastable WZ-type FeO, opposite to CoO.

5.1.2 WZ terminations in RS FeO

As shown for the bulk, a WZ termination can be obtained at the FeO(111) surface by creating a stacking defect, By analogy to the CoO(111) surface[119], we have studied the (1×1) terminations shown in Fig. 5.3, where a WZ termination is obtained by shifting the subsurface atoms to build a local tetrahedral environment in the surface region. Though in CoO this type of surface has been identified only at O terminations due to charge compensation arguments, here we will explore O- and Fe-ended surfaces.

All the slabs are supported on a Ru(0001) substrate layer stretched in order to adapt to the FeO lattice parameter, and a grid in k-space $13\times13\times1$ has been used in all cases. We have considered slabs 12 layers thick in the Fe-ended case, adding one O layer for the O-ended case, having a total of four different structures, as shown in Fig. 5.3. A vacuum region of 16.6 Å is added between opposite slab sides. The choice of Ru is based on the proved ability to grow high quality FeO films on Ru(0001). The first 4 layers in the Fe-ended slabs (5 in the O-ended) are allowed to relax in the [001] direction until the forces are less than 1 meV/Å^3. Regarding the stabilities, we have obtained that the Fe-RS termination is 26 meV/f.u. more stable than Fe-WZ. This difference does not extend to the O-ended slabs, where the RS stacking is less than 3 meV/f.u. more stable than the WZ reconstruction.

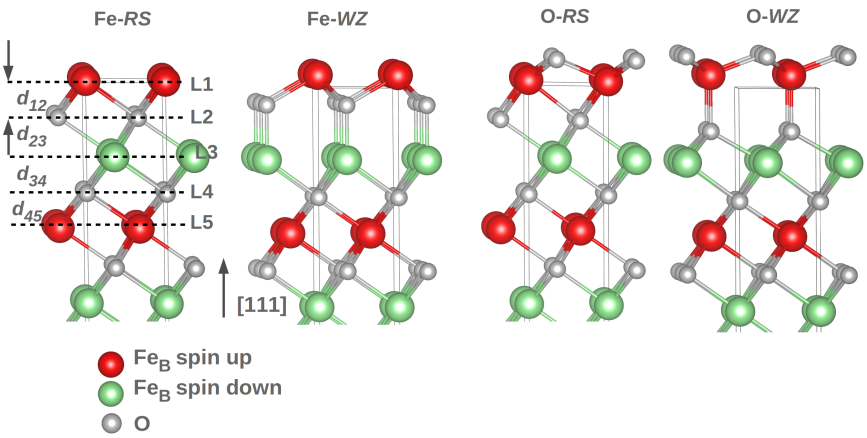

Figure 5.3: Surface terminations considered for (1×1) FeO(111). Red and green Fe layers denote opposite spin directions.

Table 5.1: Interlayer spacings for the surface layers of 1×1 FeO(111) structures sketched in Fig. 5.3

$d_{\text{interlayer}}$(Å)	Fe$-RS$	Fe$-WZ$	O$-RS$	O$-WZ$
d_{12}	1.28	1.00	0.76	0.65
d_{23}	1.24	1.87	1.39	1.88
d_{34}	1.26	1.28	1.23	1.03
d_{45}	1.22	1.25	1.26	1.30
d_{56}	1.24	1.24	1.25	1.23

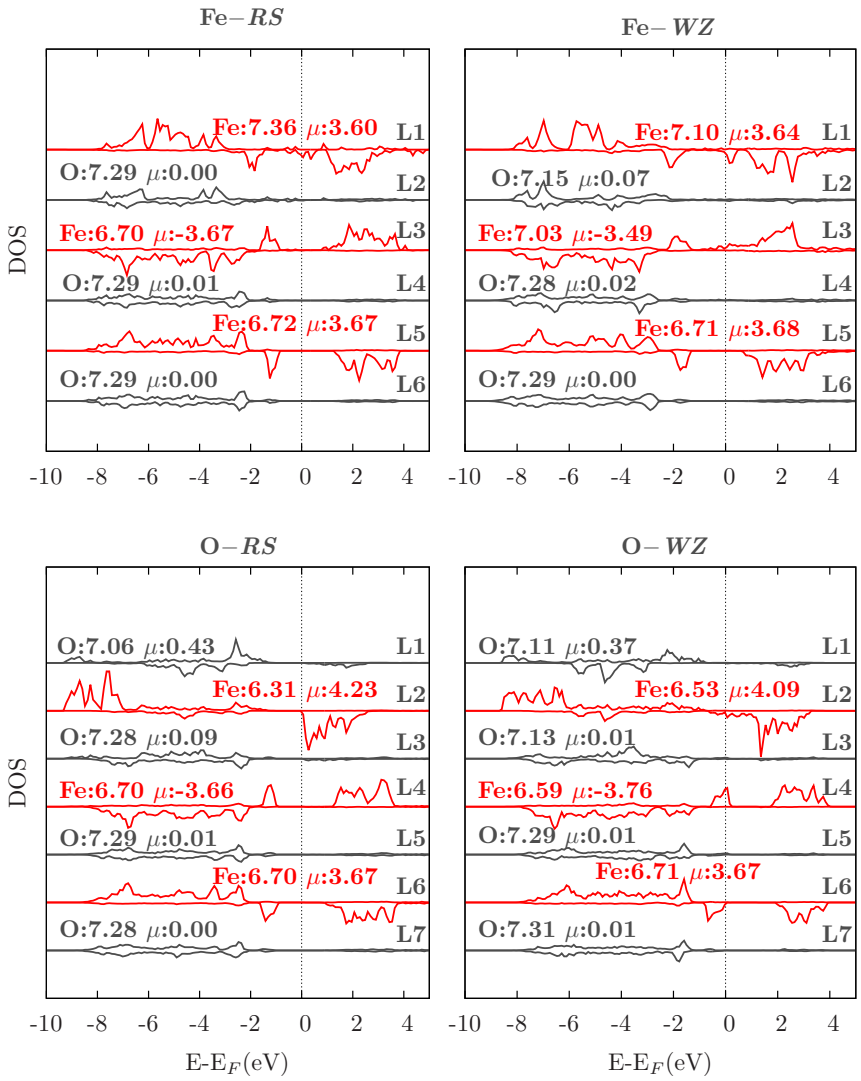

Figure 5.4: Spin-polarized DOS for the surface layers in all slabs if Fig. 5.3, also showing the Q_B.

In Table 5.1 we have summarized the interlayer distances between the first outermost layers of each termination. As a reference, the bulk RS distance is 1.24 Å. In the Fe-RS slab, the surface layer (L1) does not approach L2, opposite to the O-RS case. In these slabs, the largest structural distortions occur at the outermost layers and induce subtle oscillations around the bulk interlayer distance in the subsequent layers. In the WZ cases, d_{12} and d_{23} should be compared with the bulk values 0.75 Å and 1.94 Å, respectively. The structural modulations are more significant than in the corresponding RS cases, and d_{23} behaves in a different manner, with considerable shortening. Also, the changes extend to deeper layers, particularly for O-WZ.

In Fig. 5.4 we have plotted the spin-polarized DOS corresponding to the outermost surface layers of the structures in Fig. 5.3. In general, the bulk FeO behavior is recovered from the third O-layer, which corresponds to L4 in the Fe-ended and L5 in the O-ended structures. In the Fe-ended cases, both slabs experience a tendency to surface metallicity, which in the Fe-WZ case extends to the subsurface Fe-layer (L3), and a considerable increase in their surface charge, which for Fe-WZ reverts in the important decrease of charge of the subsrface. Probably, this inhomogeneous charge redistribution, with loss of O charge, penalizes the stability of this surface. The magnetic moments of the surface Fe are similar to the bulk, and only at the subsurface Fe-layer (L3) of the WZ case there is a significant reduction of μ.

The O-ended slabs show insulating surface layers with a reduced charge in both terminations. Opposite to this, the subsurface Fe-layers show some metallization, though with reduced charge and enhanced magnetic moments, and resembling Fe_B^{3+} atoms emerging at 4:1 clusters of at Fe_3O_4. This manifests in the energy distribution of the states, with accummulation at the bottom of the conduction band. At the O-WZ, surface metallization is extended to L4 and bulk properties are recovered starting from L5. The induced magnetic moment on L1 is significant for both terminations, as the surface O atoms are bonded to Fe atoms with only one orientation of spin. There is also an important increase of the Fe magnetic moments over the bulk values (either RS or WZ), leading to a net surface magnetization that is highest for O-RS.

Summarizing, the (1×1) surface terminations tend to turn metallic and show important distortions of their outermost layers. The WZ environment is evidently less favorable for the Fe-ended slabs, and in the O-ended ones it seems to improve charge compensation, introducing Fe_B^{3+}-like atoms at the subsurface. Also, (1×1) O-ended surfaces introduce a remarkable surface magnetization.

5.2 Fe vacancies in the FeO(111) surface

It is clear that WZ environments are more favorable for O-ended surfaces. This suggests the viability of building tetrahedral structures that lead to the conversion of FeO into Fe_3O_4. To this end, we will explore in this section two different mechanisms. The first one, described in section 5.2.1, is an alternative O-termination that preserves the global FeO stoichiometry, by introducing V_{Fe} locally at a reduced (2×2) symmetry. The second one is the actual introduction of V_{Fe} at Fe-ended surfaces, described in section 5.2.2.

5.2.1 O-ended 2×2 Surface

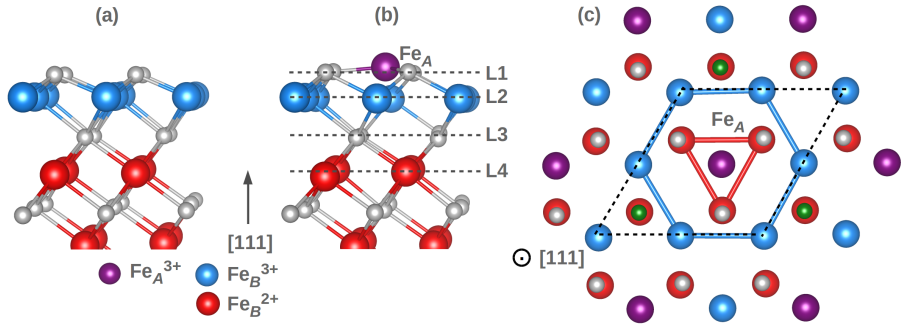

Figure 5.5: Side view of a (2×2) O-ended FeO(111) surface, at the ideal bulk termination (a) and after reconstruction (b). (c) Top view of surface (b), with the 2×2 cell highlighted with dotted lines. Thick Fe−Fe lines are drawn around V_{Fe} on L2 and L4.

When a (2×2) symmetry is considered at the O-ended FeO(111) surface, a reconstruction emerges naturally, consisting on the introduction of a V_{Fe} at the subsurface by shifting one Fe_B to a tetrahedral Fe_A position on top of the surface. This reconstruction is shown in Fig. 5.5, and resembles the non-stoichiometric $(\sqrt{2} \times \sqrt{2}R45°)$ $Fe_3O_4(001)$ termination[107].

In the right panel of the figure, we have sketched the top view of three surface layers, where a blue hexagon coplanar to V_{Fe} surrounds its position, and the red triangle on L4 is beneath the void. The reconstructed surface is 13.4 meV/f.u. (5 meV/atom) more stable than the O-RS surface, and this might explain the difficulties of isolating FeO growth from Fe_3O_4 phases experimentally.

The Fe_A surface atom becomes almost coplanar to the oxygen layer L1, and contrary to the behavior in bulk $Fe_{1-x}O$ (section 3.2), the hexagon highlighted in Fig. 5.5 does not shrink towards the void: the average Fe−Fe distance on the hexagon is of 3.04 ± 0.02 Å. The 3 oxygens bonded to

Fe_A on L1 separate from the void (coloured in grey), and their mutual interatomic distance becomes ~ 3.15 Å. On the other hand, the Fe triangle (on L4) under the void in Fig. 5.5 shrinks on the plane, with a coplanar $d(\mathrm{Fe}-\mathrm{Fe}) = 2.96 \pm 0.01$ Å. Since layer L4 has Fe^{2+} character, the d(Fe−Fe) shortening does not lead to polaronic charge sharing.

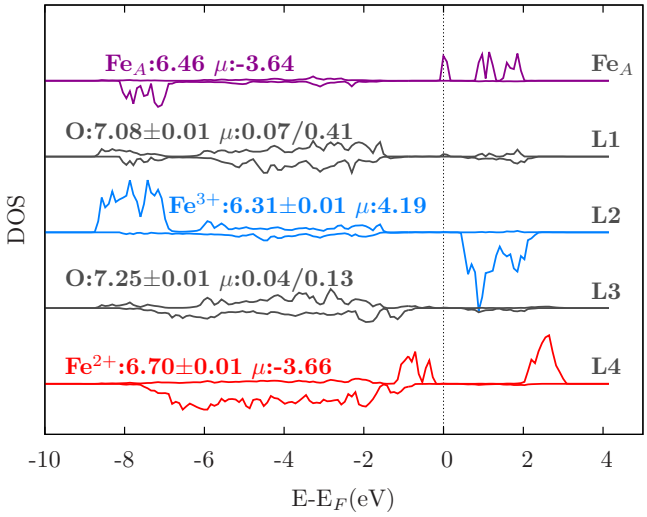

Figure 5.6: FeO(111) DOS, Bader charges and magnetic moments (in μ_B) for the reconstructed O-ended (2×2) surface sketched in Fig. 5.5(b). In the oxygen layers, the bigger value of μ corresponds to the 2n.n. to V_{Fe}.

The spin-polarized DOS is depicted in Fig. 5.6, and shows that Fe_A states contribute at E_F, inducing the slight metallization of the O-L1 atoms n.n. to V_{Fe}. Compared to the DOS corresponding to O-RS 1×1 surface on Fig. 5.4, the layer L2 has a more defined insulating character in the defective structure, and the presence of a vacancy on this layer does not affect the overall DOS below L2, except for the fact that the bulk-like behavior is recovered faster. Bader charges are practically unchanged throughout the slab, as well as the magnetic moments, except for the two outermost layers. The most noticeable inhomogeneitiesin the charge distribution are the increased charge of Fe_A as compared to the (1×1) surface, and the reduced charge of O at L1 due to the loss of bonds. This evidences that the surface vacancy enables a more homogeneous surface region with faster recovery of bulk-like properties at the inner layers, including the reduction of the surface magnetization found for the (1×1) O-ended termination.

5.2.2 Fe vacancies at Fe-ended surfaces.

In this section we study the influence of an isolated vacancy on the Fe-RS surface. To this end, we need to enlarge the unit cell, at the cost of reducing

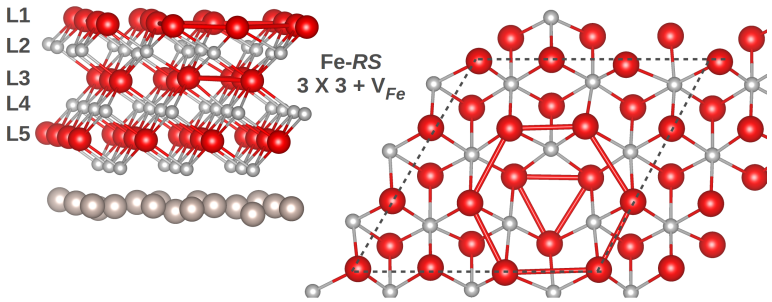

Figure 5.7: (3×3) Fe-ended FeO(111) surface with a V_{Fe} in configuration V1.

the slab thickness. We have considered (3×3) periodicities, that ease the matching to the underlying Ru(0001) substrate lattice without stretching.

The V_{Fe} is created either on the surface layer (case V1) or on the subsurface Fe-layer (V2). In Fig. 5.7 we have sketched the slab used for configuration V1, the slab corresponding to V2 differs only in the position of V_{Fe} (on L3). In the right panel of Fig. 5.7 a Fe hexagon surrounds the surface V_{Fe}. It can be seen from this top view that the size of the supercell is enough for the vacancy to be indeed isolated. A triangle on L3 shows the n.n. to V_{Fe} in the adjacent AFM layer. The first 4 layers are allowed to relax in all directions for both configurations.

We obtain that configuration V1 is 5.5 meV/f.u. more stable than V2. This energy difference is not very large, nevertheless it seems to show that the system prefers the creation of V_{Fe} close to the surface. However, it would be necessary to explore thicker slabs (increasing the computational effort) where the V_{Fe} can be moved into deeper layers and 4:1 clusters can be introduced.

We have studied in Section 3.2 the properties of the bulk $Fe_{1-x}O$ system, in particular the presence of an isolated V_{Fe} in the unit cell. We obtained that the Fe-sublattice tends to close towards the void, while the O-sublattice separates from it. As occured in the O-ended (2×2) surface, the presence of a surface vacancy does not exert the same effect on the sublattice: the Fe-sublattice does not tend to close the surface void; in fact, the hexagon around V_{Fe} is heavily distorted: d(Fe−Fe)=3.1±0.1 Å. In configuration V2, on the other hand, the coplanar hexagon tends to shrink, d(Fe−Fe)=2.98±0.03 Å. Regarding the interlayer distances, and comparing to the first column of Table 5.1, d_{12} is smaller than 1.28 Å in both configurations V1 and V2, but the dispersion of the average value is considerable. Regarding the O-sublattice, oxygens n.n. to V_{Fe} on L2 tend to separate from the void in both configurations, generating a large corrugation of this layer. As it occured in the bulk $Fe_{1-x}O$ case, the bulk values are restored after the second n.n..

One of the consequences of creating a V_{Fe} in FeO, as explained in Chap-

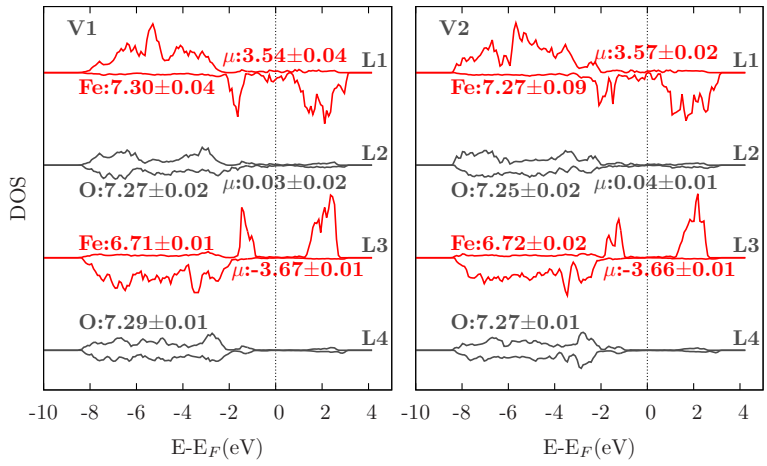

Figure 5.8: (3×3) Fe-ended FeO(111) DOS with a surface V_{Fe} for configurations V1 (left) and V2 (right).

ter 3, is the emergence of two octahedral irons with enhanced valence Fe_B^{3+} per each vacancy created. But at surfaces, the creation of an isolated vacancy does not affect the general electronic properties in the same way. In fact, as the spin-polarized DOS in Fig. 5.8 shows, the electronic properties obtained in the (1×1) slab withouth vacancies are similar to this case, but with a reduction in the Bader charges on layer L1 due to the vacancy. Surface metallization is slightly induced on L2 and disappears completely from L3. It is also remarkable that the creation of V_{Fe} in the subsurface does not lead to the appearance of Fe_B^{3+} atoms. Probably the uncompensated character of the surface does not allow for this effect, as there is already an excess Fe charge at the surface layers. In fact, compared to Fig. 5.4, the Q_B at L1 is slightly reduced here, and in order to obtain Fe_B^{3+} cations it is necessary to create the vacancy at deeper layers. The magnetic moment at L1 is slightly reduced in both configurations, and from L3 on the bulk behavior is restored.

5.3 Conclusions

When bulk FeO is set in a completely tetrahedral environment, the Fe-sublattice tends to stretch, and the Fe-O bonds become shorter in average; also, the Fe charges are slighlty reduced and the opposite occurs to O charges, evidencing an increased ionicity. But globally the structure is not favored, as compared to the rocksalt lattice.

The situation at surfaces is different. The presence of tetrahedrally coordinated Fe atoms is clearly favored at O-ended surfaces, based on charge compensation arguments. The most stable situation seems to be the cre-

ation of (2×2)-reconstructions, introducing V_{Fe} at the subsurface. This enables the preservation of the bulk-like properties at the outermost surface layers, and prevents surface metallization and magnetization.

Similarly, Fe vacancies seem to prefer positions close to the surface, though further work is required to explore this. However, their presence conveys important differences with respect to bulk $Fe_{1-x}O$, both structural (the Fe-sublattice does not tend to fill the void created by V_{Fe} at the surface) and electronic (there is no emergence of additional Fe_B^{3+} sites). In any case, it seems that Fe-ended surfaces involve the emergence of metallicity and the subsequent reduction of the local surface magnetic moments.

Chapter 6

Conclusions

This thesis has been devoted to determine the structural, electronic and magnetic properties of Fe_3O_4 and $Fe_{1-x}O$, both in bulk and low dimensional forms, based on *ab initio* calculations including the influence of correlation effects.

In Chapter 2, we adressed the study of bulk magnetite properties in a reduced $P2/m$ unit cell above and below the Verwey temperature, T_V, with *ab initio* methods. Above T_V, our description of magnetite coincides with previous theoretical and experimental results, we find a half-metallic ferrimagnet with high magnetic moment, where the conduction comes from the octahedral irons Fe_B in the cell. Below T_V, the experimental unit cell has Cc symmetry, but we have shown that in the reduced $P2/m$ cell it is possibile to reproduce most of the low temperature properties, such as the insulating character and the charge ordering.

We have provided the necessary conditions for the emergence of the local short-ranged charge correlation units, the trimerons, from *ab initio* calculations:

- interatomic $Fe_B - Fe_B$ distance shorter than 2.90 Å between irons with different valence,
- orbital directionality of the t_{2g} states of these irons along the direction of the shortened distance, and
- charge accumulation at the middle of this shortened distance, which has to be similar to the charge accumulated between adjacent $Fe^{3+} - Fe^{3+}$ pairs.

We have also discovered that the dominance of a charge order (CO), as the one proposed by Verwey, favors the emergence of trimerons: it minimizes the number of $Fe^{3+} - Fe^{3+}$ pairs, and the appearance of short range correlations is favored when number of adjacent Fe^{3+} is reduced.

In Chapter 3 we have studied bulk $Fe_{1-x}O$ with different concentrations of Fe vacancies (V_{Fe}). We focused on cells with isolated vacancies, and a

clustered structure where vacancies are distributed around a tetrahedral Fe. When a vacancy is created in the stoichiometric FeO, besides the net magnetization of the lattice due to the uncompensated antiferromagnetism, we found that the two Fe_B^{3+} that emerge for charge-compensation are located at n.n. positions to the vacancy site. They present the same properties of the Fe^{3+} at low temperature magnetite, and they are also responsible for the reduction of the insulating gap of stoichiometric FeO. By analizing the distortion of the Fe- and O-sublattices, we found that the void tends to be filled by the Fe-sublattice, while the O-sublattice separates from it. This readjustment results in the contraction of the cell volume and the reduction of the rhombohedral distortion of FeO. When the number of vacancies is increased, regardless of their distribution, all alterations of the structural, electronic, and magnetic properties remain localized around the defects, and the FeO features tend to be recovered far from the vacancies. We obtain that the formation of compact defect clusters is clearly favored, probably linked to a more effective compensation of the global charge. The most relevant features introduced by the 4:1 clusters are a high degree of overall order due to the localization of the defects, a larger local magnetization, and the existence of more favorable conditions to form polarons, in analogy to Fe_3O_4, conditioned by the distribution of vacancies and the Fe_B^{3+} sites, which in turn depends on the internal structure of the O sublattice. We found that local alterations of the magnetization around the defects have a limited effect, which becomes more important when Fe_A sites are occupied. This means that the magnetic energy balance becomes crucial to determine the stability of defect structures based on spinel-like clusters Also, the O sublattice plays a crucial role in the emergence of polaronic charge distributions, and regardless of the presence of Fe vacancies, its distortion requires the presence of magnetism.

In Chapter 4 we have studied the properties of $Fe_3O_4(001)$ in different low dimensional structures.

At first, we have determined the temperature evolution of the (001) surface, both across the Verwey transition (T_V) and the surface transition (T_S), where the $(\sqrt{2}\times\sqrt{2}R45^\circ)$ reconstruction disappears, restricted to stoichiometric configurations. In all cases we found a robust insulating surface state with Fe^{3+} character, due to the demand of charge from surface O, and a significant reorganization at the outermost planes. These features inhibit the local formation of trimerons. The insulating state persists across the surface and bulk phase transitions. We have shown that below T_S the emerging surface CO differs from the bulk CO: it corresponds to a lower charge disproportionation, and eventhough it is accompanied by the formation of polarons, they link only two Fe_B sites and lie within (001) planes, at difference with the trimerons. Below T_V, the surface and bulk COs compete, conditioned by the insulating Fe^{3+} surface layer, that weakens the trimeron structures.

In second place, we have studied the influence of the thickness on the emergence of the distinct properties of magnetite. We have found that there exists a minimum thickness that enables the emergence of half-metallicity and the development of charge disproportionation at the Fe_B sublattice, and that this limit is identical for bare and embedded films. As the thickness is increased, the relative stability of the low- and high-temperature phases is altered. This situation occurs similarly for the (1×1) and $(\sqrt{2} \times \sqrt{2}R45°)$ surface symmetries. This indicates an alteration of the phase diagram of Fe_3O_4 at low dimensions, largely conditioned by the ability to develop CO. On the other hand, the formation of local magnetic moments and the ferrimagnetic bulk-like order are robust also under reduced dimensions. The recovery of bulk properties as the thickness is increased is faster in the absence of bare surfaces, due to the existence of a surface-induced CO that competes with that of the bulk.

In Chapter 5 we have explored the stability of local tetrahedral environments in FeO(111) surfaces. To this end, we have investigated the properties of bulk würtzite FeO. Compared to the rocksalt FeO, the Fe-sublattice tends to stretch, and the Fe-O bonds become shorter in average; also, the Fe charges are slighlty reduced and the opposite occurs to O charges. However, the structure is clearly not favored over the rocksalt one.

At surfaces, the coexistence of rocksalt and würtzite structures depends on the surface termination: Fe-ended films with würtzite structure are very unstable, unlike the case with O-ended films, where the (1×1) bulk truncation and the würztite reconstruction have comparable stabilities. The simple introduction of WZ coordinations at the subsurface involves significant structural distortions that seem to correspond to local metastable minima. When lower symmetries are allowed at O-ended surfaces, we have discovered a surface reconstruction that involves the introduction of subsurface V_{Fe}. This reconstruction mimics the last three layers of the $Fe_3O_4(111)$ surface termination, and we have found that this stoichiometric configuration is more stable than the unreconstructed one. The presence of a surface vacancy accelerates the recovery of the bulk properties at the inner layers and diminishes the influence of the surface (charge redistribution, magnetization, metallicity) at the outermost layers. We have also studied Fe-ended defective surfaces, concluding that it is more profitable for the system to have V_{Fe} at the surface than at the subsurface layers. When the V_{Fe} is on the surface, the distortion does not resemble the bulk $Fe_{1-x}O$, as the presence of the surface compensates the need to create Fe_B^{3+} close to the vacancy site. Though our work seems to indicate that V_{Fe} are prone to distribute close to $Fe_{1-x}O$ surfaces, further work deserves to be done to explore alternative V_{Fe} distributions.

Bibliography

[1] C. Rödl, F. Fuchs, J. Furthmüller, and F. Bechstedt, *Phys. Rev. B* **79**, 235114 (2009). C. H. Brandow, *Adv. Phys.* **26**, 651 (1977).

[2] Ch. Kant, M. Schmidt, Z. Wang, F. Mayr, V. Tsurkan, J. Deisenhofer, and A. Loidl, *Phys. Rev. Lett.* **108**, 177203 (2012); W. Luo, P. Zhang, and M. L. Cohen, *Solid State Commun.* **142**, 504 (2007).

[3] S. M. Tomlinson, C. R. A. Catlow, and J. H. Harding, *J. Phys. Chem. Solids* **51**, No. 6, pp. 407-506 (1990).

[4] R. M. Hazen and R. Jeanloz, *Reviews of Geophysics and Space Physics* **22**, No. 1, pp. 37-46 (1984).

[5] W. L. Roth, *Phys. Rev.* **110**, 1333 (1958).

[6] F. Koch and J. B. Cohen, *Acta Crystallogr. Sect. B* **25**, 275 (1969).

[7] C. R. A. Catlow and B. E. F. Fender, *J. Phys. C* **8**, 3267 (1975).

[8] C. Lebreton and L. W. Hobbs, *Radiation Effects* **74**, 227 (1983).

[9] L. Minervini and R. W. Grimes, *J. Phys. Chem. Solids* **60**, 235 (1999).

[10] B. T. Willis and H. P. Rooksby, *Acta Crystallogr.* **6**, 827 (1953).

[11] H. Fjellvag, F. Gronvold, S. Stolen, and B. Hauback, *J. Solid State Chem.* **124**, 52 (1996).

[12] C. A. McCammon and Lin-gun Liu, *Physics and Chemistry of Minerals* **10**, No. 3, pp 106-113 (1984).

[13] D. V. Dimitrov, K. Unruh, G. C. Hadjipanayis, V. Papaefthymiou, and A. Simopoulos, *J. Appl. Phys.* **87**, 7022 (2000).

[14] D. P. Johnson, *Solid State Commun.* **7**, 1785 (1969).

[15] J. B. Carlson, *Science* **189**, 753 (1975).

[16] A. G. Roca, R. Costo, A. F. Rebolledo, S. Veintemillas-Verdaguer, P. Tartaj, T. Gonzalez-Carreño, M. P. Morales and C. J. Serna *J. Phys. D: Appl. Phys.* **42**, 224002 (2012). T. Indira and P. Lakshmi, *International Journal of Pharmaceutical Sciences and Nanotechnology* **3**, 1035 (2010). P. Majewski and B. Thierry, *Crit. Rev. Solid State Mater. Sci.* **32**, 203 (2013).

[17] Z. Stephen, F. Kievit, and M. Zhang *Mater. Today* **14**, 330 (2011).

[18] M. Darbandi, F. Stromberg, J. Landers, N. Reckers, B. Sanyal, W. Keune, and H. Wende, *J. Phys. D* **45**, 195001 (2012)

[19] F. Salafranca, J. Gazquez, N. Pérez, A. Labarta, S. Pantelides, S. Pennycook, X. Batlle, and M. Varela, *Nano Lett.* **12**, 2499 (2012).

[20] G. Parkinson, U. Diebold, J. Tang, and L. Malkinski, *Tailoring the interface properties of magnetite for spintronics*, Advanced Magnetic Materials (InTech Open).

[21] M. A. Correa-Duarte, M. Grzelczak, V. Salgueiriño-Maceira, M. Giersig, L. M. Liz-Marzán, M. Farle, K. Sierazdki, and R. Diaz, *J. Phys. Chem. B* **109 (41)**, pp 1906019063 (2005).

[22] E. J. W. Verwey *Nature* **144**, 327 (1939).

[23] F. Walz, *J. Phys.: Condens. Matter* **14**, R285 (2002).

[24] M. Iizumi, T. Koetzle, G. Shirane, S. Chikazumi, M. Matsui, and S. Todo, *Acta Crystallogr. B* **38**, 2121 (1982).

[25] H. T. Jeng, G. Guo, and D. Huang, *Phys. Rev. B* **74**, 195115 (2006).

[26] K. Yamauchi, T. Fukushima, and S. Picozzi, *Phys. Rev. B* **79**, 212404 (2009).

[27] M. Senn, J. Wright, and J. Attfield, *Nature* **481**, 173 (2012).

[28] P. Piekarz, K. Parlinski, and A. M. Oleś, *Phys. Rev. Lett.* **97**, 156402 (2006).

[29] P. Piekarz, K. Parlinski, and A. M. Oleś, *Phys. Rev. B* **76**, 165124 (2007).

[30] A. Orozco, S. B. Ogale, Y. H. Li, P. Fournier, Eric Li, H. Asano, V. Smolyaninova, R. L. Greene, R. P. Sharma, R. Ramesh, and T. Venkatesan, *Phys. Rev. Lett.* **83**, 1680 (1999).

[31] H. Wu, O. Mryasov, M. Abid, K. Radican, and I. Shvets, *Sci. Rep.* **3**, 1830 (2013).

[32] S. Lee, A. Fursina, J. Mayo, C. Yavuz, V. Colvin, R. Sofin, I. Shvets, and D. Natelson *Nat. Mater.* **7**, 130 (2008).

[33] A. Fursina, R. Sofin, I. Shvets and D. Natelson, *Phys. Rev. B* **81**, 045123 (2010).

[34] J. Wong, A. Swartz, R. Zheng, W. Han, and K. Kawakami, *Phys. Rev. B* **86**, 060409(R) (2012).

[35] R. J. McQueeney, M. Yethiraj, S. Chang, W. Montfrooij, T. G. Perring, J. M. Honig, and P. Metcalf, *Phys. Rev. Lett.* **99**, 246401 (2007); *Erratum: Phys. Rev. Lett.* **100**, 069901 (2008).

[36] M. Born and J. Oppenheimer, *Ann. Phys. Leipzig* **84**, 457484 (1927).

[37] R. G. Parr, W. Yang, *Density-functional theory of atoms and molecules* (Oxford University Press, New York, 1989).

[38] L. H. Thomas, *Math. Proc. Cambridge* **23**, 542 (1927).

[39] E. Fermi, *Rend. Accard. Naz. Lincei* **6**, 602 (1927).

[40] P. Hohenberg and W. Kohn, *Phys. Rev.* **136**, B864 (1964).

[41] G. Zhang, *Understanding the role of van der Waals forces in solids from first principles* (PhD Thesis, Freie Universität Berlin, 2014).

[42] W. Kohn and L. J. Sham, *Phys. Rev.* **140**, A1133 (1965).

[43] J. P. Perdew, A. Ruzsinszky, J. Tao, V. Staroverov, G. Scuseria, and G. Csonka, *J. Chem. Phys.* **123**, 62201 (2005).

[44] J. P. Perdew and K. Schmid, in *Density Functional Theory and Its Application to Materials*, edited by V. Van Doren (AIP Press, Melville, New York, 2001).

[45] S. H. Vosko, L. Wilk, and M. Nusair, *Can. J. Phys.* **58**, 1200, (1980).

[46] J. P. Perdew and Y. Wang, *Phys. Rev. B* **45**, 13244 (1992).

[47] J. P. Perdew, M. Ernzerhof, and K. Burke, *J. Chem. Phys.* **105**, 9982 (1996).

[48] P. D. Haynes, *Linear-scaling methods in ab-initio quantum-mechanical calculations* (PhD. Thesis, Christ's College, University of Cambridge, July 1998)

[49] J. C. Phillips, *Phys. Rev.* **112**(3), 685 (1958).

[50] J. C. Phillips and L. Kleinman, *Phys. Rev.* **116**(2), 287 (1959).

[51] D. J. Singh and L. Nordstrom *Planewaves, Pseudopotentials, and the LAPW method. Second edition* (Springer, 2006)

[52] P. E. Blöchl, *Phys. Rev. B* **50**, 17953 (1994).

[53] G. Kresse, and J. Joubert, *Phys. Rev. B* **59**, 1758 (1999).

[54] G. Kresse and J. Furthmüller, *Phys. Rev. B* **54**, 11169 (1996).

[55] G. Kresse and J. Hafner, *Phys. Rev. B* **47**, 558 (1993).

[56] J. P. Perdew, A. Ruzsinszky, G. I. Csonka, O. A. Vydrov, G. E. Scuseria, L. A. Constantin, X. Zhou, and K. Burke, *Phys. Rev. Lett.* **100**, 136406 (2008).

[57] V. I. Anisimov, J. Zaanen, and O. K. Andersen, *Phys. Rev. B* **44**, 943 (1991).

[58] K. Terakura, T. Oguchi, A. R. Williams, and J. Kübler, *Phys. Rev. B* **30**, 4734 (1984).

[59] A. Svane and O. Gunnarsson, *Phys. Rev. Lett.* **65**, 1148 (1990).

[60] Z. Szotek, W. M. Temmerman, and H. Winter, *Phys. Rev. B* **47**, 4029(R) (1993).

[61] M. R. Norman, *Phys. Rev. B* **44**, 1364(R) (1991).

[62] S. L. Dudarev, G. A. Botton, S. Y. Savrasov, C. J. Humphreys, and A. P. Sutton, *Phys. Rev. B* **57**, 1505 (1998).

[63] H. J. Monkhorst and J. D. Pack, *Phys. Rev. B* **13**, 5188 (1976).

[64] Richard F. W. Bader, *Atoms in Molecules. A Quantum Theory* (Department of Chemistry, McMaster University, Ontario, Canada, 1994).

[65] W. Tang, E. Sanville, and G. Henkelman, *J. Phys.: Compute Mater.* **21**, 084204 (2009).

[66] E. Sanville, S. D. Kenny, R. Smith, and G. Henkelman, *J. Comp. Chem.* **28**, 899-908 (2007).

[67] G. Henkelman, A. Arnaldsson, and H. Jónsson, *Comput. Mater. Sci.* **36**, 254-360 (2006).

[68] J. Neugebauer and M. Scheffler, *Phys. Rev. B* **46**, 16067 (1992).

[69] D. Ihle and B. Lorenz, *J. Phys. C* **18**, L647 (1985).

[70] D. Ihle, *Z. Phys. B: Condens. Matter* **58**, 91 (1985).

[71] E. Goering, *Phys. Stat. Sol. (b)* **248**, 2345 (2011).

[72] D. Huang, C. Chang, H. T. Jeng, G. Guo, H. J. Lin, W. Wu, H. Ku, A. Fujimori, Y. Takahashi, and C. Chen C, *Phys. Rev. Lett.* **93**, 077204 (2004).

[73] E. de Grave, R. Persoons, R. Vandenberghe, and P. de Bakker, *Phys. Rev. B* **47**, 5881 (1993).

[74] M. Uhl and B. Siberchicot, *J. Phys.: Condens. Matter* **7**, 4227 (1995).

[75] R. McQueeney, M. Yethiraj, S. Chang, W. Montfrooij, T. Perring, J. Honig, and P. Metcalf, *Phys. Rev. Lett.* **99**, 246401 (2007).

[76] Z. Zhang and S. Satpathy, *Phys. Rev. B* **44**, 13319 (1991).

[77] J. G. Tobin, S. A. Morton, S. W. Yu, G. D. Waddill, I. K. Schuller, and S. A. Chambers, *J. Phys.: Condens. Matter* **19**, 315218 (2007).

[78] M. Fonin, Y. S. Dedkov, R. Pentcheva, U. Rüdiger, and G. Güntherodt, *J. Phys.: Condens. Matter* **20**, 142201 (2008).

[79] H. Kobayashi, T. Nagao, M. Itou, S. Todo, B. Barbiellini, P. E. Mijnarends, A. Bansil and N. Sakai, *Phys. Rev. B* **80**, 104423 (2009).

[80] A. Bosak, D. Chernyshov, M. Hoesch, P. Piekarz, M. Le Tacon, M. Krisch, A. Kozlowski, A. M. Oleś, and K. Parlinski, *Phys. Rev. X* **4**, 011040 (2014).

[81] S. de Jong et al. *Nat. Mater.* **12**, 882 (2013).

[82] L. Craco, M. S. Laad, and E. Müller-Hartmann, *Phys. Rev. B* **74**, 064425 (2006).

[83] V. I. Anisimov, J. Zaanen, and O. K. Andersen, *Phys. Rev. B* **44**, 943 (1991).

[84] M. Däne, M. Lüders, A. Ernst, D. Köderitzsch, W. M. Temmerman, Z. Szotek, and W. Hergert, *J. Phys.: Condens. Matter* **21**, 045604 (2009).

[85] P. Thunstrom, I. Di Marco, and O. Eriksson, *Phys. Rev. Lett.* **109**, 186401 (2012).

[86] I. I. Mazin and V. I. Anisimov, *Phys. Rev. B* **55**, 12822 (1997).

[87] N. C. Tombs and H. P. Rooksby, *Nature (London)* **165**, 442 (1950).

[88] G. Fischer, M. Däne, A. Ernst, P. Bruno, M. Lüders, Z. Szotek, W. Temmerman, and W. Hergert, *Phys. Rev. B* **80**, 014408 (2009).

[89] C. G. Van de Walle and J. Neugebauer, *Appl. Phys. Rev.* **95**, 3851 (2004).

[90] K. Reuter and M. Scheffler, *Phys. Rev. B* **65**, 035406 (2001).

[91] C. Freysoldt, B. Grabowski, T. Hickel, J. Neugebauer, and G. Kresse, *Rev. Mod. Phys.* **86**, 253 (2014).

[92] D. V. Dimitrov, K. Unruh, G. C. Hadjipanayis, V. Papaefthymiou, and A. Simopoulos, *Phys. Rev. B* **59**, 14499 (1999).

[93] I. Bernal-Villamil and S. Gallego, *J. Phys.: Condens. Matter* **27**, 012001 (2015).

[94] D. Margulies, F. Parker, M. Rudee, F. Spada, J. Chapman, P. Aitchison and A. Berkowitz, *Phys. Rev. Lett.* **79**, 5162 (1997).

[95] M. Parames, T. Viskadourakis, M. Rogalski, J. Mariano, N. Popovici, J. Giapintzakis and O. Conde, *Appl. Surf. Sci.* **253**, 8201 (2007).

[96] P. Morral, F. Schedin, G. Case, M. Thomas, E. Dudzik, G. van der Laan and G. Thornton, *Phys. Rev. B* **67**, 214408 (2003).

[97] J. Anderson, M. Kuhn, U. Diebold, K. Shaw, P. Stoyanov and D. Lind, *Phys. Rev. B* **56**, 9902 (1997).

[98] Y. Li, W. Han, A. Swartz, K. Pi, J. Wong, S. Mack, D. Awschalom and R. Kawakami, *Phys. Rev. Lett.* **105**, 167203 (2010).

[99] F. Schedin, L. Hewitt, P. Morral, V. Petrov, G. Thornton, S. Case, M. Thomas and V. Uzdin, *Phys. Rev. B* **58**, R11861 (1998).

[100] Z. Łodziana, *Phys. Rev. Lett.* **99**, 206402 (2007).

[101] I. Bernal-Villamil and S. Gallego, *Phys. Rev. B* **90**, 195126 (2014).

[102] P. Anderson, *Phys. Rev.* **102**, 1008 (1956).

[103] I. V. Shvets, G. Mariotto, K. Jordan, N. Berdunov, R. Kantor, and S. Murphy. *Phys. Rev. B* **70**, 155406 (2004).

[104] B. Stanka, W. Hebenstreit, U. Diebold and S. Chambers, *Surf. Sci.* **448**, 49 (2000).

[105] R. Pentcheva, F. Wendler, H. L. Meyerheim, W. Moritz, N. Jedrecy and M. Scheffler, *Phys. Rev. Lett.* **94**, 126101 (2005).

[106] Z. Novotny, N. Mulakaluri, Z. Edes, M. Schmid, R. Pentcheva, U. Diebold and G. S. Parkinson, *Phys. Rev. B* **87**, 195410 (2013).

[107] R. Bliem, E. McDermott, P. Ferstl, M. Setvin, O. Gamba, J. Pavelec, M. Schneider, M. Schmid, U. Diebold, P. Blaha, L. Hammer and G. Parkinson, *Science* **346**, 1215 (2014).

[108] R. Pentcheva, W. Moritz, J. Rundgren, S. Frank, D. Schrupp and M. Scheffler, *Surf. Sci.* **602**, 1299 (2008).

[109] M. Zajac, K. Freindl, T. Slezak, M. Slezak, N. Spiridis, D. Wilgocka-Slezak and J. Korecki, *Thin Solid Films* **519**, 5588 (2011).

[110] A. Subagyo, Y. Sasaki, H. Oka and K. Sueoka, *Phys. Stat. Sol.* **244**, 4482 (2007).

[111] N. C. Bartelt, S. Nie, E. Starodub, I. Bernal-Villamil, S. Gallego, L. Vergara, K. F. McCarty and J. de la Figuera, *Phys. Rev. B* **88**, 235436 (2013).

[112] G. S. Parkinson, T. A. Manz, Z. Novotný, P. T. Sprunger, R. L. Kurtz, M. Schmid, D. S. Sholl and U. Diebold, *Phys. Rev. B* **85**, 195450 (2012).

[113] J. de la Figuera, Z. Novotny, M. Setvin, T. Liu, Z. Mao, G. Chen, A. T. NDiaye, M. Schmid, U. Diebold, A. K. Schmid and G. S. Parkinson, *Phys. Rev. B* **88**, 161410(R) (2013).

[114] T. Kendelewicz, S. Kaya, J. T. Newberg, H. Bluhm, N. Mulakaluri, W. Moritz, M. Scheffler, A. Nilsson, R. Pentcheva and G. E. Brown, Jr., *J. Phys. Chem. C* **117**, 2719 (2013).

[115] S. de Jong, R. Kukreja, C. Trabant, N. Pontius, C. F. Chang, T. Kachel, H. A. Dürr et al., *Nature Materials* **12**, 882886 (2013).

[116] K. Jordan, A. Cazacu, G. Manai, S. F. Ceballos, S. Murphy and I. V. Shvets, *Phys. Rev. B* **74**, 085416 (2006).

[117] N. Spiridis, D. Wilgocka-Ślezak, K. Freindl, B. Figarska, T. Giela, E. Młyńczak, B. Strzelczyk, M. Zajac, and J. Korecki, *Phys. Rev. B* **85**, 075436 (2012).

[118] I. Palacio, M. Monti, J. F. Marco, K. F. McCarty, and J. de la Figuera, *J. Phys.: Condens. Matter* **25**, 484001 (2013).

[119] W. Meyer, D. Hock, K. Biedermann, M. Gubo, S. Müller, L. Hammer, and K. Heinz, *Phys. Rev. Lett.* **101**, 016103 (2008).